Synchrony and Oscillatory Dynamics for a 2-D PDE-ODE Model of Diffusion-Mediated Communication Between Small Signaling Compartments

Sarafa A. Iyaniwura and Michael J. Ward

October 16, 2020

Abstract

We analyze a class of cell-bulk coupled PDE-ODE models, motivated by quorum sensing and diffusion-mediated behavior in microbial systems, that characterize communication between localized spatially segregated dynamically active signaling compartments or "cells" that have a permeable boundary. In this model, the cells are disks of a common radius $\varepsilon \ll 1$ and they are spatially coupled through a passive extracellular bulk diffusion field with diffusivity D in a bounded 2-D domain. Each cell secretes a signaling chemical into the bulk region at a constant rate and receives a feedback of the bulk chemical from the entire collection of cells. This global feedback, which activates signaling pathways within the cells, modifies the intracellular dynamics according to the external environment. The cell secretion and global feedback are regulated by permeability parameters across the cell membrane. For arbitrary reaction-kinetics within each cell, the method of matched asymptotic expansions is used in the limit $\varepsilon \ll 1$ of small cell radius to construct steady-state solutions of the PDE-ODE model, and to derive a globally coupled nonlinear matrix eigenvalue problem (GCEP) that characterizes the linear stability properties of the steady-states. The analysis and computation of the nullspace of the GCEP as parameters are varied is central to the linear stability analysis. In the limit of large bulk diffusivity $D = D_0/\nu \gg 1$, where $\nu \equiv -1/\log\varepsilon$, an asymptotic analysis of the PDE-ODE model leads to a limiting ODE system for the spatial average of the concentration in the bulk region that is coupled to the intracellular dynamics within the cells. Results from the linear stability theory and ODE dynamics are illustrated for Sel'kov reaction-kinetics, where the kinetic parameters are chosen so that each cell is quiescent when uncoupled from the bulk medium. For various specific spatial configurations of cells, the linear stability theory is used to construct phase diagrams in parameter space characterizing where a switch-like emergence of intracellular oscillations can occur through a Hopf bifurcation. The effect of the membrane permeability parameters, the reaction-kinetic parameters, the bulk diffusivity, and the spatial configuration of cells on both the emergence and synchronization of the oscillatory intracellular dynamics, as mediated by the bulk diffusion field, is analyzed in detail. The linear stability theory is validated from full numerical simulations of the PDE-ODE system, and from the reduced ODE model when D is large.

Key Words: Green's function, bulk diffusion, globally coupled eigenvalue problem (GCEP), Hopf bifurcation, cell-bulk coupling, synchronous oscillations, diffusion-mediated communication.

1 Introduction

Cell-to-cell communication is an important aspect of microbial systems that is often achieved through the diffusion of an extracellular signaling molecule, referred to as an autoinducer, in their common environment (cf. [13], [46], [9], [56]). This form of bulk-mediated communication involves the secretion and feedback of signaling molecules from and into the cells, respectively, which enables each cell to adjust its intracellular dynamics based on the signals it receives from the autoinducer field that depends on the entire collection of cells. Specific autoinducers responsible for such an intercellular communication have been identified in many biological systems including, cyclic adenosine monophosphate (cAMP) that triggers intracellular oscillations for a collection of social amoebae *Dictyostelium discoideum* and guides them to aggregation in low nutrient environments (cf. [22], [37], [16]), acetaldehyde (Ace) that leads to glycolytic oscillations in a colony of yeast cells (cf. [8], [9], [10]), and acylated homoserine lactones (AHLs) that induces bioluminescence for certain species of squid due to colonies of the marine bacterium *Vibrio fischeri* located in the squid's light organ (cf. [46]).

In this context of intercellular bulk-mediated communication, quorum-sensing (QS) refers to the onset of collective dynamics in the cells that occurs when the cell density increases past a threshold. There are two main categories of QS systems, for which mathematical models have been developed. The first main type, which includes yeast cells and social amoeba, involves a switch-like onset of synchronized oscillatory intracellular dynamics as the cell density increases (cf. [8], [9], [10], [22], [33], [27]). On the macroscale, triggered synchronous temporal oscillations also occur in physicochemical systems involving small catalyst-loaded particles immersed in a Belousov-Zhabotinsky chemical mixture (cf. [48], [47], [50], [49]). The second main type of QS system, for which the marine bacterium *Vibrio fischeri* and the human pathogen *Pseudomonas aeruginosa* are prototypical examples, is where an increase in the cell density leads to a sudden transition between bistable steady-states (cf. [12], [53], [32]).

We will focus on analyzing a conceptual PDE-ODE model for a QS system that involves a switch-like onset of synchronous intracellular oscillations. QS systems of this type have most typically been studied for well-stirred systems, where the bulk diffusivity is taken to be infinite. This well-mixed limit leads to a globally coupled ODE system, where the global coupling arises from the spatially homogeneous bulk diffusion field (cf. [22], [10], [47], [50], [30], [39], [26]). In this more classical ODE setting, well-established mathematical tools such as ODE bifurcation theory, phase reduction methods and the Kuramoto order parameter (cf. [41], [36]) can be used to analyze the onset of QS behavior and predict the degree of synchronization of intracellular oscillations as the cell density increases.

However, when the bulk diffusivity is finite, diffusion-mediated behavior associated with the spatial configuration of cells, the spatial gradients of the bulk signal, reflecting versus absorbing boundary conditions, and the mass transport properties of the bulk medium, have all been shown experimentally to play an important role for some QS systems (cf. [15], [11], [51], [24] and the references therein). In contrast to the study of QS behavior through an ODE theoretical framework, there have been relatively few theoretical and modeling studies of how spatial diffusion triggers the onset of collective intracellular oscillations in spatially segregated, but localized, dynamically active reaction sites, and these studies have typically been considered in 1-D spatial contexts (cf. [17], [7], [19], [21], [18], [31], [38], [58], [40].)

The goal of this paper is to study the emergence and synchronization of intracellular oscillations for the coupled cell-bulk PDE-ODE model of [20] in a 2-D domain. The formulation of this model was inspired by the 3-D PDE-ODE cell-based model of [34] with a single intracellular species (see also [35] and [52]). In contrast to the analysis in [20] that was restricted either to the well-mixed limit or to the simple case of a ring pattern of identical cells, our study will focus on analyzing diffusion-mediated behavior, resulting from a passive bulk diffusion field with finite diffusivity, for various spatial configurations of a collection of heterogeneous cells.

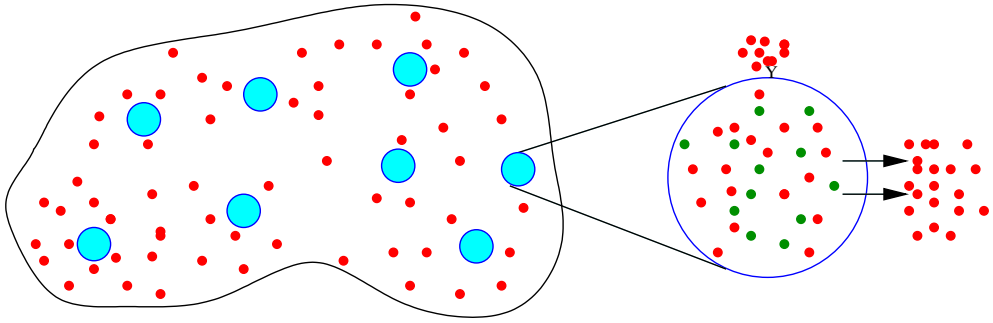

Figure 1: A schematic diagram showing dynamically active signaling compartments (in cyan) in an arbitrary bounded 2D domain. The green and red dots represent the signaling chemicals in the cells, where only the red is secreted into the extracellular bulk region. On the right: A zoomed-in illustration of the intracellular concentration of chemicals within each signaling compartment, the secretion of signaling molecules into the bulk region, and the feedback of chemical into the cells.

The coupled PDE-ODE model of [20] is formulated as follows: Within Ω we assume that there are m dynamically active circular signalling compartments or "cells" of a common radius R_0, denoted by Ω_j and centered at $\boldsymbol{X}_j \in \Omega$ for $j = 1, \ldots, m$. In the bulk, or extracellular, region $\Omega \setminus \cup_{j=1}^m \Omega_j$, the concentration $\mathcal{U}(\boldsymbol{X}, T)$ of the autoinducer or bulk signal, which is confined within $\partial\Omega$, is assumed to satisfy the passive diffusion equation

$$\mathcal{U}_T = D_B \, \Delta \mathcal{U} - k_B \, \mathcal{U} \,, \quad T > 0 \,, \quad \boldsymbol{X} \in \Omega \setminus \cup_{j=1}^m \Omega_j \,; \tag{1.1a}$$

$$\partial_{n_{\boldsymbol{X}}} \mathcal{U} = 0, \quad \boldsymbol{X} \in \partial\Omega \,; \qquad D_B \, \partial_{n_{\boldsymbol{X}}} \mathcal{U} = \beta_{1j} \, \mathcal{U} - \beta_{2j} \, \mu_j^1 \,, \quad \boldsymbol{X} \in \partial\Omega_j \,, \qquad j = 1, \ldots, m \,. \tag{1.1b}$$

Here $D_B > 0$ and $k_B > 0$ are the dimensional bulk diffusivity and rate of degradation of the bulk signal, respectively. In the Robin boundary condition (1.1b) on the cell membrane, $\beta_{1j} > 0$ and $\beta_{2j} > 0$ are dimensional parameters modeling the influx and efflux of chemical into and out of the j^{th} cell, while $\partial_{n_{\boldsymbol{X}}}$ denotes the outer normal derivative on the cell boundary that points into the bulk region. Within each cell we assume that there are n interacting species represented by the vector $\boldsymbol{\mu}_j = (\mu_j^1, \ldots, \mu_j^n)^T$. Assuming that the cells are sufficiently small so that there are no spatial chemical gradients within them, the intracellular reaction-kinetics $\boldsymbol{F}_j$ for the j^{th} cell is coupled to the bulk medium via the integration of the flux across the cell membrane. In this way, the intracellular dynamics within the j^{th} cell is coupled to the bulk signal (1.1) by

$$\frac{d\boldsymbol{\mu}_j}{dT} = k_R \, \mu_c \, \boldsymbol{F}_j \left(\boldsymbol{\mu}_j / \mu_c \right) + \boldsymbol{e}_1 \int_{\partial\Omega_j} \left(\beta_{1j} \, \mathcal{U} - \beta_{2j} \, \mu_j^1 \right) \, dS_{\boldsymbol{X}} \,, \qquad j = 1, \ldots, m \,. \tag{1.1c}$$

Here $\boldsymbol{e}_1 = (1, 0, \ldots, 0)^T$, $k_R > 0$ is the dimensional reaction rate for the intracellular kinetics, and $\mu_c > 0$ is a typical value for $\boldsymbol{\mu}_j$. In this model, one signaling chemical, labeled by μ_j^1 can permeate the cell membrane with an efflux parameter β_{2j} and, by diffusion through the bulk medium, can communicate with spatially distant cells. The influx permeability parameter β_{1j} controls the global feedback into the j^{th} cell from the bulk diffusion field, which is determined by the entire collection of cells. In Fig. 1 we schematically illustrate the cell-bulk coupling for the case of $n = 2$ intracellular species.

We assume that the radius R_0 of the signaling compartments is small relative to the domain length-scale L, and so we introduce a small parameter $\varepsilon \equiv R_0/L \ll 1$. Then, by non-dimensionalizing the coupled PDE-ODE model (1.1) using the approach of [20], we obtain that the dimensionless concentration of chemical $U(\boldsymbol{x},t)$ in the bulk region satisfies

$$\tau \frac{\partial U}{\partial t} = D\,\Delta U - U\,, \quad t>0\,, \quad \boldsymbol{x}\in\Omega\setminus \cup_{j=1}^m \Omega_{\varepsilon_j}\,; \tag{1.2a}$$

$$\partial_n U = 0\,, \quad \boldsymbol{x}\in\partial\Omega\,; \qquad \varepsilon D\,\partial_n U = d_{1j}\,U - d_{2j}\,u_j^1\,, \quad \boldsymbol{x}\in\partial\Omega_{\varepsilon_j}\,, \qquad j=1,\ldots,m\,, \tag{1.2b}$$

which is coupled to the dimensionless dynamics within the j^{th} cell by

$$\frac{\mathrm{d}\boldsymbol{u}_j}{\mathrm{d}t} = \boldsymbol{F}_j(\boldsymbol{u}_j) + \frac{\boldsymbol{e}_1}{\varepsilon\tau}\int_{\partial\Omega_{\varepsilon_j}} (d_{1j}\,U - d_{2j}\,u_j^1)\,\mathrm{d}s\,, \qquad j=1,\ldots,m\,, \tag{1.2c}$$

where $\boldsymbol{u}_j = (u_j^1,\ldots,u_j^n)^T$ is the dimensionless vector representing the n chemical species in the j^{th} cell, labeled by $\Omega_{\varepsilon_j} \equiv \{\boldsymbol{x}\,|\,|\boldsymbol{x}-\boldsymbol{x}_j|\le\varepsilon\}$. We assume that the centers of the cells are well-separated in the sense that $\text{dist}(\boldsymbol{x}_j,\boldsymbol{x}_k)=\mathcal{O}(1)$ for $j\neq k$ and $\text{dist}(\boldsymbol{x}_j,\partial\Omega)=\mathcal{O}(1)$ as $\varepsilon\to 0$. In this dimensionless formulation (1.2), the key dimensionless parameters are

$$D \equiv \frac{D_B}{k_B L^2}\,, \qquad d_{1j}\equiv \varepsilon\frac{\beta_{1j}}{k_B L} = \mathcal{O}(1)\,, \qquad d_{2j}\equiv \varepsilon\frac{\beta_{2j}L}{k_B} = \mathcal{O}(1)\,, \qquad \tau \equiv \frac{k_R}{k_B}\,. \tag{1.3}$$

We refer to D and τ as the effective bulk diffusivity and reaction-time parameter, respectively. In (1.3), the permeability parameters β_{1j} and β_{2j} are chosen as $\mathcal{O}(\varepsilon^{-1})$ in order to ensure that there is an $\mathcal{O}(1)$ transport across the membrane of the small cells. The parameter τ measures the relative rate of the intracellular dynamics to the time-scale for degradation of the bulk chemical. When the intracellular reactions proceed slowly, τ is small, and little communication between the cells occurs. When the effective bulk diffusivity D is large, the cells are readily able to communicate through the bulk medium, and in the well-mixed limit $D\to\infty$ the bulk signal becomes spatially homogeneous. Alternatively, for smaller values of D, only those cells that are in close spatial proximity should be able to communicate through the bulk diffusion field.

For arbitrary intracellular reaction kinetics and for an arbitrary spatial arrangement of cells, in §2 we use strong localized perturbation theory (cf. [54], [55]) in the limit $\varepsilon\to 0$ to construct steady-state solutions of (1.2) and to derive the linear stability problem for these steady-states. Unstable eigenvalues of the linearization of a steady-state are shown to correspond to roots λ in $\text{Re}(\lambda)>0$ for which a certain globally coupled nonlinear matrix eigenvalue problem (GCEP) $\mathcal{M}(\lambda)\boldsymbol{c}=0$ (see (2.20)) has a nontrivial solution. The $m\times m$ matrix $\mathcal{M}$, which couples all the cells through an eigenvalue-dependent Green's matrix, depends on the dimensionless parameters in (1.3). The components of the corresponding normalized eigenvector $\boldsymbol{c}$ determines the relative magnitude of the spatial gradient of the bulk signal near the cell membranes and it determines the relative phases and amplitudes of small-scale oscillations within the cells at the onset of a Hopf bifurcation when $\lambda = i\lambda_I$, with $\lambda_I>0$, is a root of $\det\mathcal{M}(\lambda)=0$ (see (2.24)).

In §3, strong localized perturbation theory is used to reduce the PDE-ODE model (1.2) to an ODE differential algebraic system with global coupling for the distinguished limit $D=D_0/\nu \gg 1$ of large bulk diffusivity, where $\nu\equiv -1/\log\varepsilon$. In contrast to the simpler ODE system derived in [20] for the well-mixed limit $D\to\infty$ (i.e. $D\gg\mathcal{O}(\nu^{-1})$), the new derivation in §3, as summarized in Proposition 2, leads to an ODE system that depends on the scaled bulk diffusivity parameter D_0 and it depends weakly on the specific spatial configuration of cells within the domain.

Our asymptotic theory is applied for the case of Sel'kov reaction kinetics, which has been used as a conceptual model for glycolysis oscillations in yeast cells [45]. With Sel'kov kinetics, (1.2) has a unique steady-state when $\varepsilon\ll 1$. As indicated from the experimental and modeling studies of collective behavior in yeast cells (cf. [9], [8], [10]), individual yeast cells are typically non-oscillatory when isolated, but readily become synchronized in a population of such cells. In qualitative agreement with this observation, the Sel'kov parameters are chosen to be close to the threshold for the onset of limit-cycle oscillations for an isolated cell. As a result, the switch-like emergence of intracellular oscillations, resulting from a Hopf bifurcation and illustrated through various phase diagrams, is inherently due to the cell-cell interaction, as mediated by the bulk diffusion field. In our study we will analyze how the onset of intracellular oscillations and synchronization depends on the membrane permeability parameters, the reaction-time parameter, the bulk diffusivity, a Sel'kov kinetic parameter, and the spatial pattern of cells. Diffusion-mediated behavior, whereby cells initiate oscillations as a result of certain spatial effects such as cell-clustering or the buildup of large spatial gradients of the autoinducer field near the cell boundary, are illustrated.

In §4 we illustrate our theory with Sel'kov reaction kinetics for a ring and center-cell pattern of cells in the unit disk (see Fig. 3), where the ring cells are taken to have common parameters but where the parameters for the center cell can be different. For the unit disk, the Green's matrices needed in the steady-state and linear stability theory are available analytically. For a ring and center-cell pattern, the GCEP matrix $\mathcal{M}(\lambda)$ has a cyclic sub-block and so in §4.1 we can analytically identify particular spatial modes for which $\det\mathcal{M}(\lambda)=0$. By using arclength continuation in D, Hopf bifurcation boundaries in the (D,τ) parameter space for which $\det\mathcal{M}(i\lambda_I)=0$ can be computed for each of these modes. In open regions of the (D,τ) parameter plane, we show how to use a winding number criterion numerically on the roots of $\det\mathcal{M}(\lambda)=0$ in $\text{Re}(\lambda)>0$, so as to compute the number of unstable eigenvalues of the linearization of the unique steady-state. In §4.2 these phase

diagrams are shown for the case of two ring cells. The triggering effect on the emergence of intracellular oscillations due to a center cell with either different permeability parameters or a different Sel'kov kinetic parameter is studied in §4.3 and §4.4, respectively. Diffusion-mediated behavior as a result of changes in the ring radius are studied in §4.5. The linear stability theory, which predicts the onset of intracellular oscillations together with the amplitude and phase differences near the Hopf bifurcation point, is validated through large-scale simulations of the PDE-ODE model (1.2) using FlexPDE [14]. Moreover, we show that in certain cases the new ODE system in Proposition 2, derived for $D = D_0/\nu \gg 1$, can still provide a decent agreement with the full numerical results even when $D = \mathcal{O}(1)$.

In §5 we study how the onset of intracellular oscillations depends on the specific spatial arrangement of ten cells in the unit disk that differ only in their influx permeabilites d_{1j}, for $j = 1, \ldots, m$. The cell configurations considered include two clusters of cells (see Fig. 17b), two rings of cells with two isolated cells (see Fig. 23b), and arbitrarily placed cells (see Fig. 17d). For computational simplicity, we primarily focus on the regime $D = D_0/\nu \gg 1$, where matrix perturbation theory can be used to asymptotically calculate the spectrum of the GCEP matrix $\mathcal{M}(\lambda)$, as summarized in Proposition 4. Since this analysis shows that only one matrix eigenvalue of $\mathcal{M}(\lambda)$ can cross through zero, in §5.1 a numerical root-finding is readily implemented on this eigenvalue to determine Hopf bifurcation boundaries in the (D_0, τ) plane where intracellular oscillations originate for the various spatial configurations of cells and permeability parameter sets d_{1j} for $j = 1, \ldots, 10$. Our linear stability results, validated through FlexPDE simulations of (1.2) and the ODE dynamics of Proposition 2, shows that when $D = D_0/\nu$ the intracellular dynamics depend sensitively on the influx permeability set, but only weakly on the cell locations. In §5.1.1 we implement the linear stability theory based on the GCEP matrix for $D = \mathcal{O}(1)$ to predict that small-scale intracellular oscillations can be highly heterogeneous in terms of amplitude and phase when there are isolated cells. The linear stability theory is confirmed from full PDE simulations. Finally, in §6 we briefly summarize our study and discuss some biological modeling problems that are well-aligned with the cell-based PDE-ODE framework of (1.1).

2 Asymptotic analysis of the dimensionless coupled model

In this section, strong localized perturbation theory in the limit $\varepsilon \to 0$ is applied to the dimensionless PDE-ODE model (1.2) for the regime $D = \mathcal{O}(1)$. This theory is used to asymptotically approximate the steady-state solution of the coupled model, and also to formulate a globally coupled eigenvalue problem (GCEP) for studying the linear stability properties of the derived steady-state solution.

2.1 Asymptotic construction of the steady-state solution

We construct the steady-state solution for (1.2) using matched asymptotics. In the j^{th} inner region, defined within an $\mathcal{O}(\varepsilon)$ neighborhood of the boundary of the j^{th} cell, we introduce the local variables $\boldsymbol{y} = \varepsilon^{-1}(\boldsymbol{x} - \boldsymbol{x}_j)$ and $U_j(\boldsymbol{x}) = U_j(\varepsilon \boldsymbol{y} + \boldsymbol{x}_j)$, where $\rho \equiv |\boldsymbol{y}|$. Upon writing (1.2) in terms of the inner variables, for $\varepsilon \to 0$ the steady-state problem in the j^{th} inner region is $\Delta U_j = 0$ for $\rho \geq 1$, subject to $D\, \partial_\rho U_j = d_{1j} U_j - d_{2j} u_j^1$ on $\rho = 1$. The radially symmetric solution to this problem is

$$U_j(\rho) = A_j \log \rho + \frac{1}{d_{1j}} \left(D\, A_j + d_{2j} u_j^1 \right) , \qquad j = 1, \ldots, m \,, \tag{2.1}$$

where A_j for $j = 1, \ldots, m$ are constants to be determined. Upon substituting (2.1) into the steady-state problem of (1.2c), we obtain that the steady-state intracellular dynamics $\boldsymbol{u}_j$ of the j^{th} cell satisfies

$$\boldsymbol{F}_j \left(\boldsymbol{u}_j \right) + \frac{2\pi D}{\tau} A_j \boldsymbol{e}_1 \, = \boldsymbol{0} \,, \qquad j = 1, \ldots, m \,. \tag{2.2}$$

This determines $\boldsymbol{u}_j$ in terms of the unknown constant A_j. To proceed, we must derive another algebraic system for the constants A_j for $j = 1, \ldots, m$, which is then coupled to (2.2).

By matching the far-field behaviour of the inner solution (2.1) to an outer steady-state solution for (1.2a), we obtain that the outer solution must satisfy a specific singularity behaviour as $\boldsymbol{x} \to \boldsymbol{x}_j$. In this way, the steady-state outer approximation for the bulk solution satisfies

$$\begin{aligned} &\Delta U - \varphi^2 U = 0 \,, \quad \boldsymbol{x} \in \Omega \setminus \{ \boldsymbol{x}_1, \ldots, \boldsymbol{x}_m \} \,; \qquad \partial_n U = 0 \,, \quad \boldsymbol{x} \in \partial\Omega \,; \\ &U \sim A_j \log |\boldsymbol{x} - \boldsymbol{x}_j| + \frac{A_j}{\nu} + \frac{1}{d_{1j}} (D A_j + d_{2j} u_j^1) \,, \quad \text{as} \quad \boldsymbol{x} \to \boldsymbol{x}_j \,, \qquad j = 1, \ldots, m \,, \end{aligned} \tag{2.3}$$

where $\nu \equiv -1/\log \varepsilon$, with $\varepsilon \ll 1$, and $\varphi \equiv \sqrt{1/D}$. The pre-specification of the regular part of each singularity structure in (2.3) yields a constraint. Overall these constraints provide an algebraic system for A_j for $j = 1, \ldots, m$.

To determine this algebraic system, we next represent the solution to (2.3) as

$$U = -2\pi \sum_{i=1}^{m} A_i G(\boldsymbol{x}; \boldsymbol{x}_i) \,, \tag{2.4}$$

where the reduced-wave Green's function $G(\boldsymbol{x};\boldsymbol{x}_j)$ satisfies

$$\begin{aligned} &\Delta G - \varphi^2 G = -\delta(\boldsymbol{x}-\boldsymbol{x}_j)\,, \quad \boldsymbol{x}\in\Omega\,; \qquad \partial_n G = 0\,, \quad \boldsymbol{x}\in\partial\Omega\,; \\ &G(\boldsymbol{x};\boldsymbol{x}_j) \sim -\frac{1}{2\pi}\log|\boldsymbol{x}-\boldsymbol{x}_j| + R(\boldsymbol{x}_j) + o(1)\,, \quad \text{as} \quad \boldsymbol{x}\to\boldsymbol{x}_j\,. \end{aligned} \tag{2.5}$$

Here $R_j \equiv R(\boldsymbol{x}_j)$ is the regular part of $G(\boldsymbol{x};\boldsymbol{x}_j)$ at $\boldsymbol{x}=\boldsymbol{x}_j$. By expanding (2.4) as $\boldsymbol{x}\to\boldsymbol{x}_j$, we simply require that the non-singular terms of the resulting expression agree with that specified in (2.3) for each $j=1,\dots,m$. This leads to an algebraic system for the vector $\boldsymbol{\mathcal{A}} \equiv (A_1,\dots,A_m)^T$, which is given in matrix form as

$$\Big(I + 2\pi\nu\mathcal{G} + \nu D P_1\Big)\boldsymbol{\mathcal{A}} = -\nu\, P_2\, \boldsymbol{u}^1\,, \tag{2.6}$$

where $\boldsymbol{u}^1 \equiv (u_1^1, u_2^1, \dots, u_m^1)^T$ denotes the vector of chemicals that is secreted into the bulk region by the cells. In (2.6), $\mathcal{G}$ is the symmetric reduced-wave Green's interaction matrix, while P_1 and P_2 are $m\times m$ diagonal matrices, defined by

$$\mathcal{G} \equiv \begin{pmatrix} R_1 & G_{12} & \dots & G_{1m} \\ G_{21} & R_2 & \dots & G_{2m} \\ \vdots & \vdots & \ddots & \vdots \\ G_{m1} & G_{m2} & \dots & R_m \end{pmatrix}\,, \quad P_1 \equiv \operatorname{diag}\Big(\frac{1}{d_{11}},\dots,\frac{1}{d_{1m}}\Big)\,, \quad P_2 \equiv \operatorname{diag}\Big(\frac{d_{21}}{d_{11}},\dots,\frac{d_{2m}}{d_{1m}}\Big)\,. \tag{2.7}$$

Here $G_{ji} = G_{ij} \equiv G(\boldsymbol{x}_j;\boldsymbol{x}_i)$ for $i\neq j$, and $R_j \equiv R(\boldsymbol{x}_j)$ for $j=1,\dots,m$, are obtained from the solution to (2.5).

Overall, the asymptotic steady-state solution is determined in terms of the solution $\boldsymbol{\mathcal{A}}$ and $\boldsymbol{u}_j$ for $j=1,\dots,m$, to the $n\times m$ dimensional nonlinear algebraic system (NAS) given by (2.2) and (2.6). This system applies to arbitrary local reaction kinetics $\boldsymbol{F}_j$ and permeabilities parameters $d_{1j}>0$ and $d_{2j}>0$ for $j=1,\dots,m$. When the kinetics and permeability parameters are identical for all the cells, the NAS reduces to the system given in equations (2.4) and (2.9) of [20].

Depending on the specific reaction kinetics assumed, the solution structure to (2.2) and (2.6) as parameters are varied can involve solution multiplicity, saddle-node points, and other bifurcations. However, to illustrate our asymptotic theory we will focus on the two-component Sel'kov reaction kinetics for which (2.2) and (2.6) has a unique solution.

2.2 Linear stability analysis

In the previous subsection, we characterized steady-state solutions of the coupled model (1.2) using strong perturbation theory. Suppose that the NAS (2.2) and (2.6) has a solution for a given set of parameters. This then yields an approximation to the steady-state solution solution $U_e(\boldsymbol{x})$ and $\boldsymbol{u}_{ej}$, for $j=1,\dots,m$, to (1.2). To determine the linear stability of this steady-state we begin by introducing the perturbation

$$U(\boldsymbol{x},t) = U_e(\boldsymbol{x}) + e^{\lambda t}\xi(\boldsymbol{x}) \qquad \text{and} \qquad \boldsymbol{u}_j(t) = \boldsymbol{u}_{ej} + e^{\lambda t}\boldsymbol{\phi}_j\,, \quad j=1,\dots,m\,. \tag{2.8}$$

where λ is the eigenvalue of the linearization, and $\xi(\boldsymbol{x})$ and $\boldsymbol{\phi}_j \equiv (\phi_j^1,\dots,\phi_j^n)^T$ are the corresponding eigenfunctions in the bulk region and in the j^{th} cell, respectively. Upon substituting this perturbation into the PDE-ODE model (1.2), in the bulk region we obtain the linearized problem

$$\tau\lambda\xi = D\,\Delta\xi - \xi\,, \quad \boldsymbol{x}\in\Omega\setminus\cup_{j=1}^m\Omega_{\varepsilon_j}\,; \tag{2.9a}$$

$$\partial_n\xi = 0, \quad \boldsymbol{x}\in\partial\Omega\,; \qquad \varepsilon D\,\partial_{nj}\xi = d_{1j}\,\xi - d_{2j}\,\phi_j^1\,, \quad \boldsymbol{x}\in\partial\Omega_{\varepsilon_j}\,, \qquad j=1,\dots,m\,, \tag{2.9b}$$

which is coupled to the linearized intracellular dynamics of the j^{th} cell given in terms of $\boldsymbol{\phi}_j \equiv (\phi_j^1,\dots,\phi_j^n)^T$, by

$$\lambda\boldsymbol{\phi}_j = J_j\,\boldsymbol{\phi}_j + \frac{\boldsymbol{e}_1}{\varepsilon\tau}\int_{\partial\Omega_{\varepsilon_j}}(d_{1j}\,\xi - d_{2j}\,\phi_j^1)\,\mathrm{d}s\,, \qquad j=1,\dots,m\,. \tag{2.9c}$$

Here $J_j \equiv J(\boldsymbol{u}_{ej})$ is the Jacobian matrix of the local kinetics $\boldsymbol{F}_j$ evaluated at the steady-state $\boldsymbol{u}_{ej}$.

Next, we use strong localized perturbation theory to analyze the eigenvalue problem (2.9) in the limit $\varepsilon\to 0$. This analysis leads to a limiting globally coupled eigenvalue problem (GCEP) for λ in the form of a nonlinear matrix eigenvalue problem. This GCEP will be used to investigate instabilities of the steady-state solution for the PDE-ODE system (1.2).

To derive this GCEP, we first construct an inner region in an $\mathcal{O}(\varepsilon)$ neighborhood of the j^{th} cell by introducing the local variables $\boldsymbol{y} = \varepsilon^{-1}(\boldsymbol{x}-\boldsymbol{x}_j)$ and $\xi_j(\boldsymbol{x}) \equiv \xi_j(\boldsymbol{x}_j+\varepsilon\boldsymbol{y})$ with $\rho=|\boldsymbol{y}|$. From (2.9), we obtain for $\varepsilon\to 0$ that

$$\Delta\,\xi_j = 0, \quad 1<\rho<\infty; \qquad D\,\partial_\rho\,\xi_j = d_{1j}\xi_j - d_{2j}\phi_j^1, \quad \text{on} \quad \rho=1, \tag{2.10}$$

in the j^{th} inner region. The radially symmetric solution to (2.10) is

$$\xi_j = c_j \log\rho + \frac{1}{d_{1j}}\left(D\, c_j + d_{2j}\phi_j^1\right)\,, \qquad j = 1,\ldots,m\,, \tag{2.11}$$

where $\rho = |\boldsymbol{y}|$ and c_j for $j = 1,\ldots,m$ are constants to be determined. Upon substituting (2.11) into the linearized intracellular dynamics of the j^{th} cell (2.9c), we obtain a linear relation between $\boldsymbol{\phi}_j$ and c_j given by

$$(J_j - \lambda I)\boldsymbol{\phi}_j = -\frac{2\pi D}{\tau}\, c_j \boldsymbol{e}_1\,. \qquad j = 1,\ldots,m\,. \tag{2.12}$$

Next, by analyzing the outer solution in the bulk region, we will derive another linear system, which will be coupled to (2.12). These two systems will provide the GCEP that is needed to study the linear stability of the steady-state solution.

To determine this additional linear system, we first match the far-field behaviour of the inner solution (2.11) to the outer solution in order to obtain the singularity behaviour of the outer solution as $\boldsymbol{x} \to \boldsymbol{x}_j$. This yields in the bulk region that

$$\begin{aligned} &\Delta\xi - \varphi_\lambda^2\,\xi = 0\,, \quad \boldsymbol{x}\in\Omega\setminus\{\boldsymbol{x}_1,\ldots,\boldsymbol{x}_m\}\,; \qquad \partial_n\xi = 0\,, \quad \boldsymbol{x}\in\partial\Omega\,; \\ &\xi \sim c_j\log|\boldsymbol{x}-\boldsymbol{x}_j| + \frac{c_j}{\nu} + \frac{1}{d_{1j}}(Dc_j + d_{2j}\phi_j^1)\,, \quad \text{as} \quad \boldsymbol{x}\to\boldsymbol{x}_j\,, \qquad j = 1,\ldots,m\,, \end{aligned} \tag{2.13}$$

where $\nu \equiv -1/\log\varepsilon$ and $\varphi_\lambda = \sqrt{(1+\tau\lambda)/D}$. The solution to (2.13) is represented as

$$\xi(\boldsymbol{x}) = -2\pi\sum_{i=1}^m c_i\, G_\lambda(\boldsymbol{x};\boldsymbol{x}_i)\,, \tag{2.14}$$

where the eigenvalue-dependent reduced-wave Green's function $G_\lambda(\boldsymbol{x};\boldsymbol{x}_j)$ satisfies

$$\Delta G_\lambda - \varphi_\lambda^2 G_\lambda = -\delta(\boldsymbol{x}-\boldsymbol{x}_j)\,, \quad \boldsymbol{x}\in\Omega\,; \qquad \partial_n G_\lambda = 0\,, \quad \boldsymbol{x}\in\partial\Omega\,; \tag{2.15a}$$

$$G_\lambda(\boldsymbol{x};\boldsymbol{x}_j) \sim -\frac{1}{2\pi}\log|\boldsymbol{x}-\boldsymbol{x}_j| + R_\lambda(\boldsymbol{x}_j) + o(1)\,, \quad \text{as} \quad \boldsymbol{x}\to\boldsymbol{x}_j\,. \tag{2.15b}$$

Here $R_{\lambda j} \equiv R_\lambda(\boldsymbol{x}_j)$ is the regular part of $G_\lambda(\boldsymbol{x};\boldsymbol{x}_j)$ at $\boldsymbol{x} = \boldsymbol{x}_j$. In (2.14) we have specified the principal branch of φ_λ to ensure that G_λ is analytic in $\mathrm{Re}(\lambda) > 0$ and that G_λ decays far away from the cells.

By expanding (2.14) as $\boldsymbol{x}\to\boldsymbol{x}_j$, we equate the non-singular terms of the resulting expression with those specified in (2.13) for each $j = 1,\ldots,m$. This yields a linear system for $\boldsymbol{c} \equiv (c_1,\ldots,c_m)^T$ given in matrix form by

$$\left(I + 2\pi\nu\mathcal{G}_\lambda + \nu\, D P_1\right)\boldsymbol{c} = -\nu\, P_2\,\boldsymbol{\phi}^1\,, \tag{2.16}$$

where $\boldsymbol{\phi}^1 \equiv (\phi_1^1,\ldots,\phi_m^1)^T$ and $\mathcal{G}_\lambda$ is the eigenvalue-dependent reduced-wave Green's matrix whose entries are defined by

$$(\mathcal{G}_\lambda)_{ij} = (\mathcal{G}_\lambda)_{ji} \equiv G_\lambda(\boldsymbol{x}_j,\boldsymbol{x}_i) \quad \text{for} \quad i\neq j\,, \quad \text{and} \quad (\mathcal{G}_\lambda)_{jj} = R_{\lambda j} \equiv R_\lambda(\boldsymbol{x}_j)\,. \tag{2.17}$$

In (2.16), the diagonal matrices P_1 and P_2 are defined in (2.7).

Next, we will combine the algebraic system (2.16) with (2.12) in order to derive the GCEP for λ and $\boldsymbol{c} = (c_1,\ldots,c_m)^T$. We first use (2.12) to determine ϕ_j^1 in terms of the constant c_j as $\phi_j^1 = 2\pi D\tau^{-1}\boldsymbol{e}_1^T(\lambda I - J_j)^{-1}\boldsymbol{e}_1\, c_j$ for $j = 1,\ldots,m$, provided that λ is not an eigenvalue of J_j for any $j = 1,\ldots,m$. In matrix form this yields

$$\boldsymbol{\phi}^1 = \frac{2\pi D}{\tau}\mathcal{K}\boldsymbol{c}\,, \tag{2.18}$$

where $\mathcal{K} \equiv \mathcal{K}(\lambda)$ is an $m\times m$ diagonal matrix $\mathcal{K} \equiv \mathrm{diag}\,(K_1,\ldots,K_m)$, whose entries are given by

$$K_j = \boldsymbol{e}_1^T(\lambda I - J_j)^{-1}\boldsymbol{e}_1 = \frac{\boldsymbol{e}_1^T N_j \boldsymbol{e}_1}{\det(\lambda I - J_j)} = \frac{(N_j)_{11}}{\det(\lambda I - J_j)}\,. \tag{2.19a}$$

Here N_j is the $n\times n$ matrix of cofactors of $(\lambda I - J_j)$, while $(N_j)_{11}$ is its entry in the first row and first column given by

$$(N_j)_{11} \equiv (N_j(\lambda))_{11} = \det\begin{pmatrix} \lambda - \left.\frac{\partial F_j^2}{\partial u_2}\right|_{\boldsymbol{u}=\boldsymbol{u}_{e,j}} & \cdots & -\left.\frac{\partial F_j^2}{\partial u_n}\right|_{\boldsymbol{u}=\boldsymbol{u}_{e,j}} \\ \vdots & \ddots & \vdots \\ -\left.\frac{\partial F_j^n}{\partial u_2}\right|_{\boldsymbol{u}=\boldsymbol{u}_{e,j}} & \cdots & \lambda - \left.\frac{\partial F_j^n}{\partial u_n}\right|_{\boldsymbol{u}=\boldsymbol{u}_{e,j}} \end{pmatrix}\,. \tag{2.19b}$$

The functions $F_j^2, \ldots, F_j^n$ are the components of the local reaction kinetics $\boldsymbol{F_j} \equiv (F_j^1, \ldots, F_j^n)^T$ of the j^{th} cell.

Upon substituting (2.18) into (2.16), we obtain the m-dimensional homogeneous algebraic system

$$\mathcal{M}(\lambda)\boldsymbol{c} = \boldsymbol{0}\,, \qquad \text{where} \qquad \mathcal{M}(\lambda) \equiv I + 2\pi\nu\mathcal{G}_\lambda + \nu\, D\, P_1 + \frac{2\pi\nu D}{\tau} P_2\mathcal{K}\,, \tag{2.20a}$$

where $\nu \equiv -1/\log\varepsilon$. The homogeneous system (2.20a), where $\mathcal{M}$ is a symmetric but non-Hermitian matrix, is referred to as the globally coupled eigenvalue problem (GCEP). The GCEP is a nonlinear matrix eigenvalue problem for λ, and it has a nontrivial solution $\boldsymbol{c} \neq \boldsymbol{0}$ if and only λ satisfies $\det\mathcal{M}(\lambda) = 0$. We label the set $\Lambda(\mathcal{M})$ as the union of all such roots, i.e.

$$\Lambda(\mathcal{M}) \equiv \{\lambda \,|\, \det\mathcal{M}(\lambda) = 0\}\,. \tag{2.20b}$$

The parameters in the GCEP (2.20a) are the bulk diffusivity D, the reaction-timescale τ and the permeabilities d_{1j} and d_{2j}, for $j = 1, \ldots, m$, which are encoded in the matrices P_1 and P_2 given in (2.7). Moreover, in (2.20a), the effect of the spatial configuration of the centers $\{\boldsymbol{x}_1, \ldots, \boldsymbol{x}_m\} \in \Omega$ of the cells and the domain shape Ω arises from both the eigenvalue-dependent reduced wave Green's interaction matrix $\mathcal{G}_\lambda$ and the steady-state solution, which determines $\mathcal{K}$ in (2.19).

A recent survey of nonlinear matrix eigenvalue problems and available solution strategies for certain classes of matrices is given in [23] and [4]. A range of applications of such problems, but in simpler contexts where $\mathcal{M}(\lambda)$ is either a polynomial or rational function of λ, are discussed in [3].

Any element $\lambda \in \Lambda(\mathcal{M})$ satisfying $\text{Re}(\lambda) > 0$ provides an approximation, valid as $\varepsilon \to 0$, for an unstable discrete eigenvalue of the linearized system (2.9). This leads to the following criterion regarding the linear stability of the steady-state solution.

Proposition 1. *For $\varepsilon \to 0$, a steady-state solution to (1.2) is linearly stable when there are no roots to $\det\mathcal{M}(\lambda) = 0$ in $Re(\lambda) > 0$, i.e. for all $\lambda \in \Lambda(\mathcal{M})$ we have $Re(\lambda) < 0$. Moreover, if $\mathcal{A}_e$ and $\boldsymbol{u}_{ej}$ for $j = 1, \ldots, m$ is a non-degenerate solution to the NAS (2.2) and (2.6), for which J_j is non-singular, then $\lambda = 0$ is not a root of $\det\mathcal{M}(\lambda) = 0$.*

Proof. For $\varepsilon \to 0$, any discrete eigenvalue λ of the linearization (2.8) corresponds to a non-trivial solution to (2.9). Since, for $\varepsilon \to 0$, these discrete eigenvalues comprise the set $\Lambda(\mathcal{M})$ in (2.20b), the steady-state is linearly stable if all $\lambda \in \Lambda(\mathcal{M})$ satisfy $\text{Re}(\lambda) < 0$. Next, suppose that $\mathcal{A}_e$ and $\boldsymbol{u}_{ej}$ for $j = 1, \ldots, m$ is a non-degenerate solution to the NAS (2.2) and (2.6). Introducing the perturbation $\mathcal{A} = \mathcal{A}_e + \boldsymbol{\psi}$ and $\boldsymbol{u}_j = \boldsymbol{u}_{ej} + \boldsymbol{v}_j$, where $|\boldsymbol{v}_j| \ll 1$ and $|\boldsymbol{\psi}| \ll 1$, we linearize (2.2) and (2.6) to obtain

$$\left(I + 2\pi\nu\mathcal{G} + \nu\, DP_1\right)\boldsymbol{\psi} = -\nu\, P_2\,\boldsymbol{v}^1\,, \qquad J_j\boldsymbol{v}_j = -\frac{2\pi D}{\tau}\,\psi_j\boldsymbol{e}_1\,. \qquad j = 1, \ldots, m\,, \tag{2.21}$$

where $\boldsymbol{v}^1 \equiv (v_1^1, \ldots, v_m^1)^T$, $\boldsymbol{\psi} = (\psi_1, \ldots, \psi_m)^T$ and $\boldsymbol{v}_j = (v_j^1, \ldots, v_j^n)^T$. Assuming that J_j is invertible, (2.21) yields that

$$\mathcal{J}\boldsymbol{\psi} = \boldsymbol{0}\,, \quad \text{where} \quad \mathcal{J} \equiv I + 2\pi\nu\mathcal{G} + \nu\, D\, P_1 + \frac{2\pi\nu D}{\tau} P_2\mathcal{K}_0 \quad \text{and} \quad \mathcal{K}_0 \equiv -\text{diag}\left(\boldsymbol{e}_1^T J_1^{-1}\boldsymbol{e}_1, \ldots, \boldsymbol{e}_1^T J_m^{-1}\boldsymbol{e}_1\right)\,. \tag{2.22}$$

We conclude that $\det\mathcal{J} \neq 0$ owing to the fact that $\mathcal{A}_e$ and $\boldsymbol{u}_{ej}$ for $j = 1, \ldots, m$ is assumed to be a non-degenerate solution of the NAS (2.2) and (2.6). Finally, since it is readily verified that $\mathcal{J} = \mathcal{M}(0)$, where $\mathcal{M}(\lambda)$ is the GCEP matrix in (2.20a), we conclude that $\lambda = 0$ is not a root of (2.20b). □

Proposition 1 implies that branches of non-degenerate solutions to the NAS (2.2) and (2.6) obtained as a parameter is varied cannot lose stability through a zero-eigenvalue crossing of the GCEP (2.20a). This simple observation is the motivation for analzying whether stability can be lost through Hopf bifurcations associated with the linearization.

In terms of the eigenvectors $\boldsymbol{c}$ and eigenvalues $\lambda \in \Lambda(\mathcal{M})$ of the GCEP (2.20), we obtain from (2.8), (2.14) and (2.12) that the linearization around the bulk and intracellular steady-state solutions is, for $\varepsilon \to 0$, given by the superposition

$$U(\boldsymbol{x}, t) \sim U_e - \sum_{\lambda\in\Lambda(\mathcal{M})} e^{\lambda t}\left(\sum_{j=1}^m c_j G_\lambda(\boldsymbol{x};\boldsymbol{x}_j)\right)\,; \qquad \boldsymbol{u}_j(t) \sim \boldsymbol{u}_{ej} + \frac{2\pi D}{\tau}\sum_{\lambda\in\Lambda(\mathcal{M})} e^{\lambda t} c_j\left(\lambda I - J_j\right)^{-1}\boldsymbol{e}_1\,, \quad j = 1, \ldots, m\,, \tag{2.23}$$

where each $\boldsymbol{c} = (c_1, \ldots, c_m)^T$ depends on the particular eigenvalue λ. To relate the diffusive flux into the j-th cell to the components of $\boldsymbol{c}$ we use the the inner solutions (2.1) and (2.11). To determine the effect on the intracellular component that can be transported across the membrane we calculate $\boldsymbol{e}_1^T\boldsymbol{u}_j \equiv u_j^1$ in (2.23). This yields that

$$D\partial_\rho U|_{\rho=1} \sim D\left(A_j + \sum_{\lambda\in\Lambda(\mathcal{M})} c_j e^{\lambda t}\right)\,, \qquad u_j^1 \sim u_{ej}^1 + \frac{2\pi D}{\tau}\sum_{\lambda\in\Lambda(\mathcal{M})}\left(\mathcal{K}\boldsymbol{c}\right)_j e^{\lambda t}\,, \qquad j = 1, \ldots, m\,, \tag{2.24}$$

where $\mathcal{K} \equiv \text{diag}\,(K_1, \ldots, K_m)$, with K_j defined in (2.19). As evident from (2.24), and discussed for various examples in §4.2 and §5.1, the modulus $|(\mathcal{K}\boldsymbol{c})_j|$ and argument $\arg(\mathcal{K}\boldsymbol{c})_j$ of the components of a complex-valued $\mathcal{K}\boldsymbol{c}$, resulting from pure

imaginary eigenvalues with $\mathrm{Re}(\lambda) = 0$ and $\mathrm{Im}(\lambda) \neq 0$, determines the relative amplitudes and phase differences of small scale intracellular oscillations near a Hopf bifurcation of the steady-state solution.

Our linear stability theory for steady-state solutions of PDE-ODE model (1.2) can be applied to any configuration of cells in an arbitrary 2-D bounded domain and for arbitrary local reaction kinetics. However, in our illustrations of the theory below in §4 and §5, we will consider the two-component Sel'kov model, which is used in simple models of glycolysis (cf. [37], [45]). From (1.2c), for an isolated cell with no influx from the bulk, the intracellular dynamics within the j^{th} cell that accounts for efflux from the cell boundary is given by $\mathrm{d}\boldsymbol{u}_j/\mathrm{d}t = \boldsymbol{F}_j(\boldsymbol{u}_j) - 2\pi d_{2j} u_j^1 \boldsymbol{e}_1/\tau$, where $\boldsymbol{u}_j = (u_j^1, u_j^2)^T$ and the Sel'kov kinetics $\boldsymbol{F}_j(v,w) = (F_{j1}(v,w), F_{j2}(v,w))^T$ are defined by

$$F_{j1}(v,w) = \alpha_j w + wv^2 - v\,, \qquad F_{j2}(v,w) = \zeta_j\left[\mu_j - \left(\alpha_j w + wv^2\right)\right]\,. \tag{2.25}$$

The steady-state for this isolated cell is given by $u_j^1 = \mu_j/\chi_j$ and $u_j^2 = \mu_j/\left(\alpha_j + (u_j^1)^2\right)$, where $\chi_j \equiv 1 + 2\pi d_{2j}/\tau$. The determinant and trace of the Jacobian J_{ej} for this isolated cell with boundary efflux is

$$\det(J_{ej}) = \zeta_j\chi_j\left(\alpha_j + \frac{\mu_j^2}{\chi_j^2}\right)\,, \qquad \mathrm{tr}(J_{ej}) = \frac{2\mu_j^2}{\chi_j}\left(\alpha_j + \frac{\mu_j^2}{\chi_j^2}\right)^{-1} - \chi_j - \zeta_j\left(\alpha_j + \frac{\mu_j^2}{\chi_j^2}\right)\,. \tag{2.26}$$

Since $\det(J_{ej}) > 0$, the steady-state for this isolated cell is linearly stable only if $\mathrm{tr}(J_{ej}) < 0$. We will choose Sel'kov kinetic parameters α_j, μ_j and ζ_j so that an isolated cell with zero boundary efflux (i.e. $d_{2j} = 0$) is linearly stable, but with parameters rather close to the stability threshold. A set of such parameters is shown in Fig. 2a where we verify that $\mathrm{tr}(J_{ej}) < 0$ on $0.7 < \alpha_j < 1.0$ when $\mu_j = 2$ and $\zeta_j = 0.15$. The Hopf bifurcation (HB) boundary in the α_j versus μ_j parameter plane, as obtained by setting $\mathrm{tr}(J_{ej}) = 0$ is

$$\alpha_j = -\frac{\mu_j^2}{\chi_j^2} + \frac{1}{2\zeta_j}\left[-\chi_j + \sqrt{\chi_j^2 + \frac{8\zeta_j\mu_j^2}{\chi_j}}\right]\,, \qquad \text{where} \quad \chi_j \equiv 1 + \frac{2\pi d_{2j}}{\tau}\,. \tag{2.27}$$

For an isolated cell, a simple application of the Poincare-Bendixson theorem shows that when the steady-state is unstable the cell will have limit cycle oscillations. When there is no boundary efflux, i.e. $d_{2j} = 0$, this parameter range of periodic solutions is given by the green-shaded region in Fig. 2b. However, no time-periodic oscillations with Sel'kov kinetics are possible when the steady-state is linearly stable. In Fig. 2c we show how the HB boundary for an isolated cell depends on the boundary efflux parameter d_{2j}. As expected, for the fixed value $\mu_j = 2$, the interval in α_j where oscillations are possible is decreased when there is an efflux out of the cell boundary. The shifting of the HB boundaries to the right in Fig. 2c indicates that a greater rate μ_j of production of u_j^2 is needed to ensure oscillations when there is a boundary efflux. The interval in μ_j where oscillations are possible, at least for some range of $\alpha_j > 0$, is $0 < \mu_j < \chi_j^{3/2}/\sqrt{\zeta_j}$.

For the baseline parameter set $\mu_j = 2$ and $\zeta_j = 0.15$, in §4 and §5 we will show that the inter-cell coupling via the bulk diffusion field can be sufficient to trigger an oscillatory instability in the cells through a Hopf bifurcation.

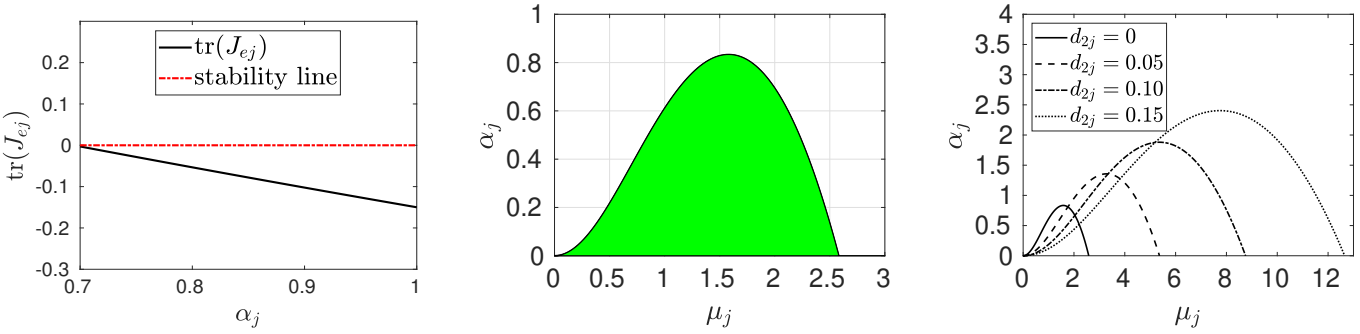

(a) $tr(J_{ej})$ versus α_j for isolated cell *(b) Instability region: isolated cell* *(c) HB boundaries: isolated cell with efflux*

Figure 2: Left panel: $tr(J_{ej})$, from (2.26) versus α_j, for the steady-state of the Sel'kov kinetics (2.25) for an isolated cell, with $\mu_j = 2$ and $\zeta_j = 0.15$. This steady-state is linearly stable but the parameters are close to the stability threshold. Middle panel: Green-shaded region of instability where $tr(J_{ej}) > 0$ in the α_j versus μ_j plane for the steady-state of an isolated cell with no boundary efflux and $\zeta_j = 0.15$. Within this region, a time-periodic solution (limit cycle) occurs for an isolated cell. The HB boundary is given by (2.27) with $d_{2j} = 0$. In the unshaded region the steady-state is linearly stable. Right panel: HB boundaries for an isolated cell (see (2.27)) with $\zeta_j = 0.15$, $\tau = 0.5$ and four boundary efflux parameters. A larger production rate μ_j is needed to support oscillations.

For Sel'kov local reaction kinetics (2.25) it is readily shown that, with an arbitrary arrangement of cells, there is a unique solution to the NAS (2.2) and (2.6) given by

$$u_{ej}^1 = \mu_j + \frac{2\pi D}{\tau}A_j\,, \qquad u_{ej}^2 = \frac{\mu_j}{\alpha_j + \left(u_{ej}^1\right)^2}\,, \qquad j = 1,\ldots,m\,, \tag{2.28a}$$

where $\mathcal{A} = (A_1, \ldots, A_m)^T$ satisfies the linear algebraic system

$$\left(I + 2\pi\nu\mathcal{G} + \nu\, D\, P_1 + \frac{2\pi\nu D}{\tau} P_2 \right) \mathcal{A} = -\nu P_2\, \boldsymbol{\mu}\,, \qquad \text{with} \qquad \boldsymbol{\mu} \equiv (\mu_1, \ldots, \mu_m)^T\,. \tag{2.28b}$$

For $\nu \ll 1$ sufficiently small, the matrix in (2.28b) is invertible, yielding a unique solution for $\mathcal{A}$. For Sel'kov kinetics we conclude that steady-state solutions of the PDE-ODE model (1.2) are always non-degenerate as $\varepsilon \to 0$. As such, since by Proposition 1 stability cannot be lost via a zero-eigenvalue crossing, in §4 and §5 we will focus on analyzing instabilities of the steady-state arising from Hopf bifurcations.

3 A limiting ODE system with global coupling: $D = \mathcal{O}(\nu^{-1})$

In this section, we use a singular perturbation approach to reduce the dimensionless coupled PDE-ODE model (1.2) to an ODE system that is valid for the limiting regime $D = \mathcal{O}(\nu^{-1}) \gg \mathcal{O}(1)$, where $\nu \equiv -1/\log\varepsilon$ and $\varepsilon \ll 1$. This ODE system depends weakly on the spatial configuration of the cells and on the scaled diffusivity $D_0 = \mathcal{O}(1)$, defined by $D = D_0/\nu$.

Consider a collection of m small cells centered at the points $\boldsymbol{x}_1, \ldots, \boldsymbol{x}_m$ in a 2-D bounded domain Ω. Define $\Omega_p \equiv \cup_{j=1}^m \Omega_{\varepsilon_j}$ as the region formed by the union of the cells, and the average bulk concentration $\overline{U} = \overline{U}(t)$ by

$$\overline{U} = \frac{1}{|\Omega \setminus \Omega_p|} \int_{\Omega\setminus\Omega_p} U\, \mathrm{d}\boldsymbol{x}\,. \tag{3.1}$$

Our goal is to derive an ODE for $\overline{U} \equiv \overline{U}(t;\nu)$, accurate to $\mathcal{O}(\nu)$, which is coupled to the intracellular dynamics of the cells, as given in (1.2b). Upon multiplying (1.2a) by $1/|\Omega \setminus \Omega_p|$ and using the divergence theorem, we obtain

$$\tau \overline{U}_t + \overline{U} = \frac{2\pi}{|\Omega \setminus \Omega_p|} \sum_{j=1}^m \left(d_{2j} u_j^1 - \frac{d_{1j}}{2\pi\varepsilon} \int_{\partial\Omega_{\varepsilon_j}} U\, \mathrm{d}s \right)\,, \tag{3.2}$$

where we used $|\partial\Omega_{\varepsilon_j}| = 2\pi\varepsilon$ for the perimeter of each cell. Since $|\Omega_p| = m\pi\varepsilon^2$, we estimate $|\Omega \setminus \Omega_p| = |\Omega| - \mathcal{O}(\varepsilon^2)$, so that $|\Omega \setminus \Omega_p| \to |\Omega|$ as $\varepsilon \to 0$ in (3.2). Next, by evaluating the integral in (1.2b), and using $|\partial\Omega_{\varepsilon_j}| = 2\pi\varepsilon$, we obtain

$$\frac{\mathrm{d}\boldsymbol{u}_j}{\mathrm{d}t} = \boldsymbol{F}_j(\boldsymbol{u}_j) - \frac{2\pi \boldsymbol{e}_1}{\tau} \left(d_{2j} u_j^1 - \frac{d_{1j}}{2\pi\varepsilon} \int_{\partial\Omega_{\varepsilon_j}} U\, \mathrm{d}s \right)\,, \qquad j = 1, \ldots, m\,. \tag{3.3}$$

In (3.2) and (3.3), we must estimate the bulk concentration $U \equiv U(\boldsymbol{x}, t)$ on the j^{th} cell boundary $\partial\Omega_{\varepsilon_j}$.

For $D = \mathcal{O}(\nu^{-1})$ we introduce the scaling

$$D = \frac{D_0}{\nu}, \quad \text{where} \quad \nu \equiv \frac{-1}{\log\varepsilon}\,, \quad \varepsilon \ll 1 \quad \text{and} \quad D_0 = \mathcal{O}(1)\,. \tag{3.4}$$

Upon substituting (3.4) into (1.2), we obtain in the bulk region that

$$\begin{aligned} &\tau U_t = \frac{D_0}{\nu}\, \Delta U - U\,, \qquad t > 0\,, \quad \boldsymbol{x} \in \Omega \setminus \cup_{j=1}^m \Omega_{\varepsilon_j}\,; \\ &\partial_n U = 0, \quad \boldsymbol{x} \in \partial\Omega_\varepsilon\,; \qquad \varepsilon \frac{D_0}{\nu}\, \partial_n U = d_{1j}\, U - d_{2j} u_j^1 \quad \text{on} \quad \partial\Omega_{\varepsilon_j}\,, \qquad j = 1, \ldots, m\,. \end{aligned} \tag{3.5}$$

In the inner region at an $\mathcal{O}(\varepsilon)$ neighborhood of the j^{th} cell, we introduce the inner variables $\boldsymbol{y} = \varepsilon^{-1}(\boldsymbol{x} - \boldsymbol{x}_j)$ and $U(\boldsymbol{x}) = V_j(\boldsymbol{x}_j + \varepsilon\boldsymbol{y};\nu)$, with $\rho = |\boldsymbol{y}|$. Writing (3.5) in terms of these inner variables, we obtain for $\varepsilon \to 0$ that

$$\Delta V_j = 0, \quad \rho \geq 1\,; \qquad \partial_\rho V_j = \frac{\nu}{D_0} \Big(d_{1j}\, V_j - d_{2j}\, u_j^1 \Big)\,, \quad \text{on} \quad \rho = 1\,, \qquad j = 1, \ldots, m\,, \tag{3.6}$$

which has the radially symmetric solution

$$V_j = \nu\, b_j \log\rho + U_j^0\,, \qquad \text{where} \qquad b_j \equiv \frac{1}{D_0} \Big(d_{1j}\, U_j^0 - d_{2j}\, u_j^1 \Big)\,, \qquad j = 1, \ldots, m\,, \tag{3.7}$$

where $V_j|_{\rho=1} = U_j^0$ is to be determined. By writing (3.7) in the outer $\boldsymbol{x}$ variable, and using $|\boldsymbol{y}| = \varepsilon^{-1}|\boldsymbol{x} - \boldsymbol{x}_j|$, we obtain the following asymptotic matching condition for the outer solution in the bulk region:

$$U \sim \nu\, b_j \log|\boldsymbol{x} - \boldsymbol{x}_j| + \Big(\frac{d_{1j}}{D_0} + 1 \Big) U_j^0 - \frac{d_{2j}}{D_0}\, u_j^1\,, \qquad \text{as} \qquad \boldsymbol{x} \to \boldsymbol{x}_j\,. \tag{3.8}$$

Since $V_j(\rho) = U_j^0$ on $\rho = 1$ from (3.7), we have $\int_{\partial\Omega_{\varepsilon_j}} U\,\mathrm{d}s = \varepsilon \int_0^{2\pi} V_j|_{\rho=1}\,\mathrm{d}\theta = 2\pi\varepsilon\, U_j^0$. Then, from (3.2) and (3.3), and recalling (3.7) for b_j, we obtain for $\varepsilon \to 0$ that

$$\begin{aligned} \tau \overline{U}_t + \overline{U} &= \frac{2\pi}{|\Omega|}\sum_{j=1}^{m}\left(d_{2j}u_j^1 - d_{1j}U_j^0\right) = -\frac{2\pi D_0}{|\Omega|}\sum_{j=1}^{m} b_j\,, \\ \frac{\mathrm{d}\boldsymbol{u}_j}{\mathrm{d}t} - \boldsymbol{F}_j(\boldsymbol{u}_j) &= -\frac{2\pi \boldsymbol{e}_1}{\tau}\left(d_{2j}u_j^1 - d_{1j}U_j^0\right) = \frac{2\pi D_0}{\tau}\boldsymbol{e}_1 b_j\,, \qquad j = 1,\ldots,m\,. \end{aligned} \tag{3.9}$$

To complete the derivation of the ODE system we must obtain an algebraic system for b_j for $j = 1,\ldots,m$ from the analysis of the outer solution. From (3.5) and (3.8), and relating U_j^0 to b_j using (3.7), the outer problem for $U(\boldsymbol{x},t)$ is

$$\begin{aligned} &\tau U_t = \frac{D_0}{\nu}\,\Delta U - U\,, \quad t > 0\,, \quad \boldsymbol{x} \in \Omega \setminus \cup_{j=1}^m \Omega_{\varepsilon_j}\,; \qquad \partial_n U = 0\,, \quad \boldsymbol{x} \in \Omega\,; \\ &U \sim \nu b_j \log|\boldsymbol{x} - \boldsymbol{x}_j| + b_j\left(1 + \frac{D_0}{d_{1j}}\right) + \frac{d_{2j}}{d_{1j}}u_j^1\,, \qquad \text{as} \qquad \boldsymbol{x} \to \boldsymbol{x}_j\,. \end{aligned} \tag{3.10}$$

We then expand $U(\boldsymbol{x},t)$ as

$$U(\boldsymbol{x},t) = \overline{U} + \frac{\nu}{D_0}U_1(\boldsymbol{x},t) + \ldots\,, \qquad \text{where} \quad \int_\Omega U_1\,d\boldsymbol{x} = 0\,. \tag{3.11}$$

The zero average constraint on U_1 ensures that $\overline{U}$ is the spatial average of U to terms of order $\mathcal{O}(\nu)$. Upon substituting (3.11) into (3.10), we obtain in the sense of distributions that U_1 satisfies

$$\begin{aligned} &\Delta U_1 = \tau\,\overline{U}_t + \overline{U} + 2\pi D_0\sum_{i=1}^{m} b_i\delta(\boldsymbol{x} - \boldsymbol{x}_i)\,, \quad \boldsymbol{x} \in \Omega\,; \qquad \partial_n U_1 = 0\,, \quad \boldsymbol{x} \in \partial\Omega\,; \\ &U_1 \sim b_j D_0 \log|\boldsymbol{x} - \boldsymbol{x}_j| - \frac{D_0}{\nu}\overline{U} + \frac{D_0}{\nu}\left[b_j\Big(1 + \frac{D_0}{d_{1j}}\Big) + \frac{d_{2j}}{d_{1j}}\,u_j^1\right]\,, \qquad \text{as} \qquad \boldsymbol{x} \to \boldsymbol{x}_j\,. \end{aligned} \tag{3.12}$$

The divergence theorem applied to (3.12) yields the ODE given in (3.9) while the linear system for b_j, for $j = 1,\ldots,m$, is obtained from the constraints involved with specifying the form of the regular part of the singularity behavior in (3.12).

The solution to (3.12), with $\int_\Omega U_1\,d\boldsymbol{x} = 0$ is written as

$$U_1 = -2\pi D_0\sum_{i=1}^{m} b_i\,G_0(\boldsymbol{x};\boldsymbol{x}_i)\,, \tag{3.13}$$

where $G_0(\boldsymbol{x};\boldsymbol{x}_j)$ is the unique Neumann Green's function satisfying

$$\Delta G_0 = \frac{1}{|\Omega|} - \delta(\boldsymbol{x} - \boldsymbol{x}_j)\,, \quad \boldsymbol{x} \in \Omega\,; \qquad \partial_n G_0 = 0\,, \quad \boldsymbol{x} \in \partial\Omega\,; \tag{3.14a}$$

$$G_0(\boldsymbol{x};\boldsymbol{x}_j) \sim -\frac{1}{2\pi}\log|\boldsymbol{x} - \boldsymbol{x}_j| + R_{0j} + o(1)\,, \quad \text{as} \quad \boldsymbol{x} \to \boldsymbol{x}_j\,, \quad \text{and} \quad \int_\Omega G_0\,\mathrm{d}\boldsymbol{x} = 0\,. \tag{3.14b}$$

Here R_{0j} is the regular part of G_0 at $\boldsymbol{x} = \boldsymbol{x}_j$. By expanding (3.13) as $\boldsymbol{x} \to \boldsymbol{x}_j$, we enforce that the nonsingular part of the resulting expression agrees with that in (3.12). This yields that

$$b_j\left(1 + \frac{D_0}{d_{1j}}\right) + 2\pi\nu\left(b_j R_{0j} + \sum_{i\neq j}^{m} b_i G_{0ji}\right) = \overline{U} - \frac{d_{2j}}{d_{1j}}u_j^1\,, \qquad j = 1,\ldots,m\,, \tag{3.15}$$

where $G_{0ji} = G_0(\boldsymbol{x}_j;\boldsymbol{x}_i)$. This linear system for $b_1,\ldots,b_m$ is then coupled to the ODEs given in (3.9). Upon writing this ODE system in matrix form we summarize the result as follows:

Proposition 2. *Let $\varepsilon \to 0$ and assume that $D = D_0/\nu \gg 1$ where $D_0 = \mathcal{O}(1)$ and $\nu = -1/\log\varepsilon \ll 1$. Then, the PDE-ODE system (1.2) reduces to the following $nm+1$ dimensional ODE system for $\overline{U} \approx |\Omega|^{-1}\int_\Omega U\,d\boldsymbol{x}$ and the intracellular species:*

$$\frac{d}{dt}\overline{U} = -\frac{1}{\tau}\overline{U} - \frac{2\pi D_0}{\tau|\Omega|}\boldsymbol{e}^T\boldsymbol{b}\,; \qquad \frac{d\boldsymbol{u}_j}{dt} = \boldsymbol{F}_j(\boldsymbol{u}_j) + \frac{2\pi D_0\boldsymbol{e}_1}{\tau}b_j\,, \qquad j = 1,\ldots,m\,, \tag{3.16a}$$

where $\boldsymbol{e} \equiv (1,\ldots,1)^T$, $\boldsymbol{e}_1 \equiv (1,0,\ldots,0)^T$ and $\boldsymbol{b} \equiv (b_1,\ldots,b_m)^T$. In (3.16a), $\boldsymbol{b}$ is the solution to the linear system

$$\big(I + D_0 P_1 + 2\pi\nu\,\mathcal{G}_0\big)\boldsymbol{b} = \overline{U}\,\boldsymbol{e} - P_2\,\boldsymbol{u}^1\,, \tag{3.16b}$$

where $\boldsymbol{u}^1 \equiv (u_1^1, \ldots, u_m^1)^T$ *and* P_1 *and* P_2 *are the diagonal matrices defined in terms of the permeabilities by (2.7). In (3.16b),* $\mathcal{G}_0$ *is the Neumann Green's matrix with matrix entries*

$$(\mathcal{G}_0)_{ij} = (\mathcal{G}_0)_{ji} = G_0(\boldsymbol{x}_i, \boldsymbol{x}_j)\,, \quad i \neq j \qquad \text{and} \quad (G_0)_{jj} = R_{0j}\,. \tag{3.17}$$

For $\nu \ll 1$*, this ODE system is equivalent up to* $\mathcal{O}(\nu)$ *terms to*

$$\begin{aligned} \frac{d}{dt}\overline{U} &= -\frac{1}{\tau}\overline{U} - \frac{2\pi}{\tau|\Omega|}\left[\overline{U}\boldsymbol{e}^T\mathcal{C}\boldsymbol{e} - \boldsymbol{e}^T\mathcal{C}P_2\,\boldsymbol{u}^1\right] + \mathcal{O}(\nu^2)\,, \\ \frac{d\boldsymbol{u}_j}{dt} &= \boldsymbol{F}_j(\boldsymbol{u}_j) + \frac{2\pi\boldsymbol{e}_1}{\tau}\left[\overline{U}\,(\mathcal{C}\boldsymbol{e})_j - \left(\mathcal{C}P_2\,\boldsymbol{u}^1\right)_j\right]\,, \qquad j = 1, \ldots, m\,, \end{aligned} \tag{3.18a}$$

where the matrix $\mathcal{C}$ *is defined in terms of* $\mathcal{G}_0$ *and a diagonal matrix* $\mathcal{P}$ *by*

$$\mathcal{C} \equiv \mathcal{P} - \frac{2\pi\nu}{D_0}\mathcal{P}\mathcal{G}_0\mathcal{P}\,, \qquad \mathcal{P} \equiv diag\left(\frac{D_0 d_{11}}{d_{11}+D_0}, \ldots, \frac{D_0 d_{1m}}{d_{1m}+D_0}\right)\,. \tag{3.18b}$$

In the well-mixed limit for which $D_0 \to \infty$*, (3.16b) yields* $D_0 b_j \sim \overline{U}d_{1j} - d_{2j}u_j^1$*, so that (3.16a) reduces to*

$$\overline{U}_t = -\frac{1}{\tau}\overline{U} - \frac{2\pi}{\tau|\Omega|}\sum_{j=1}^{m}(\overline{U}d_{1j} - d_{2j}u_j^1)\,; \qquad \frac{d\boldsymbol{u}_j}{dt} = \boldsymbol{F}_j(\boldsymbol{u}_j) + \frac{2\pi\boldsymbol{e}_1}{\tau}(\overline{U}d_{1j} - d_{2j}u_j^1)\,, \qquad j = 1, \ldots, m\,. \tag{3.19}$$

To derive (3.18) from (3.16), we approximate the solution $\boldsymbol{b}$ to (3.16b) up to terms of order $\mathcal{O}(\nu)$. By inverting the diagonal matrix $I + D_0P_1$, we obtain from (3.16b) that

$$\boldsymbol{b} = \frac{1}{D_0}\left(I + \frac{2\pi\nu}{D_0}\mathcal{P}\mathcal{G}_0\right)^{-1}\left(\overline{U}\mathcal{P}\boldsymbol{e} - \mathcal{P}P_2\boldsymbol{u}^1\right) \sim \frac{1}{D_0}\left(I - \frac{2\pi\nu}{D_0}\mathcal{P}\mathcal{G}_0\right)\left(\overline{U}\mathcal{P}\boldsymbol{e} - \mathcal{P}P_2\boldsymbol{u}^1\right) = \frac{1}{D_0}\left(\overline{U}\mathcal{C}\boldsymbol{e} - \mathcal{C}P_2\boldsymbol{u}^1\right) + \mathcal{O}(\nu^2)\,, \tag{3.20}$$

where $\mathcal{C}$ and $\mathcal{P}$ are given in (3.18b). The ODE system (3.18) results from substituting (3.20) into (3.16).

The ODE systems (3.16), or alternatively (3.18), for the regime $D = \mathcal{O}(\nu^{-1})$ are accurate up to and including terms of order $\mathcal{O}(\nu)$ and show how the intracellular species are globally coupled through the spatial average of the bulk field. Since these ODE systems depend on the scaled diffusivity parameter D_0 and include the effect of the spatial configuration $\boldsymbol{x}_1, \ldots, \boldsymbol{x}_m$ of the cells through the Neumann Green's matrix, these ODE systems can account for both diffusion-mediated and quorum-sensing behavior (see §4 and §5). In contrast, the limiting well-mixed ODE system (3.19), originally derived in [20] for the simpler case of identical cells, depends only on the number m of cells. As a result, the well-mixed ODE dynamics is independent of the diffusivity and the spatial configuration of the cells.

In our numerical experiments in §4 and §5 using the ODE system (3.16) the domain Ω is the unit disk. For the unit disk, the Neumann Green's function $G_0(\boldsymbol{x};\boldsymbol{x}_j)$ and its regular part R_{0j}, satisfying (3.14), are (see equation (4.3) of [28])

$$\begin{aligned} G_0(\boldsymbol{x};\boldsymbol{x}_j) &= -\frac{1}{2\pi}\log|\boldsymbol{x}-\boldsymbol{x}_j| - \frac{1}{4\pi}\log\left(|\boldsymbol{x}|^2|\boldsymbol{x}_j|^2 + 1 - 2\boldsymbol{x}\cdot\boldsymbol{x}_j\right) + \frac{(|\boldsymbol{x}|^2 + |\boldsymbol{x}_j|^2)}{4\pi} - \frac{3}{8\pi}, \\ R_{0j} &= -\frac{1}{2\pi}\log\left(1 - |\boldsymbol{x}_j|^2\right) + \frac{|\boldsymbol{x}_j|^2}{2\pi} - \frac{3}{8\pi}\,. \end{aligned} \tag{3.21}$$

For an arbitrary cell pattern $\{\boldsymbol{x}_1, \ldots, \boldsymbol{x}_m\}$, (3.21) is used to evaluate the Neumann Green's matrix $\mathcal{G}_0$ as needed in (3.16).

4 A ring and center cell pattern

With Sel'kov reaction kinetics, we apply the theory developed in §2 to a ring and center cell configuration in the unit disk. This pattern is characterized by $m - 1 \geq 2$ equally spaced cells on a concentric ring within the unit disk, and with one at the center of the disk (see Fig. 3). For this pattern, the GCEP (2.20) will be used to obtain tractable nonlinear algebraic equations that can be solved numerically to compute HB boundaries in the τ versus D parameter plane. In addition, a winding number criterion is developed to count the number of unstable eigenvalues in open regions of this parameter plane. Some of our examples will show that rather small changes in either the permeabilities or reaction kinetic parameters of the center cell can significantly alter the region in parameter space where oscillations occurs.

4.1 Analysis of the GCEP

Consider a ring and center cell pattern of m cells where the cells on the ring of radius r_0 have identical parameters, but where the center cell has possibly different permeabilities or Sel'kov kinetic parameters (see Fig. 3). The cell centers are at

$$\boldsymbol{x}_j = r_0\left(\cos\left(\frac{2\pi(j-1)}{(m-1)}\right),\ \sin\left(\frac{2\pi(j-1)}{(m-1)}\right)\right)\,, \quad j = 1\,, \ldots, m-1\,; \qquad \boldsymbol{x}_m = \boldsymbol{0}\,, \tag{4.1}$$

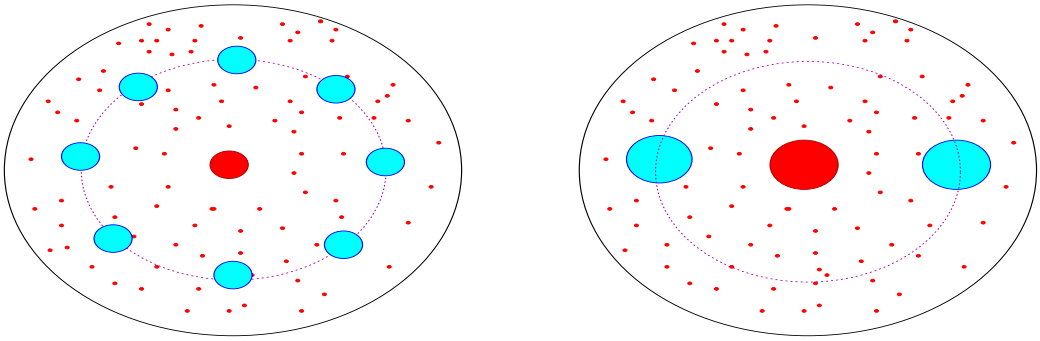

Figure 3: Schematic showing a ring and center cell configuration of $m = 9$ (left) and $m = 3$ (right) cells in the unit disk. The ring cells are identical and equally spaced on a concentric ring within the disk (in cyan). The center cell (in red), possibly has different parameters. The red dots represent the signaling molecules secreted in the bulk region by the cells.

where $0 < r_0 < 1$. For this pattern, the reduced-wave Green's matrix $\mathcal{G}$ in (2.7) can be partitioned as

$$\mathcal{G} = \left(\begin{array}{ccc|c} & \mathcal{G}_{m-1} & & \begin{array}{c} g_m \\ \vdots \\ g_m \end{array} \\ \hline g_m & \cdots & g_m & R_m \end{array}\right); \qquad g_m \equiv G(\boldsymbol{x}_j, \boldsymbol{x}_m) = G(\boldsymbol{x}_m, \boldsymbol{x}_j)\,, \quad j = 1\ldots, m-1\,, \quad R_m = R(\boldsymbol{x}_m)\,. \tag{4.2}$$

Here $\mathcal{G}_{m-1}$ is the $(m-1)\times(m-1)$ symmetric matrix block representing the interaction between the cells on the ring. Since this block is also cyclic it has the eigenpair

$$\mathcal{G}_{m-1}\boldsymbol{e} = \omega_1 \boldsymbol{e}\,, \qquad \text{with} \qquad \boldsymbol{e} = (1,\ldots,1)^T \in \mathbb{R}^{m-1}\,, \quad \text{and} \quad \omega_1 \equiv R_1 + \sum_{j=2}^{m-1} G(\boldsymbol{x}_1, \boldsymbol{x}_j)\,. \tag{4.3}$$

In (4.2) there is a common interaction, represented by g_m, between each ring cell and the center cell owing to the rotational symmetry and the fact that the ring cells are all equidistant from the center cell.

For the identical ring cells, we label their permeabilities as $d_1 = d_{1j}$ and $d_2 = d_{2j}$ for $j = 1,\ldots,m-1$ and their common Sel'kov kinetic parameters as $\mu_1 = \mu_j$, $\alpha_1 = \alpha_j$ and $\zeta_1 = \zeta_j$ for $j = 1,\ldots,m-1$. Since the unique steady-state solution to (2.28b) has the form $\mathcal{A} = (A_c,\ldots,A_c,A_m)^T$, we readily find that A_c and A_m satisfies the 2×2 linear system

$$\left(1 + \frac{\nu D}{d_1} + 2\pi\nu\omega_1 + \frac{2\pi\nu D}{\tau}\frac{d_2}{d_1}\right)A_c + 2\pi\nu g_m\, A_m = -\nu\mu_1\frac{d_2}{d_1}\,; \tag{4.4a}$$

$$\left(1 + \frac{\nu D}{d_{1m}} + 2\pi\nu R_m + \frac{2\pi\nu D}{\tau}\frac{d_{2m}}{d_{1m}}\right)A_m + 2\pi\nu\, g_m\,(m-1)A_c = -\nu\mu_m\frac{d_{2m}}{d_{1m}}\,, \tag{4.4b}$$

where ω_1 is the eigenvalue of $\mathcal{G}_{m-1}$ in (4.3). In terms of $\mathcal{A} = (A_c,\ldots,A_c,A_m)^T$, the steady-state for the intracellular species as obtained from (2.28a) is

$$u^1_{ej} = \begin{cases} u^1_{e1} \equiv \mu_1 + \frac{2\pi D}{\tau}A_c\,, & j = 1\,,\ldots,m-1\,, \\ u^1_{em} \equiv \mu_m + \frac{2\pi D}{\tau}A_m\,, & j = m\,, \end{cases}; \qquad u^2_{ej} = \begin{cases} u^2_{e1} \equiv \frac{\mu_1}{\alpha_1 + (u^1_{e1})^2}\,, & j = 1\,,\ldots,m-1\,, \\ u^2_{em} \equiv \frac{\mu_m}{\alpha_m + (u^1_{em})^2}\,, & j = m\,. \end{cases} \tag{4.5}$$

Next, we determine the GCEP for the ring and center cell pattern using (2.20a). For this pattern, the GCEP matrix $\mathcal{M}(\lambda)$ in (2.20a) is written as

$$\mathcal{M}(\lambda) = 2\pi\nu\,\mathcal{G}_\lambda + \mathcal{M}_0\,, \tag{4.6a}$$

where $\mathcal{G}_\lambda$ is the eigenvalue-dependent Green's matrix, as defined in (2.17), and where the diagonal $\mathcal{M}_0$ is defined by

$$\mathcal{M}_0 = \begin{pmatrix} M_0 & & & \\ & \ddots & & \\ & & M_0 & \\ & & & M_m \end{pmatrix}, \qquad \text{where} \qquad \begin{cases} M_0 \equiv 1 + \frac{\nu D}{d_1} + \frac{2\pi\nu D}{\tau}\frac{d_2}{d_1}K_c\,, \\ \\ M_m \equiv 1 + \frac{\nu D}{d_{1m}} + \frac{2\pi\nu D}{\tau}\frac{d_{2m}}{d_{1m}}K_m\,. \end{cases} \tag{4.6b}$$

Here $K_c = K_c(\lambda)$ and $K_m = K_m(\lambda)$ are the entries of the $m\times m$ diagonal matrix $\mathcal{K} = \mathrm{diag}(K_c,\ldots,K_c,K_m)$ defined in (2.19a). For the Sel'kov kinetics given in (2.25), (2.19a) yields

$$K_c \equiv \frac{\lambda + \det(J_1)}{\lambda^2 - \mathrm{tr}(J_1)\lambda + \det(J_1)}\,, \qquad K_m \equiv \frac{\lambda + \det(J_m)}{\lambda^2 - \mathrm{tr}(J_m)\lambda + \det(J_m)}\,, \tag{4.7a}$$

where the trace and determinant of the Jacobians of the intracellular dynamics for the identical ring cells and the center cell are given in terms of the steady-state values in (4.5) by

$$\det(J_1) = \zeta_1\left(\alpha_1 + (u^1_{e1})^2\right), \qquad \det(J_m) = \zeta_m\left(\alpha_m + (u^1_{em})^2\right),$$
$$\mathrm{tr}(J_1) = \frac{\left[2(u^1_{e1})\mu_1 - \left(\alpha_1 + (u^1_{e1})^2\right) - \zeta_1\left(\alpha_1 + (u^1_{e1})^2\right)^2\right]}{\alpha_1 + (u^1_{e1})^2}, \quad \mathrm{tr}(J_m) = \frac{\left[2(u^1_{em})\mu_m - \left(\alpha_m + (u^1_{em})^2\right) - \zeta_m\left(\alpha_m + (u^1_{em})^2\right)^2\right]}{\alpha_m + (u^1_{em})^2}. \tag{4.7b}$$

From Proposition 1, discrete eigenvalues λ associated with the ring and center cell pattern are roots of $\det\mathcal{M}(\lambda) = 0$. A convenient way to implement this determinant root-finding problem numerically is to use the special structure of $\mathcal{M}(\lambda)$ in order to determine explicit formulae for its matrix spectrum $\mathcal{M}(\lambda)\boldsymbol{c}_j = \sigma_j\boldsymbol{c}_j$, for $j = 1,\ldots,m$, where $\sigma_j = \sigma_j(\lambda)$. Then, we need only numerically solve the scalar root-finding problems $\sigma_j(\lambda) = 0$ for λ for each $j = 1,\ldots,m$.

To do so, we use the convenient fact that $\mathcal{G}_\lambda$ can be partitioned, similar to that in (4.2), as

$$\mathcal{G}_\lambda = \left(\begin{array}{ccc:c} & \mathcal{G}_{\lambda(m-1)} & & g_{\lambda m} \\ & & & \vdots \\ & & & g_{\lambda m} \\ \hdashline g_{\lambda m} & \cdots & g_{\lambda m} & R_{\lambda m} \end{array}\right); \qquad g_{\lambda m} \equiv G_\lambda(\boldsymbol{x}_j,\boldsymbol{x}_m) = G_\lambda(\boldsymbol{x}_m,\boldsymbol{x}_j), \quad j = 1\ldots,m-1, \quad R_{\lambda m} \equiv R_\lambda(\boldsymbol{x}_m), \tag{4.8}$$

where G_λ is the eigenvalue-dependent reduced-wave Green's function with regular part R_λ satisfying (2.15). In (4.8), the $(m-1)\times(m-1)$ matrix block $\mathcal{G}_{\lambda(m-1)}$, representing cell interactions on the ring, is symmetric and cyclic. As a result, it has the well-defined eigenspace

$$\mathcal{G}_{\lambda(m-1)}\,\boldsymbol{v}_j = \omega_{\lambda j}\,\boldsymbol{v}_j, \quad j = 1,\ldots,m-1; \qquad \boldsymbol{e}^T\boldsymbol{v}_j = 0, \quad j = 1,\ldots,m-2, \quad \boldsymbol{v}_{m-1} = \boldsymbol{e} \equiv (1,\ldots,1)^T \in \mathbb{R}^{m-1}. \tag{4.9}$$

By using this special matrix structure, it readily follows that the GCEP matrix $\mathcal{M}(\lambda)$ in (4.6) admits $m-2$ *anti-phase modes*, characterized by eigenvectors of the form $\boldsymbol{c}_j = (\boldsymbol{v}_j, 0)^T \in \mathbb{R}^m$ where $\boldsymbol{v}_j \in \mathbb{R}^{m-1}$ are those eigenvectors of $\mathcal{G}_{\lambda(m-1)}$ in (4.9), which satisfy $\boldsymbol{e}^T\boldsymbol{v}_j = 0$ for $j = 1,\ldots,m-2$. With this choice, (4.6) becomes

$$\begin{pmatrix} 2\pi\nu\mathcal{G}_{\lambda(m-1)}\boldsymbol{v}_j + M_0\boldsymbol{v}_j \\ \\ 2\pi\nu g_{\lambda m}\,\boldsymbol{e}^T\boldsymbol{v}_j \end{pmatrix} = \begin{pmatrix} \sigma_j\boldsymbol{v}_j \\ \\ 0 \end{pmatrix}, \quad \text{for} \quad j = 1,\ldots,m-2. \tag{4.10}$$

Since $\boldsymbol{e}^T\boldsymbol{v}_j = 0$ for $j = 1,\ldots,m-2$, we obtain from (4.10), (4.9) and (4.6b) that $m-2$ eigenpairs of $\mathcal{M}(\lambda)$ are

$$\sigma_j = 2\pi\nu\omega_{\lambda j} + M_0 = 2\pi\nu\omega_{\lambda j} + 1 + \frac{\nu D}{d_1} + \frac{2\pi\nu D}{\tau}\frac{d_2}{d_1}K_c, \quad \boldsymbol{c}_j = (\boldsymbol{v}_j, 0)^T, \quad \text{for} \quad j = 1,\ldots,m-2, \tag{4.11}$$

where $K_c = K_c(\lambda)$ is defined in (4.7a). We remark that since K_c depends on the steady-state values A_c and A_m, as obtained from the linear system (4.4), this term depends on the permeabilities and local kinetics of the center cell. Discrete eigenvalues λ for the anti-phase modes are union of the zeroes of $\sigma_j(\lambda) = 0$ for $j = 1,\ldots,m-2$.

For the remaining two eigenpairs of the GCEP matrix $\mathcal{M}(\lambda)$ the associated eigenvector $\boldsymbol{c}$ has the form $\boldsymbol{c} = (\boldsymbol{e},\gamma)^T$ for some scalar γ to be determined and $\boldsymbol{e} = (1,\ldots,1)^T \in \mathbb{R}^{m-1}$. This eigenvector is referred to as the *in-phase mode* since any instability associated with this mode has the same phase for the cells on the ring. With this choice, (4.6) reduces to

$$\begin{pmatrix} \omega_{\lambda(m-1)} + M_0/(2\pi\nu) & g_{\lambda m} \\ (m-1)g_{\lambda m} & R_{\lambda m} + M_m/(2\pi\nu) \end{pmatrix}\begin{pmatrix} 1 \\ \gamma \end{pmatrix} = \frac{\sigma}{2\pi\nu}\begin{pmatrix} 1 \\ \gamma \end{pmatrix}, \tag{4.12}$$

where $\mathcal{G}_{\lambda(m-1)}\boldsymbol{e} = \omega_{\lambda(m-1)}\boldsymbol{e}$ from (4.9).

Upon eliminating σ from the 2×2 matrix problem (4.12) we obtain that $\gamma_\pm$ are the roots of the quadratic equation

$$\gamma^2 + \frac{1}{2\pi\nu g_{\lambda m}}\Big[(M_0 - M_m) + 2\pi\nu(\omega_{\lambda(m-1)} - R_{\lambda m})\Big]\gamma - (m-1) = 0, \tag{4.13}$$

given by

$$\gamma_\pm = -\frac{\beta_\lambda}{2} \pm \frac{1}{2}\sqrt{\beta_\lambda^2 + 4(m-1)}, \qquad \text{where} \qquad \beta_\lambda \equiv \frac{1}{2\pi\nu g_{\lambda m}}\Big[(M_0 - M_m) + 2\pi\nu(\omega_{\lambda(m-1)} - R_{\lambda m})\Big]. \tag{4.14}$$

Since $\gamma_+\gamma_- = -(m-1) > 0$, but with $\gamma_\pm$ possibly complex-valued, we confirm that the two possible in-phase modes $\boldsymbol{c}_\pm = (1,\ldots,1,\gamma_\pm)^T$ are orthogonal. The two eigenvalues $\sigma = \sigma_\pm(\lambda)$, given by $\sigma_\pm \equiv 2\pi\nu\big(\omega_{\lambda(m-1)} + \gamma_\pm\, g_{\lambda m}\big) + M_0$, can be written as

$$\sigma_\pm(\lambda) = \frac{(h_1+h_2)}{2} \pm \frac{1}{2}\sqrt{(h_1-h_2)^2 + 16\pi^2\nu^2(m-1)g_{\lambda m}^2}, \quad \text{where} \quad h_1 \equiv 2\pi\nu\,\omega_{\lambda(m-1)} + M_0, \quad h_2 \equiv 2\pi\nu\,R_{\lambda m} + M_m. \tag{4.15}$$

Here $M_0 = M_0(\lambda)$ and $M_m = M_m(\lambda)$ are given in (4.6b) and $\omega_{\lambda(m-1)}$ is defined by $\mathcal{G}_{\lambda(m-1)}\boldsymbol{e} = \omega_{\lambda(m-1)}\boldsymbol{e}$ from (4.9).

Alternatively, rather than solving (4.12) for $\sigma_\pm$, and then setting $\sigma_\pm(\lambda) = 0$ by using a root-finder for λ, we can more directly conclude that $\mathcal{M}(\lambda)\boldsymbol{c} = \boldsymbol{0}$ for $\boldsymbol{c} = (\boldsymbol{e}, \gamma)^T$ if and only if the determinant of the 2×2 matrix in (4.12) vanishes. In this way, a discrete eigenvalue λ of the GCEP (2.20) for the in-phase mode, which satisfies $\det(\mathcal{M}(\lambda)) = 0$, is a root of $\mathcal{H}_c(\lambda) = 0$ defined by

$$\mathcal{H}_c(\lambda) = \left(\omega_{\lambda(m-1)} + \frac{M_0}{2\pi\nu}\right)\left(R_{\lambda m} + \frac{M_m}{2\pi\nu}\right) - (m-1)g_{\lambda m}^2\,. \tag{4.16}$$

For any root of (4.16), the corresponding eigenvector $\boldsymbol{c}$ of $\mathcal{M}(\lambda)$ is

$$\boldsymbol{c} = (1,\ldots,1,\gamma)^T\,, \qquad \gamma = -\frac{1}{g_{\lambda m}}\left(\omega_{\lambda(m-1)} + \frac{M_0}{2\pi\nu}\right)\,. \tag{4.17}$$

It is readily verified using (4.15) that if $\lambda^\star$ satisfies either $\sigma_+(\lambda^\star) = 0$ or $\sigma_-(\lambda^\star) = 0$, then we must have $\mathcal{H}_c(\lambda^\star) = 0$. In contrast, if $\lambda^\star$ satisfies $\mathcal{H}_c(\lambda^\star) = 0$, then we can only conclude that *either* $\sigma_+(\lambda^\star) = 0$ or $\sigma_-(\lambda^\star) = 0$. Therefore, in implementing a root-finding strategy based on the single scalar equation (4.16) instead of the two scalar equations (4.15) care must be taken to identify all possible roots of $\mathcal{H}_c(\lambda) = 0$ for the same parameter set.

We summarize our result for eigenvalues λ of the GCEP (2.20) for a ring and center cell pattern as follows:

Proposition 3. *Consider a ring and center hole pattern of $m \geq 3$ cells in the unit disk with cell centers at (4.1). The set $\Lambda(\mathcal{M})$ as obtained from the GCEP (2.20), and which approximates as $\varepsilon \to 0$ all the discrete eigenvalues of the linearization of the PDE-ODE system (1.2) around the steady-state solution, is*

$$\Lambda(\mathcal{M}) \equiv \left\{\lambda \mid \bigcup_{j=1}^{m-2}\{\,\sigma_j(\lambda) = 0\,\}\,,\ \bigcup\{\sigma_\pm(\lambda) = 0\}\right\}. \tag{4.18}$$

Here $\sigma_j(\lambda)$, for $j = 1,\ldots,m-2$, for the anti-phase modes are defined in (4.11), while $\sigma_\pm(\lambda)$ for the in-phase modes are defined in (4.15). As shown in Remark 1 of Appendix A, due to mode degeneracy of $\mathcal{G}_{\lambda(m-1)}$, there are $(m-1)/2$ distinct anti-phase modes if m is odd and $(m-2)/2$ distinct anti-phase modes if m is even.

For the unit disk, where an infinite series representation of the solution to (2.15) is available, explicit formulae for the eigenvalues $\omega_{\lambda j}$ of $\mathcal{G}_{\lambda(m-1)}$, as needed in (4.11) and (4.15), are given in Appendix A. The result in Remark 1 of Appendix A regarding mode degeneracy results from the fact that $\mathcal{G}_{\lambda(m-1)}$ is both symmetric and cyclic. In Appendix A we also show how to readily calculate the quantities in (4.2) and (4.3), which are needed in (4.4) for determining the steady-state.

As indicated by Proposition 1, stability boundaries in the τ versus D parameter space for the steady-state under Sel'kov kinetics are determined by HB boundaries where $\lambda = i\lambda_I \in \Lambda(\mathcal{M})$. To determine Hopf bifurcation boundaries for the anti-phase modes we set $\mathrm{Re}(\sigma_j(i\lambda_I)) = 0$ and $\mathrm{Im}(\sigma_j(i\lambda_I)) = 0$ for $j = 1,\ldots,m-2$ in (4.11). Upon separating real and imaginary parts in (4.7a) we obtain the following nonlinear algebraic system for each $j = 1,\ldots,m-2$:

$$2\pi\nu\,\mathrm{Re}(\omega_{\lambda j}) + \left(1 + \nu\frac{D}{d_1}\right) + \frac{2\pi\nu D}{\tau}\frac{d_2}{d_1}\,\mathrm{Re}(K_c(i\lambda_I)) = 0\,, \qquad \mathrm{Im}(\omega_{\lambda j}) + \frac{D}{\tau}\frac{d_2}{d_1}\,\mathrm{Im}(K_c(i\lambda_I)) = 0\,, \tag{4.19a}$$

where

$$\mathrm{Im}(K_c(i\lambda_I)) = \frac{\lambda_I(\det(J_1) - \lambda_I^2) + \lambda_I\det(J_1)\mathrm{tr}(J_1)}{(\det(J_1) - \lambda_I^2)^2 + (\lambda_I\,\mathrm{tr}(J_1))^2}\,, \quad \mathrm{Re}(K_c(i\lambda_I)) = \frac{\det(J_1)(\det(J_1) - \lambda_I^2) - \lambda_I^2\,\mathrm{tr}(J_1)}{(\det(J_1) - \lambda_I^2)^2 + (\lambda_I\,\mathrm{tr}(J_1))^2}\,. \tag{4.19b}$$

Here J_1 is the Jacobian of the Sel'kov kinetics for the ring cells with determinant and trace given in (4.7b). Similarly, the Hopf bifurcation boundaries for the in-phase modes are obtained by setting $\sigma_\pm(i\lambda_I) = 0$ in (4.15), which yields the nonlinear algebraic system

$$\mathrm{Re}(\sigma_\pm(i\lambda_I)) = 0\,, \qquad \mathrm{Im}(\sigma_\pm(i\lambda_I)) = 0\,, \tag{4.20}$$

or equivalently $\mathcal{H}_c(i\lambda_I) = 0$ from (4.16).

4.2 Example: Two cells on a ring with a center cell

We now apply the theory developed in §4.1 to a population of $m = 3$ cells, where two of the cells are equally spaced on a concentric ring of radius r_0 within the unit disk, with the remaining one centered at the origin (see Fig. 3). For this configuration, the eigenvalues of the 3×3 GCEP matrix $\mathcal{M}(\lambda)$ are given in (4.11) and (4.15) for a single anti-phase mode and the two in-phase modes, respectively. To compute the HB boundaries in the τ versus D parameter plane for these modes, we solve (4.19) and (4.20) numerically by implementing the psuedo-arclength continuation algorithm TEST_CON (cf. [1]) with respect to D, while using Newton's method to compute τ and λ_I at each point on the solution path. Such a continuation scheme in D is needed owing to the possibility of fold points along the HB boundary.

To determine regions of instability in open sets of the τ versus D parameter plane we use (4.18) of Proposition 3, together with the winding number criterion of complex analysis, to identify the number $\mathcal{N}$ of eigenvalues $\lambda \in \Lambda(\mathcal{M})$ with $\mathrm{Re}(\lambda) > 0$. To do so, we first define $\mathcal{F}(\lambda) \equiv \det(\mathcal{M}(\lambda))$, where $\mathcal{M}(\lambda)$ is the GCEP matrix in (4.6). Provided that there are no zeroes or poles on the imaginary axis, $\mathcal{N}$ is the number of zeroes of $\mathcal{F}(\lambda) = 0$ in $\mathrm{Re}(\lambda) > 0$, which from the argument principle is

$$\mathcal{N} = \frac{1}{2\pi}\big[\arg \mathcal{F}(\lambda)\big]_\Gamma + \mathcal{P}\,. \tag{4.21}$$

Here $\mathcal{P}$ is the number of poles of $\mathcal{F}(\lambda)$ in $\mathrm{Re}(\lambda) > 0$, while $\big[\arg \mathcal{F}(\lambda)\big]_\Gamma$ denotes the change in the argument of $\mathcal{F}(\lambda)$ over the closed, counter-clockwise oriented contour Γ. This contour Γ is the limit as $\mathcal{R} \to \infty$ of the union of the imaginary axis $\Gamma_I = i\lambda_I$, for $|\lambda_I| \le \mathcal{R}$, and the semi-circle $\Gamma_\mathcal{R}$, defined by $|\lambda| = \mathcal{R}$ with $|\arg(\lambda)| \le \pi/2$. To count the number of poles of $\mathcal{F}(\lambda)$ in $\mathrm{Re}(\lambda) > 0$, we must examine the analyticity properties of the GCEP matrix $\mathcal{M}(\lambda)$ in (4.6). Since the entries of the Green's matrix $\mathcal{G}_\lambda$ are analytic in $\mathrm{Re}(\lambda) > 0$, any singularity of $\mathcal{F}(\lambda)$ must arise from the diagonal matrix $\mathcal{K}(\lambda) \equiv \mathrm{diag}(K_c, K_c, K_m)$ of (4.6b), which is given explicitly in (4.7) in terms of the Jacobians J_1 and J_m of the Sel'kov kinetics for the identical ring cells and the center cell, respectively. Since $\det(J_1) > 0$, (4.7a) yields that K_c has a complex conjugate pair of poles in $\mathrm{Re}(\lambda) > 0$ only if $\mathrm{tr}(J_1) > 0$. Since this term involves two rows of $\mathcal{M}(\lambda)$, $\mathcal{P}$ must be incremented by four whenever $\mathrm{tr}(J_1) > 0$. Similarly, since $\det(J_m) > 0$, $\mathcal{P}$ is increased by two when $\mathrm{tr}(J_m) > 0$ for the center cell.

With $\mathcal{P}$ determined in this way, we numerically compute the number of unstable eigenvalues $\mathcal{N}$ of the linearization of the steady-state by evaluating (4.21) for each point (D, τ) in the τ versus D plane. For each such point, we numerically construct the closed contour Γ for some value $\mathcal{R}$ (chosen so that Γ encloses all the poles of $\mathcal{F}$) in the complex λ-plane. As the closed curve Γ is traversed in a counter-clockwise direction, the closed image curve $\mathcal{F}(\lambda) = \mathcal{F}_R + i\mathcal{F}_I$ is evaluated numerically in the complex $\mathcal{F}$-plane. The winding number, denoting the number of times $\mathcal{F}$ encloses/winds around the origin, is computed numerically from the algorithm of [2], and this is used to calculate $\big[\arg \mathcal{F}(\lambda)\big]_\Gamma$. If the orientation of $\mathcal{F}(\lambda) = \mathcal{F}_R + i\mathcal{F}_I$ around the origin is in the counter-clockwise direction, then $\big[\arg \mathcal{F}(\lambda)\big]_\Gamma$ is positive; otherwise, it is negative. In our computations, we chose $\mathcal{R} = 1.5$ (since any pole of $\mathcal{F}$ is close to the imaginary axis of the λ-plane), and we discretized the closed contour $\Gamma = \Gamma_I \cup \Gamma_\mathcal{R}$ into subintervals, with Γ_I having 800 subintervals while the semi-circle $\Gamma_\mathcal{R}$ had 50 subintervals. In the function evaluation, the identity $\mathcal{F}(\overline{\lambda}) = \overline{\mathcal{F}(\lambda)}$ was used to halve the computational effort.

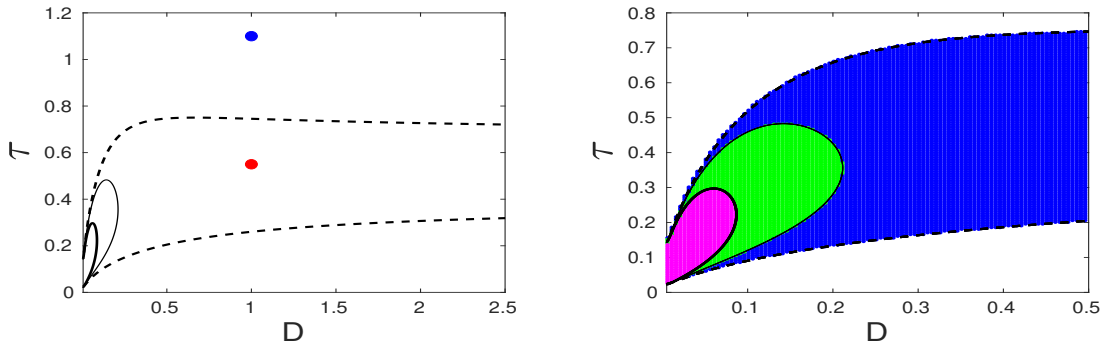

(a) HB boundaries: Identical cells *(b) Number of unstable eigenvalues of the GCEP*

Figure 4: Left panel: HB boundaries in the τ versus D plane for a ring and center hole pattern of $m = 3$ identical cells with ring radius $r_0 = 0.5$, parameters as in (4.22) and permeabilities $d_1 = 0.8$ and $d_2 = 0.2$. The dashed and heavy solid curves are for the in-phase modes computed from (4.20) with $(+)$ and $(-)$, respectively. The thin solid curve is for the anti-phase mode computed from (4.19). Each mode is linearly unstable within its respective lobe. Linearly stable steady-state solutions exist outside the union of the lobes. Full PDE simulations of (1.2) are shown in Figs. 6 and 7 at the red and blue dots, respectively. Right panel: The regions of instability computed from the winding number (4.21). Blue region: in-phase '+' mode is unstable with 2 roots of $\mathcal{F}(\lambda) = \det(\mathcal{M}(\lambda)) = 0$ in $Re(\lambda) > 0$. Green region: anti-phase mode is also unstable, yielding 4 roots. Magenta region: all modes are unstable, and there are 6 roots. Plot on right is a zoom of the one on the left. The HB boundaries in the left panel are superimposed in this figure.

4.3 A defective center cell: different permeabilities

In our results below, except when otherwise stated, the Sel'kov parameters α, μ and ζ, and permeabilities d_1 and d_2 for the identical cells on the ring, and the common cell radius ε are

$$\alpha = 0.9\,, \qquad \mu = 2\,, \qquad \zeta = 0.15\,, \qquad d_1 = 0.8\,, \qquad d_2 = 0.2\,, \qquad \varepsilon = 0.05\,. \tag{4.22}$$

From Fig. 2, we conclude that each cell, when isolated, has no intracellular oscillations. The permeabilities d_{13} and d_{23} for the center cell will be stated in the figure captions below.

Fig. 4a shows the computed HB boundaries in the τ versus D plane for a ring of radius $r_0 = 0.5$ when the cells are all identical. We observe that one of the in-phase lobes is open/unbounded, which predicts the existence of intracellular

oscillations even for large D. In Fig. 4b, we show the corresponding regions of instability in the τ versus D parameter plane. In generating this figure, we pixelated the τ versus D plane with the uniform spacing $\Delta\tau = \Delta D = 0.005$, and at each discrete point (D, τ) used our winding number algorithm to count the number of roots $\mathcal{N}$ of $\det\mathcal{M}(\lambda) = 0$ in $\mathrm{Re}(\lambda) > 0$. In Fig. 4b, each point in the blue-shaded region has two unstable eigenvalues for the GCEP, and they correspond to the in-phase '+' mode. The green-shaded region contains four unstable eigenvalues, two of which are for the anti-phase mode while the other two for the in-phase '+' mode. Finally, in the magenta-shaded region there are six unstable eigenvalues of the linearization, with two such eigenvalues associated with each of the three possible modes of instability (in-phase $\pm$ and anti-phase). The HB boundaries in the left panel of Fig. 4 are superimposed on these instability regions.

The $\mathcal{F}(\lambda) = \mathcal{F}_R + i\mathcal{F}_I$ curve in the complex $\mathcal{F}$-plane is shown in Fig. 5 for a specific point in each of the three instability regions in Fig. 4b. These plots show how $\mathcal{F}(\lambda)$ winds around the origin $(\mathcal{F}_R, \mathcal{F}_I) = (0, 0)$ (shown with a green dot) as λ traverses Γ in the counterclockwise direction. For the point $(D, \tau) = (0.05, 0.15)$ in the magenta-shaded region, we observe from the left panel of Fig. 5 that $\left[\arg\mathcal{F}(\lambda)\right]_\Gamma = 0$. At this point, $\mathcal{F}(\lambda)$ has two poles, one of order four and the other of order 2, so that $\mathcal{P} = 6$. As such, (4.21) yields that there are 6 roots (counting multiplicity) to $\mathcal{F}(\lambda) = 0$ in $\mathrm{Re}(\lambda) > 0$. At the point $(D, \tau) = (0.15, 0.35)$ in the anti-phase mode instability region (green-shaded region in Fig. 4b), $\mathcal{F}(\lambda)$ winds round the origin twice in the clockwise direction as shown in the middle panel of Fig. 5, which yields $\left[\arg\mathcal{F}(\lambda)\right]_\Gamma = -4\pi$. Since $\mathcal{P} = 6$ at this point, (4.21) yields that $\mathcal{F}(\lambda) = 0$ has four roots (counting multiplicity) in $\mathrm{Re}(\lambda) > 0$. In the right panel of Fig. 5, we present a similar result for the point $(D, \tau) = (0.4, 0.5)$ in the blue-shaded region in Fig. 4b. At this point, we calculate $\left[\arg\mathcal{F}(\lambda)\right]_\Gamma = -8\pi$ and that $\mathcal{F}$ has a pole of order four and a pole of order two in $\mathrm{Re}(\lambda) > 0$. As such, (4.21) yields that $\mathcal{F}(\lambda) = 0$ has two roots in $\mathrm{Re}(\lambda) > 0$.

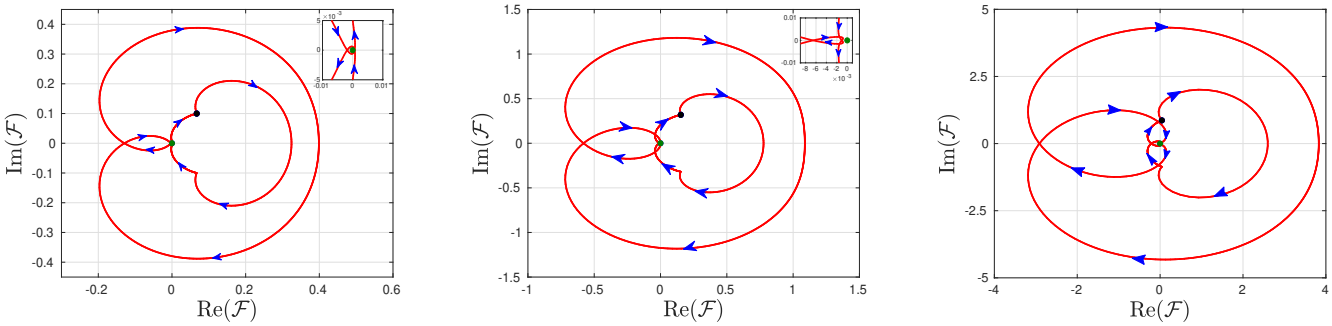

Figure 5: The closed curve $\mathcal{F}(\lambda) = \det(\mathcal{M}(\lambda))$ plotted for a specific points in each of the three regions of instability in Fig. 4b. The closed contour $\Gamma = \Gamma_I \cup \Gamma_\mathcal{R}$ in the λ-plane was constructed with $\mathcal{R} = 1.5$, and discretized with 800 subintervals on Γ_I and 50 subintervals on $\Gamma_\mathcal{R}$. The green dot represents the origin $(\mathcal{F}_R, \mathcal{F}_I) = (0, 0)$, the black dot indicates the starting point of the curve, and the blue arrows show the direction of the curve. The inserts detail the behavior near the origin. Left panel: for $(D, \tau) = (0.05, 0.15)$ in the magenta-shaded region of Fig. 4b, we have $\left[\arg\mathcal{F}(\lambda)\right]_\Gamma = 0$. Middle panel: for $(D, \tau) = (0.15, 0.35)$ in the green-shaded region in Fig. 4b, we have $\left[\arg\mathcal{F}(\lambda)\right]_\Gamma = -4\pi$. Right panel: for $(D, \tau) = (0.4, 0.5)$ in the blue-shaded region of Fig. 4b, we have $\left[\arg\mathcal{F}(\lambda)\right]_\Gamma = -8\pi$.

The real and imaginary parts of the normalized eigenvector $\boldsymbol{c}$ of the GCEP matrix $\mathcal{M}$ in (4.6) is given in Table 1 for selected points on the HB boundaries in Fig. 4a. Recall from (2.24) that the magnitude of the components of the eigenvector $\boldsymbol{c}$ measure the diffusive flux at the boundary of each cell, while $\tilde{\boldsymbol{c}} \equiv \mathcal{K}\boldsymbol{c}$ predicts the relative amplitude and phase shifts of the intracellular oscillations within the cells at the Hopf bifurcation point. For our ring and center-cell pattern $\mathcal{K} = \mathrm{diag}\,(K_c, K_c, K_m)$, where K_c and K_m are given in (4.7a).

mode	(D, τ)	j	$\left(\mathrm{Re}(c_j), \mathrm{Im}(c_j)\right)$	θ_j (rad)	$\left(\mathrm{Re}(\tilde{c}_j), \mathrm{Im}(\tilde{c}_j)\right)$
In-phase (+) (dashed curve)	$(1.021, 0.262)$	1	$(0.579, 0)$	0	$(-0.569, 0.067)$
		2	$(0.579, 0)$	0	$(-0.569, 0.067)$
		3	$(0.575, 0.0144)$	0.0251	$(-0.582, 0.0625)$
In-phase (−) (heavy solid)	$(0.0857, 0.199)$	1	$(-0.412, -0.004)$	3.15	$(0.395, -0.00429)$
		2	$(-0.412, -0.004)$	3.15	$(0.395, -0.00429)$
		3	$(0.813, 0)$	0	$(-0.829, 0.0239)$
Anti-phase (thin solid)	$(0.211, 0.365)$	1	$(0.707, 0)$	0	$(-0.706, 0.042)$
		2	$(-0.707, 0)$	π	$(0.706, -0.042)$
		3	$(0, 0)$	0	$(0, 0)$

Table 1: Real and imaginary parts of the eigenvector $\boldsymbol{c}$ of the GCEP matrix $\mathcal{M}(\lambda)$ in (4.6), together with $\tilde{\boldsymbol{c}} \equiv \mathcal{K}\boldsymbol{c}$, as computed for a few points on the HB boundaries in Fig. 4a for three identical cells. The second to last column shows the phase shifts measured in terms of the angle each component of the vector $\boldsymbol{c}$ makes with the positive real axis in anticlockwise direction.

In Fig. 6 we show full numerical simulations of the coupled PDE-ODE model (1.2) obtained using the commercial PDE

software package FlexPDE [14] for $\tau = 0.55$ and $D = 1$, which corresponds to the red dot in the phase diagram of Fig. 4a. We observe from the results in this figure that the intracellular dynamics of the cells are synchronized with a very slight phase shift, which agrees with the prediction by the eigenvector $\mathcal{K}\boldsymbol{c}$ in the first three rows of Table 1 from the linearized theory. Although the cells have identical parameters, the center and ring cells have slightly different dynamics owing to the fact that the full Green's matrix is not cyclic for a ring and center cell pattern. Our numerical computations of $\det \mathcal{M}(\lambda) = 0$ for $(D, \tau) = (1, 0.55)$ using the GCEP matrix in (4.6) yields that $\mathrm{Re}(\lambda) \approx 0.0143$, $\mathrm{Im}(\lambda) \approx 0.762$, $\mathrm{Re}(\boldsymbol{c}) \approx (0.588, 0.588, 0.556)$ and $\mathrm{Im}(\boldsymbol{c}) \approx (0, 0, 0.0178)$. Observe that the eigenvector is rather close to that on the nearby point on the HB boundary, as given in the first three rows of Table 1. The prediction from linearized theory is that the period of oscillations is approximately $2\pi/\mathrm{Im}(\lambda) \approx 8.25$, which is rather close to the period observed in the full PDE simulations of Fig. 6. A similar full numerical result is presented in Fig. 7 for $\tau = 1.1$ and $D = 1$, corresponding to the blue dot in Fig. 4a. At this pair (D, τ), our phase diagram predicts no intracellular oscillations. This is confirmed from the full numerical results shown in Fig. 7.

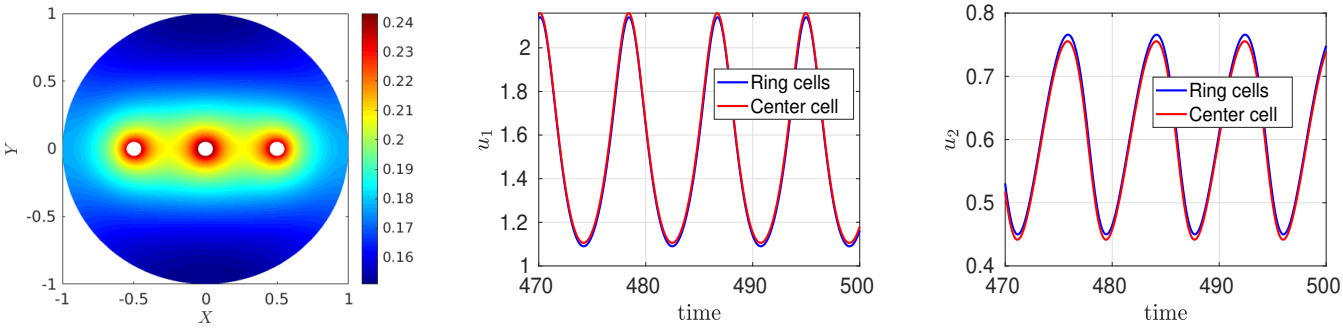

Figure 6: Full PDE simulations of (1.2), computed with FlexPDE [14], for $\tau = 0.55$ and $D = 1$ for three identical cells corresponding to the red dot in Fig. 4a. Left panel: surface plot at time $t = 400$. Middle panel: intracellular species u_1 versus t. Right panel: intracellular species u_2 versus t. The blue and red curve is for the cells on the ring and the center cell, respectively.

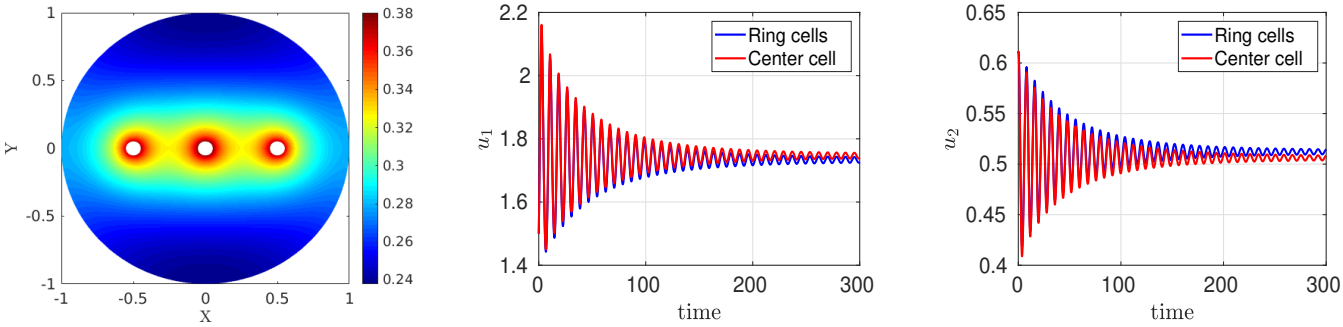

Figure 7: Same caption as in Fig. 6 except that now $\tau = 1.1$ and $D = 1$, corresponding to the blue dot in Fig. 4a. There are no intracellular oscillations and the steady-state is linearly stable.

In the left panel of Fig. 8 we show the computed HB boundaries in the τ versus D plane for the same parameters as in Fig. 4a, except that the influx rate into the center cell is reduced to $d_{13} = 0.4$ (keeping $d_{23} = 0.2$). With this lower influx rate, Fig. 8 shows that the in-phase lobes are now closed, so that there are no longer intracellular oscillations when D is large. Qualitatively, when D is large, the bulk chemical diffuses quickly in the entire disk and there is insufficient feedback of it into the center cell, owing to the smaller value of d_{13}, to sustain intracellular oscillations. The winding number algorithm of (4.21) can be used, with the same result as in Fig. 4, to determine the number of unstable eigenvalues of the GCEP within the lobes (not shown). In the right panel of Fig. 8 we give the real and imaginary parts of the normalized eigenvector $\boldsymbol{c}$ of the GCEP matrix in (4.6) at a few selected points on the HB boundaries shown in the left panel of Fig. 8.

In Fig. 9, we show full FlexPDE [14] numerical simulations of (1.2) for $\tau = 0.6$ and $D = 0.4$, which corresponds to the red dot in the left panel of Fig. 8. Our numerical computations of $\det \mathcal{M}(\lambda) = 0$ for $(D, \tau) = (0.4, 0.6)$ using the GCEP matrix in (4.6) yields that $\mathrm{Re}(\lambda) \approx 0.0115$, $\mathrm{Im}(\lambda) \approx 0.778$, $\mathrm{Re}(\mathcal{K}\boldsymbol{c}) \approx (-0.551, -0.551, -0.624)$ and $\mathrm{Im}(\mathcal{K}\boldsymbol{c}) \approx (0.0197, 0.0197, 0.0569)$. As such, our linearized theory predicts that the center cell will have larger amplitude oscillations near onset than the ring cells, and there will be a $\approx 22°$ phase shift between the oscillations. Our FlexPDE numerical results in the middle and right panels of Fig. 9 show that the prediction of the linearized theory does extend to the fully nonlinear regime in that the defective center cell has larger amplitude oscillations than do the identical ring cells, and there is a slight phase shift in the oscillations. From the surface plot shown in the left panel of Fig. 9, we observe that the coupling between the cells mediated by the bulk medium is rather weak. Moreover, the rather large concentration of the bulk chemical close to the center cell, with flux measured by the modulus of the third component of $\mathrm{Re}(\boldsymbol{c}) \approx (0.267, 0.267, 0.914)$ and $\mathrm{Im}(\boldsymbol{c}) \approx (0.107, 0.107, 0.0)$, is due to its smaller rate $d_{13} = 0.4$ of influx into the center cell than for the identical ring cells centered at $(\pm 0.5, 0)$. Paradoxically,

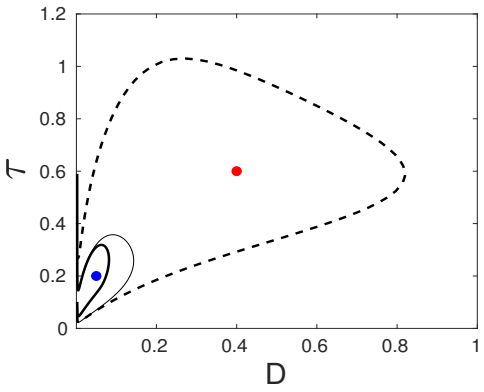

mode	(D, τ)	j	Re(c_j)	Im(c_j)	θ_j (rad)
In-phase (+) (dashed curve)	$(0.820, 0.584)$	1	0.345	0.171	0.460
		2	0.345	0.171	0.460
		3	0.839	0	0
In-phase (−) (heavy solid)	$(0.0775, 0.216)$	1	−0.446	0.256	2.62
		2	−0.446	0.256	2.62
		3	0.686	0	0
Anti-phase (thin solid)	$(0.129, 0.325)$	1	0.707	0	0
		2	−0.707	0	π
		3	0	0	0

Figure 8: Left panel: same caption as in Fig. 4a except that now the center cell is a defector with permeabilities $d_{13} = 0.4$ and $d_{23} = 0.2$, corresponding to a reduced influx into the center cell. Full PDE simulations are shown in Figs. 9 and 10 at the red and blue dots, respectively. Right panel: same caption as in Table 1 except that now $d_{13} = 0.4$ and $d_{23} = 0.2$. The real and imaginary parts of the eigenvector $\mathbf{c}$ of the GCEP matrix $\mathcal{M}(\lambda)$ in (4.6) are computed for a few points on the HB boundaries shown in the left panel.

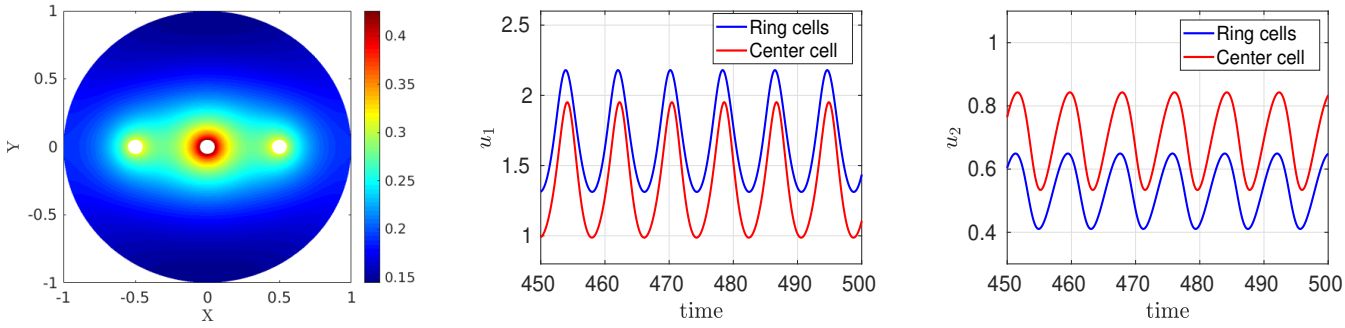

Figure 9: Full PDE simulations of (1.2), computed with FlexPDE [14], for $\tau = 0.6$ and $D = 0.4$, corresponding to the red dot in the left panel of Fig. 8. The center cell is a defector with permeabilites $d_{13} = 0.4$ and $d_{23} = 0.2$. Left panel: surface plot at time $t = 400$. Middle panel: intracellular species u_1 versus t. Right panel: intracellular species u_2 versus t.

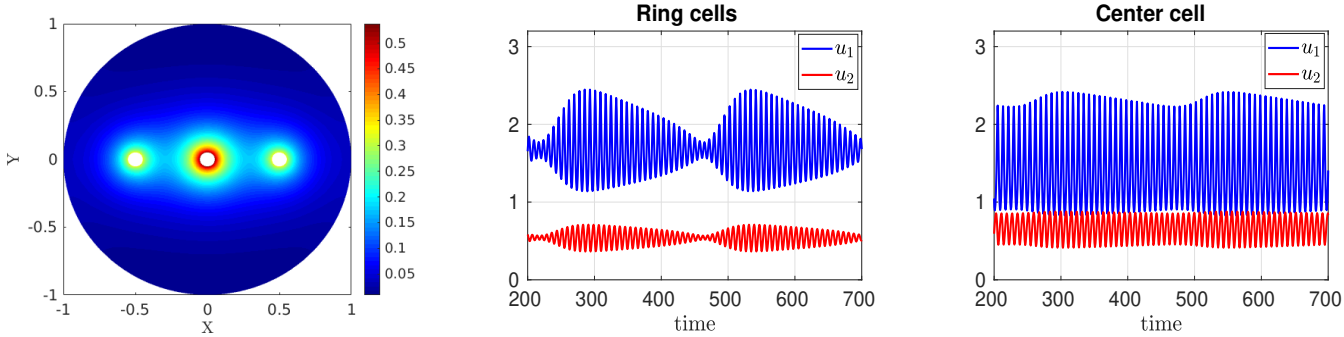

Figure 10: Same caption as in Fig. 9, except that the FlexPDE [14] simulation of (1.2) is done at $\tau = 0.2$ and $D = 0.05$, corresponding to the blue dot in the left panel of Fig. 8. At this point, both in-phase modes and the anti-phase mode are unstable. The beating-behavior observed arises from the fact that these three modes all have comparable frequencies.

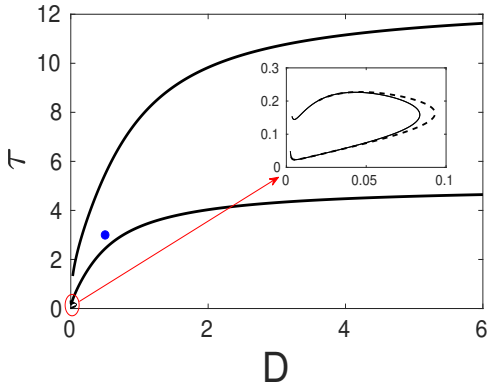

mode	(D,τ)	j	Re(c_j)	Im(c_j)	θ_j (rad)
In-phase (+) (dashed curve)	$(0.0931, 0.165)$	1	0.707	0	0
		2	0.707	0	0
		3	0.0245	-0.0314	5.375
In-phase (−) (heavy solid)	$(1.241, 3.577)$	1	-0.0638	0.0985	2.146
		2	-0.0638	0.0985	2.146
		3	0.986	0	0
Anti-phase (thin solid)	$(0.0836, 0.159)$	1	0.707	0	0
		2	-0.707	0	π
		3	0	0	0

Figure 11: Same caption as in Fig. 8 except that now the center cell is a defector with permeabilities $d_{13} = 0.2$ and $d_{23} = 0.4$, corresponding to a reduced influx and a larger efflux out of the center cell. Full PDE simulations are shown in Fig. 12 at the blue dot in the left panel.

however, this large buildup of the bulk signal near the center cell counteracts the relatively smaller rate of influx into the center cell, and has the effect of triggering a larger amplitude oscillation in the center cell than for the ring cells.

In Fig. 10, we show full FlexPDE [14] numerical simulations of (1.2) for $\tau = 0.2$ and $D = 0.05$, corresponding to the blue dot in the left panel of Fig. 8. As seen from Fig. 8, this point is located within the region of instability that is common to all three modes of instability. By solving $\det \mathcal{M}(\lambda) = 0$ for $(D, \tau) = (0.05, 0.2)$ numerically, the eigenvalues λ and eigenvectors $\boldsymbol{c}$ for the three modes are:

$$\begin{aligned}
\text{in-phase } (+): &\quad \lambda \approx 0.0350 + 0.779\,i\,, \quad \text{Re}(c) \approx (0.152, 0.152, 0.829)\,, \quad \text{Im}(c) \approx (0, 0, -0.517)\,, \\
\text{in-phase (-)}: &\quad \lambda \approx 0.0144 + 0.813\,i\,, \quad \text{Re}(c) \approx (0.624, 0.624, -0.434)\,, \quad \text{Im}(c) \approx (0, 0, -0.180)\,, \\
\text{anti-phase}: &\quad \lambda \approx 0.0189 + 0.812\,i\,, \quad \text{Re}(c) \approx (0.707, -0.707, 0)\,, \quad \text{Im}(c) = (0, 0, 0)\,.
\end{aligned} \tag{4.23}$$

We observe that this linearized theory predicts three distinct unstable oscillatory modes with roughly similar frequencies Im(λ) and growth rates Re(λ). The beating-type intracellular oscillations observed in Fig. 10 is likely related to the well-known linear phenomenon of superimposing two or more single-mode oscillations with comparable frequencies.

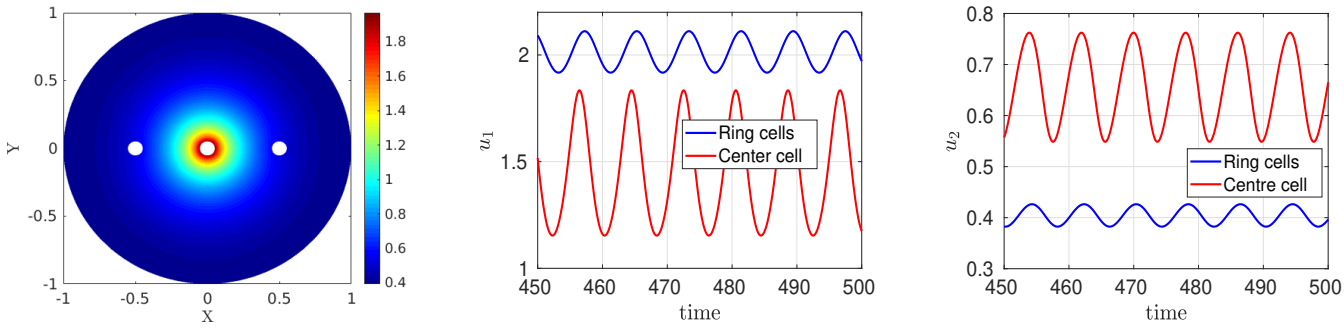

Figure 12: Full PDE simulations of (1.2), computed with FlexPDE [14], for $\tau = 3$ and $D = 0.5$, corresponding to the blue dot in the left panel of Fig. 11. The center cell is a defector with permeabilites $d_{13} = 0.2$ and $d_{23} = 0.4$. Left panel: surface plot at time $t = 400$. Observe the buildup of the bulk chemical near the center cell in comparison to the two ring cells. Middle panel: intracellular species u_1 versus t. Right panel: intracellular species u_2 versus t. As predicted by the second row in the table in the right panel of Fig. 11, we confirm that the center cell has larger amplitude oscillations than do the ring cells.

In the left panel of Fig. 11 we plot the HB boundaries for the case where the center cell has permeabilities $d_{13} = 0.2$ and $d_{23} = 0.4$. This corresponds to a larger secretion or efflux rate for the center cell, while the feedback it receives from the ring cells is reduced. Unlike the HB boundaries shown in Figs. 4 and 8 where the instability regions for the modes are nested within each other, we observe from the insert in the left panel of Fig. 11 that only the in-phase (+) mode and the anti-phase mode overlap. Moreover, since the other in-phase (−) lobe is unbounded in D, intracellular oscillations always occur in some range of τ as D increases. In the right panel of Fig. 11, we give the real and imaginary parts of the normalized eigenvector $\boldsymbol{c}$ of the GCEP matrix (4.6) at a few points on the HB boundaries. From the second row of this table, the linearized theory suggests that the amplitude of intracellular oscillations associated with the dominant in-phase (−) instability lobe will be much larger in the center cell than in the identical ring cells at the HB point, and that there will be a significant phase shift in the oscillations between the center cell and the ring cells. More precisely, at the point $(D, \tau) = (0.5, 3)$ interior to the instability lobe, we solve $\det \mathcal{M}(\lambda) = 0$ numerically to obtain that Re$(\lambda) \approx 0.00665$, Im$(\lambda) \approx 0.781$, Re$(\boldsymbol{c}) \approx (-0.0534, -0.0534, 0.9908)$,

$\mathrm{Im}(\boldsymbol{c}) \approx (0.0792, 0.0792, 0)$, $\mathrm{Re}(\mathcal{K}\boldsymbol{c}) \approx (-0.177, -0.177, -0.926)$, and $\mathrm{Im}(\mathcal{K}\boldsymbol{c}) \approx (0.187, 0.187, 0.106)$. From $\mathcal{K}\boldsymbol{c}$ and $\mathrm{Im}(\lambda)$ this indicates that the center cell will have much larger oscillations near onset than the ring cells, with a period of oscillations of ≈ 8 and with a phase shift of $\approx 40^\circ$ between the ring and center cell oscillations. From the FlexPDE simulations of (1.2) when $\tau = 3$ and $D = 0.5$ shown in Fig. 12, corresponding to the blue dot in the left panel of Fig. 11, we observe that these predictions of the linearized theory are roughly satisfied. Moreover, since the efflux rate out of the center cell is larger, while the influx rate is smaller, the rather small bulk diffusivity $D = 0.5$ should qualitatively lead to a buildup of the bulk chemical near the center cell at certain times in the oscillation. This feature is observed in the surface plot in the left panel of Fig. 12, and provides a clear example of diffusion-mediated behavior, as regulated by the permeability parameters.

Next, we examine whether the ODE system (3.16) of Proposition 2, derived under the assumption of large bulk diffusivity $D = \mathcal{O}(\nu^{-1}) \gg 1$, can still be used to reliably approximate the intracellular dynamics observed in the full FlexPDE simulation results of (1.2), performed for $\mathcal{O}(1)$ values of D, in Figs. 6, 7, 9 and 12. In Fig. 13 we show that the numerical results computed from the ODE system (3.16) compare surprisingly well with the full PDE simulations with respect to the amplitude and period of intracellular oscillations (first, third and fourth rows of Fig. 13) and the prediction of a linearly stable steady-state (second row of Fig. 13). In using the ODE system (3.16) we calculated D_0 as $D_0 = D\nu$, where $\nu = -1/\log\varepsilon$ with $\varepsilon = 0.05$. We remark that the beating-type oscillations observed in Fig. 10 for the very small value $D = 0.05$ are not captured by the ODE system (3.16). Moreover, we emphasize that the simpler ODE system corresponding to the well-mixed limit $D \to \infty$ as given in (3.19), and which was used in [20] and [26] for studying quorum-sensing behavior, does not reliably approximate the intracellular oscillations for the values of bulk diffusivity given in Figs. 6, 7, 9, 9, and 12.

4.4 A defective center cell: different Sel'kov kinetics

Next, we study how the HB boundaries in the (D, τ) plane are altered by varying a Sel'kov kinetic parameter of the center cell. In Fig. 14 we plot the HB boundaries for a ring and center cell pattern of $m = 3$ cells, where the identical cells on the ring have parameters as in (4.22), while the Sel'kov parameter α_3 for the defective center cell is either $\alpha_3 = 0.86$ (red curves), $\alpha_3 = 0.96$ (blue curves), or $\alpha_3 = 0.9$ (same as in the left panel of Fig. 4). The HB boundaries in the right panel of Fig. 14 show a zoom for smaller values of D than the figure in the left panel. In these figures, the dashed and the heavy solid curves are for the in-phase modes computed from (4.20) with $(+)$ and $(-)$, respectively, while the thin solid curve is for the anti-phase mode computed from (4.19). We observe that the HB boundary for the anti-phase mode is independent of the Sel'kov kinetic parameter α_3 for the center cell. This follows from the facts that the steady-state solution to (4.4) for the ring cells and its Jacobian J_1 in (4.7b) do not depend on α_3. As a result, the anti-phase HB boundary, computed from (4.19), is independent of α_3.

From the left panel of Fig. 14 we observe that as α_3 increases the parameter regions in the (D, τ) plane where intracellular oscillations occur decreases. In particular, the in-phase $(+)$ instability lobe that was open for $\alpha_3 = 0.86$ becomes closed when $\alpha_3 = 0.96$, thereby precluding the possibility of intracellular oscillations when D is sufficiently large. To interpret this result, we observe from the middle panel of Fig. 2 that, as α_3 increases, the center cell becomes less activated, with the parameters drifting further from the HB boundary for the uncoupled cell. As a result, it becomes more difficult to trigger in-phase intracellular oscillations for a group of coupled cells as α_3 increases. Overall, Fig. 14 does show that rather small increases or decreases in a parameter value of the nonlinear Sel'kov kinetics for one specific cell can either extinguish or trigger intracellular oscillations for an entire group of cells. The corresponding eigenvectors for selected points on the bifurcation diagrams in Fig. 14 are shown in Table 2 for $\alpha_3 = 0.86$ and $\alpha_3 = 0.96$.

mode	j	$\alpha_3 = 0.86$			$\alpha_3 = 0.96$		
		(D, τ)	$(\mathrm{Re}c_j, \mathrm{Im}c_j)$	θ_j (rad)	(D, τ)	$(\mathrm{Re}c_j, \mathrm{Im}c_j)$	θ_j (rad)
In-phase $(+)$ (heavy solid)	1	$(0.233, 0.744)$	$(0.539, -0.080)$	6.14	$(0.475, 0.672)$	$(0.639, 0)$	0
	2		$(0.539, -0.080)$	6.14		$(0.639, 0)$	0
	3		$(0.638, 0)$	0		$(0.427, -0.0118)$	6.256
In-phase $(-)$ (dashed curve)	1	$(0.108, 0.284)$	$-(0.461, 0.0415)$	3.23	$(0.0492, 0.168)$	$(-0.254, 0.0428)$	2.974
	2		$-(0.461, 0.0415)$	3.23		$(-0.254, 0.0428)$	2.974
	3		$(0.756, 0)$	0		$(0.932, 0)$	0
Anti-phase (thin solid)	1	$(0.211, 0.365)$	$(0.707, 0)$	0	$(0.211, 0.365)$	$(0.707, 0)$	0
	2		$-(0.707, 0)$	π		$-(.707, 0)$	π
	3		$(0, 0)$	0		$(0, 0)$	0

Table 2: Real and imaginary parts of the eigenvector $\boldsymbol{c}$ of the GCEP matrix $\mathcal{M}(\lambda)$ in (4.6), computed for a few points on the HB boundaries in Fig. 14. The cells on the ring are identical and located at $(\pm 0.5, 0)$ with parameters as given in (4.22). The center cell has the same parameters, with the exception that it has a Sel'kov kinetic parameter α_3 different than those on the ring. Middle three columns: $\alpha_3 = 0.86$. Last three columns: $\alpha_3 = 0.96$.

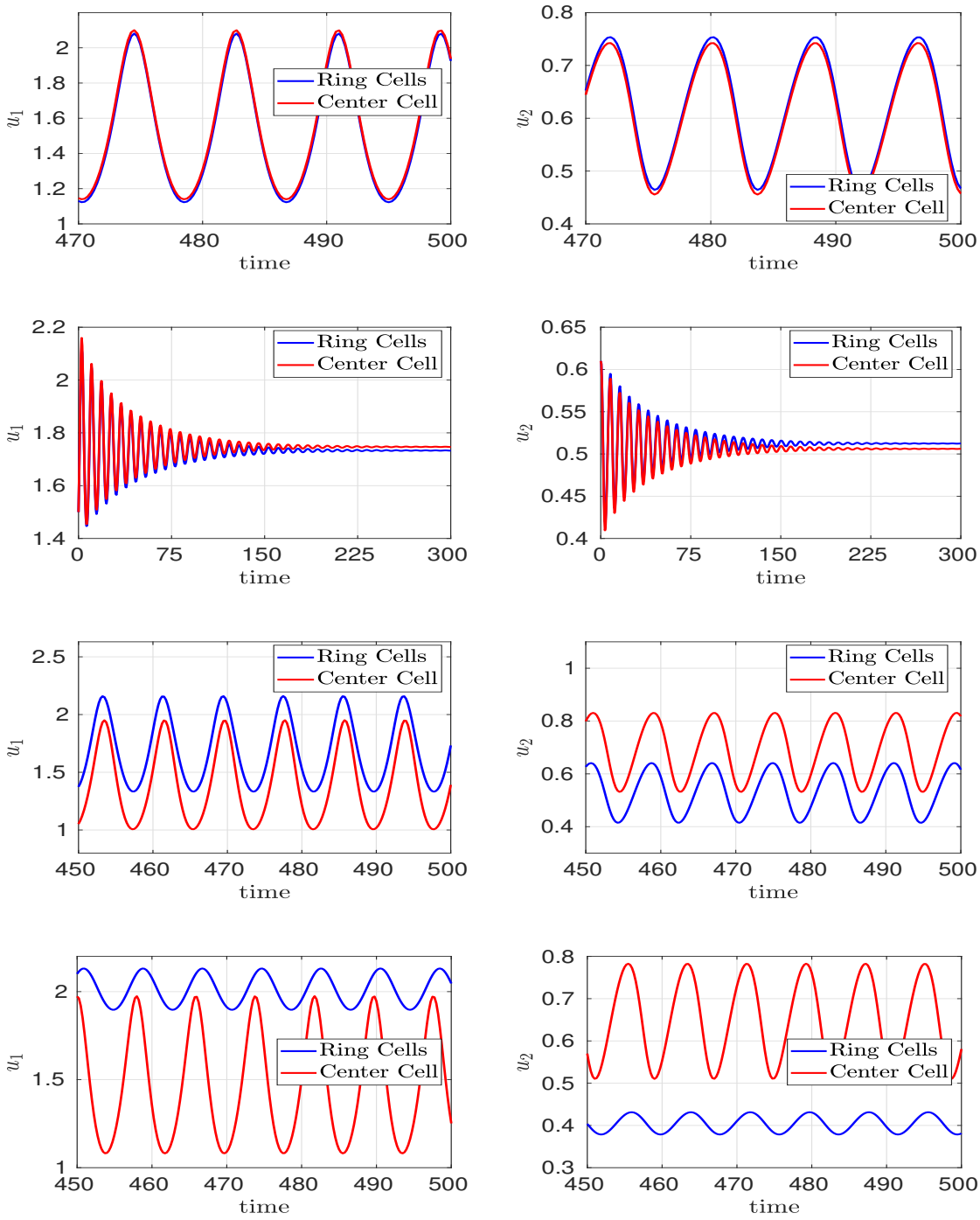

Figure 13: Numerical results for intracellular dynamics versus time computed from the ODE system (3.16) of Proposition 2 corresponding to the PDE simulations shown in Fig. 6 (first row), Fig. 7, (second row), Fig. 9 (third row) and Fig. 12 (fourth row), respectively. In each case, although D is not large, results from the ODE system (3.16) are seen to compare surprisingly well with the full FlexPDE simulations of the PDE-ODE system (1.2). First row: $(D, \tau) = (1.0, 0.55)$ (red dot in Fig. 4a). Compare with Fig. 6. Second row: $(D, \tau) = (1.0, 1.1)$ (blue dot in Fig. 4a). Compare with Fig. 7. Third row: $(D, \tau) = (0.4, 0.6)$ (red dot in the left panel of Fig. 8). Compare with Fig. 9. Fourth row: $(D, \tau) = (0.5, 3)$ (blue dot in the left panel of Fig. 11). Compare with Fig. 12. Although there is a phase shift between the ODE and full PDE results for intracellular oscillations due to different initial conditions used, the ODE system (3.16) captures well the amplitude and period of intracellular oscillations observed in the full PDE simulations.

4.5 The effect of cell locations on triggering oscillations

For a ring and center cell pattern, with cells centered at $(\pm r_0, 0)$ and $(0, 0)$, we study how the HB boundaries in the (D, τ) plane depend on the ring radius r_0. In the first row of Fig. 15 we show the HB boundaries for the in-phase and anti-phase modes when $r_0 = 0.25$, $r_0 = 0.5$ (same as Fig. 4a), and $r_0 = 0.75$ for the case where the cells are all identical with permeabilities $d_1 = 0.8$ and $d_2 = 0.4$. Similar plots for the three values of r_0 are shown in the second row of Fig. 15 for the

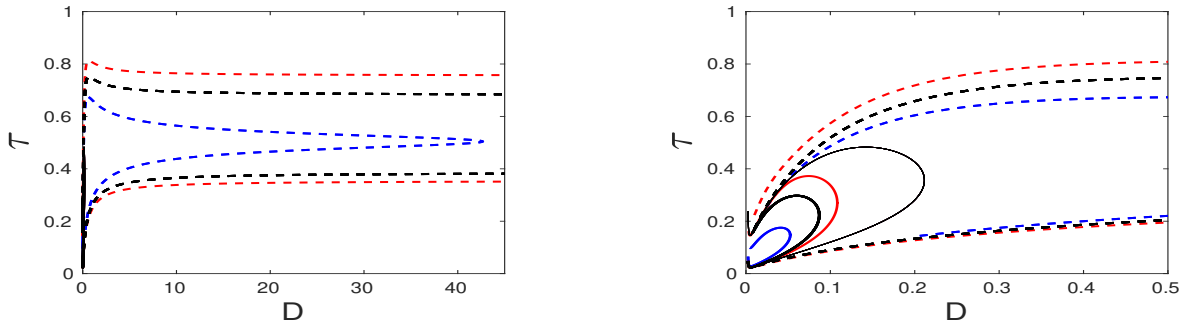

Figure 14: HB boundaries in the τ versus D plane for a ring and center cell pattern of $m = 3$ cells, where the Sel'kov kinetic parameter α_3 for the center cell is varied. The ring cells are centered at $(\pm 5, 0)$ and, with the exception of the Sel'kov kinetic parameter for the center cell, all three cells have parameters as in (4.22). Left panel: $\alpha_3 = 0.86$ (red curves), $\alpha_3 = 0.9$ (black curves), $\alpha_3 = 0.96$ (blue curves). Right panel: a zoomed-in version of the left panel for smaller values of D. In both panels, the dashed and heavy solid curves are for the in-phase modes computed from (4.20), while the thin solid curve is for the anti-phase mode computed from (4.19). Each mode is linearly unstable in their respective lobes, while linearly stable steady-state solutions exists outside the union of the lobes. The anti-phase HB boundaries are independent of α_3, and so are plotted on top of each other.

case where the center cell is now defective with $d_{13} = 0.4$ and $d_{23} = 0.2$ (Fig. 15e for $r_0 = 0.5$ is the same as in Fig. 8).

When the cells are all identical, we observe from the top row in Fig. 15 that the regions of instability for the anti-phase mode and the in-phase $(-)$ mode shrink noticeably as r_0 decreases. In contrast, the instability region for the in-phase $(+)$ mode is relatively insensitive to changes in r_0. To qualitatively explain this observation, we examine the eigenvector of the GCEP matrix given in Table 1 at points on the HB boundaries for the three modes. From this table, for the in-phase $(-)$ mode only the two ring cells oscillate in phase while the center cell has larger amplitude oscillations that are roughly 180° out of phase. For the anti-phase $(-)$ mode, the center cell is quiescent while the ring cells oscillate 180° out of phase. Finally, for the dominant in-phase $(+)$ mode, the three identical cells are synchronized with very similar amplitudes and phases. Intuitively, as the ring radius r_0 decreases the cells become more clustered and, as a result, intracellular dynamics can still be synchronized even for smaller values of the bulk diffusivity D. As a result, when r_0 is small, the anti-phase and in-phase $(-)$ instability lobes, in which the center and ring cells are not synchronized, should exist only for very small values of D (see Fig. 15a). When D is very small, communication between cells that are close can still be rather weak. Notice that for $r_0 = 0.75$, where the cells are farther apart, the anti-phase lobe in Fig. 15c exists for larger values of D than when $r_0 = 0.25$ or $r_0 = 0.5$. For $r_0 = 0.75$, the ring cells can oscillate, maintaining a quiescent center cell, provided that the bulk chemical is not washed away, i.e. D is not too large, owing to the fact that each of the two ring cells are now relatively close to their images across the domain boundary due to the reflecting boundary condition imposed. However, when r_0 is large, the ring cells are far from each other and so, within the anti-phase instability lobe, their oscillations are 180° out of phase.

The second row of Fig. 15 shows similar results for the case where the center cell is defective, with permeabilities $d_{13} = 0.4$ and $d_{23} = 0.2$, corresponding to a reduced rate of influx into the center cell. Similar to the results for identical cells presented in the first row of Fig. 15, as r_0 decreases the region of instability for the in-phase $(-)$ and the anti-phase modes shrink. Moreover, we observe that the maximum extent in D of the in-phase $(+)$ lobes, in which all the cells are essentially synchronized in amplitude and phase, decreases as r_0 increases. This is because when the cells are farther apart, a relatively smaller value of the bulk diffusivity can lead to a washing out of the bulk signal, which thereby weakens the communication between the three cells and precludes synchronization.

5 Asymptotic analysis for a large population of cells

As the number of cells increases it becomes increasingly more challenging numerically to determine the stability boundaries in parameter space from the root-finding condition $\det \mathcal{M}(\lambda) = 0$ given an arbitrary cell configuration $\boldsymbol{x}_j$ with arbitrary permeability parameters d_{1j} and d_{2j} for $j = 1, \ldots, m$. In this section we provide a simpler approach to determine the stability boundaries from the GCEP (2.20) for the large bulk diffusion parameter regime where $D = \mathcal{O}(\nu^{-1})$. To isolate only the effect of different cell configurations, such as shown in Fig. 16, as well as the effect of different cell permeabilities, in our analysis below we will assume that the Sel'kov kinetic parameters are all cell-independent, i.e. that $\alpha_j = \alpha$, $\mu_j = \mu$ and $\zeta_j = \zeta$ for $j = 1, \ldots, m$. Our analysis is easily extended to remove this assumption.

We first recall from (2.28b) of §2.2 that, for $\varepsilon \to 0$, the steady-state solution with Sel'kov kinetics is determined in terms of the solution $\boldsymbol{\mathcal{A}} = (A_1, \ldots, A_m)^T$ to the linear system

$$\left(I + 2\pi\nu\mathcal{G} + \nu\, D\, P_1 + \frac{2\pi\nu D}{\tau} P_2 \right) \mathcal{A} = -\mu\nu P_2\, \boldsymbol{e}\,; \qquad P_1 = \operatorname{diag}\Big(\frac{1}{d_{11}}, \ldots, \frac{1}{d_{1m}} \Big) \quad P_2 = \operatorname{diag}\Big(\frac{d_{21}}{d_{11}}, \ldots, \frac{d_{2m}}{d_{1m}} \Big), \tag{5.1a}$$

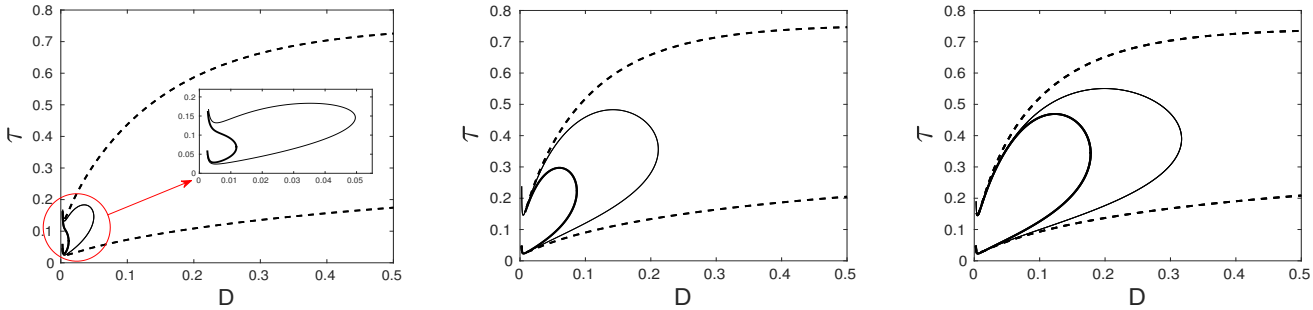

(a) $r_0 = 0.25$ (b) $r_0 = 0.5$ (c) $r_0 = 0.75$

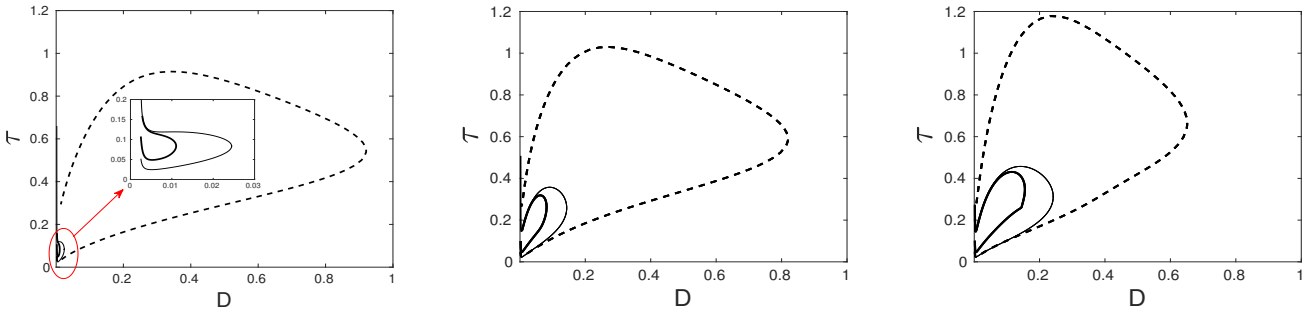

(d) $r_0 = 0.25$ (e) $r_0 = 0.5$ (f) $r_0 = 0.75$

Figure 15: HB boundaries in the τ versus D plane for a ring and center hole configuration of $m = 3$ cells, for three different ring radii r_0 as indicated. The Sel'kov parameters and cell radius are as in (4.22). Top row: identical cells with permeabilities $d_1 = 0.8$ and $d_2 = 0.2$. Bottom row: center cell is defective with $d_{13} = 0.4$ and $d_{23} = 0.2$. The dashed and heavy solid curves are the HB boundaries for the in-phase $(+)$ and $(-)$ modes, respectively, as computed from (4.20). The thin solid curve is the HB boundary for the anti-phase mode computed from (4.19). Each mode is unstable in their respective lobes, while linearly stable steady-state solutions occur outside the union of the lobes.

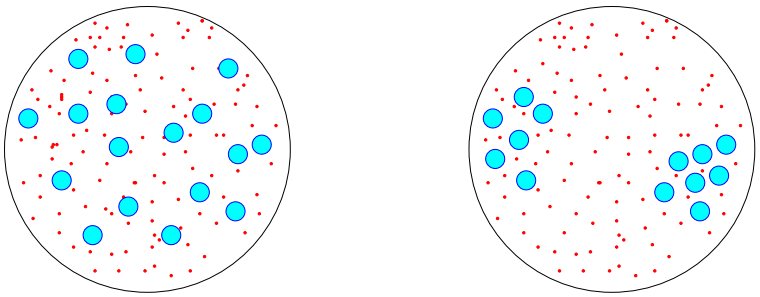

(a) *Randomly placed cells* (b) *Two clusters of cells*

Figure 16: Schematic showing different cell configurations in the unit disk. The cells are represented by smaller disks (in cyan) and the diffusing bulk species corresponds to the red dots. Left panel: randomly placed cells. Right panel: two spatially clustered groups of cells.

where $\boldsymbol{e} = (1, \ldots, 1)^T$ and $\mathcal{G}$ is the Green's interaction matrix defined in (2.7). In terms of the solution $\boldsymbol{\mathcal{A}}$ to (5.1a), we obtain from (2.28a) that the steady-state for the intracellular species $\boldsymbol{u}_e = (u_{ej}^1, u_{ej}^2)^T$ in each cell is

$$u_{ej}^1 = \mu + \frac{2\pi D}{\tau} A_j \,, \qquad \text{and} \qquad u_{ej}^2 = \frac{\mu}{\alpha + (u_{ej}^1)^2} \,. \tag{5.1b}$$

Since this simple steady-state construction is accurate to all orders in ν for any $D > 0$, we will not seek an approximation to it valid for the regime $D = \mathcal{O}(\nu^{-1})$. Therefore, in the GCEP matrix $\mathcal{M}(\lambda)$ given in (2.20a), the diagonal matrix $\mathcal{K}(\lambda)$, as defined in (2.19a), will be evaluated at the solution to (5.1). With Sel'kov kinetics, this yields

$$\mathcal{K} = \mathcal{K}(\lambda) \equiv \operatorname{diag}\Big(K_1, \ldots, K_m\Big) \,, \qquad \text{where} \qquad K_j = \frac{\lambda + \det(J_j)}{\lambda^2 - \lambda \operatorname{tr}(J_j) + \det(J_j)} \,, \tag{5.2a}$$

where J_j is the Jacobian matrix for the local Sel-kov kinetics at the j^{th} cell, for which

$$\det(J_j) = \zeta \left(\alpha + (u_{ej}^1)^2\right) \,, \qquad \operatorname{tr}(J_j) = \frac{\left[2\mu u_{ej}^1 - \left(\alpha + (u_{ej}^1)^2\right) - \zeta \left(\alpha + (u_{ej}^1)^2\right)^2\right]}{\alpha + (u_{ej}^1)^2} \,. \tag{5.2b}$$

Our goal in this subsection of determining a more tractable formula for determining the roots of $\det \mathcal{M}(\lambda) = 0$ when m is large and in the limit $D = D_0/\nu$, where $\nu = -1/\log \varepsilon$ and $D_0 = \mathcal{O}(1)$, is based on approximating the eigenvalue-dependent Green's matrix $\mathcal{G}_\lambda$ in (2.20a), while retaining the full $\mathcal{K}$ matrix, as defined in (5.2).

To do so, we readily calculate from (2.15) that when $D = D_0/\nu \gg 1$ we have (see [20])

$$\mathcal{G}_\lambda = \frac{D_0}{\nu|\Omega|(1+\tau\lambda)} + \mathcal{G}_0 + \mathcal{O}(\nu)\,. \tag{5.3}$$

Here $\mathcal{G}_0$ is the Neumann Green's matrix of (3.17) given in terms of the Neumann Green's function G_0 of (3.14), which is known analytically for the the unit disk in (3.21). By using (5.3) in (2.20a), we find that the GCEP matrix reduces to

$$\mathcal{M}(\lambda) = \mathcal{M}_\infty(\lambda) + \mathcal{O}(\nu^2)\,, \qquad \text{where} \qquad \mathcal{M}_\infty \equiv \mathcal{B} + \gamma E + 2\pi\nu\mathcal{G}_0\,. \tag{5.4a}$$

In (5.4a) the scalar γ, the rank-one matrix E and the diagonal matrix $\mathcal{B}$ are defined by

$$\gamma = \gamma(\lambda) \equiv \frac{2\pi m D_0}{(1+\tau\lambda)|\Omega|}\,, \qquad E \equiv \frac{1}{m}\boldsymbol{e}\,\boldsymbol{e}^T\,, \qquad \mathcal{B} = \mathcal{B}(\lambda) \equiv I + D_0 P_1 + \frac{2\pi D_0}{\tau} P_2\,\mathcal{K}(\lambda)\,. \tag{5.4b}$$

Neglecting terms of order $\mathcal{O}(\nu^2)$, in the limit $D = D_0/\nu \gg 1$ we conclude that the GCEP (2.20) reduces to finding values of λ for which there is a nontrivial solution $\boldsymbol{c}$ to

$$\mathcal{M}_\infty(\lambda)\boldsymbol{c} = \boldsymbol{0}\,, \qquad \text{which occurs iff} \qquad \det \mathcal{M}_\infty(\lambda) = 0\,. \tag{5.4c}$$

We remark that in our asymptotic reduction (5.4) of the GCEP (2.20), the cell configuration enters through the diagonal matrix $\mathcal{K}$, as defined in (5.2), and at order ν from the Neumann Green's matrix $\mathcal{G}_0$ in (5.4a).

To analyze (5.4) we first observe from (5.4b) and (5.2a) that

$$\mathcal{B} = \text{diag}(b_1, \ldots, b_m)\,, \qquad \text{where} \qquad b_j = \frac{(d_{1j}+D_0)}{d_{1j}}\left[1 + \frac{\eta_j}{\tau}K_j\right]\,, \qquad \eta_j \equiv \frac{2\pi d_{2j} D_0}{d_{1j}+D_0}\,, \quad j = 1, \ldots, m\,. \tag{5.5}$$

The key advantage of our asymptotic reduction is that by using the matrix structure in (5.4) we can readily calculate a tractable analytical expression for $\det\mathcal{M}_\infty(\lambda)$, which can be used in implementing the root-finding condition in (5.4c) numerically. Our first result for (5.4) in this direction is as follows:

Proposition 4. *Suppose that $b_j \neq 0$ for $j = 1, \ldots, m$ so that $\mathcal{B}$ is invertible. Then,*

$$det\mathcal{M}_\infty(\lambda) = det\,(\mathcal{B} + \gamma E + 2\pi\nu\mathcal{G}_0) = \left(\prod_{i=1}^m b_i\right)\kappa_{1\varepsilon}\,(1 + \mathcal{O}(\nu))\,, \tag{5.6}$$

where

$$\kappa_{1\varepsilon} \equiv 1 + \frac{\gamma}{m}\boldsymbol{e}^T\boldsymbol{v}_1 + 2\pi\nu\left(\frac{\boldsymbol{v}_1^T\,\mathcal{G}_0\,\boldsymbol{v}_1}{\boldsymbol{e}^T\,\boldsymbol{v}_1}\right) + \mathcal{O}(\nu^2)\,, \qquad with \qquad \boldsymbol{v}_1^T \equiv (1/b_1, \ldots, 1/b_m)\,. \tag{5.7}$$

Proof. Since $\mathcal{B}$ is a diagonal matrix and invertible by assumption, we have

$$\det\,(\mathcal{B} + \gamma E + 2\pi\nu\mathcal{G}_0) = \det(\mathcal{B})\det\left(I + \gamma\mathcal{B}^{-1}E + 2\pi\nu\mathcal{B}^{-1}\mathcal{G}_0\right)\,, \tag{5.8}$$

where $\det\mathcal{B} = \prod_{i=1}^m b_i$. The second term in (5.8) is calculated by multiplying all the eigenvalues κ_ε of

$$\left(I + \gamma\mathcal{B}^{-1}E + 2\pi\nu\mathcal{B}^{-1}\mathcal{G}_0\right)\boldsymbol{v}_\varepsilon = \kappa_\varepsilon\boldsymbol{v}_\varepsilon\,. \tag{5.9}$$

To determine $\mathcal{O}(\nu)$ accurate expressions for these eigenvalues we expand an eigenpair κ_ε and $\boldsymbol{v}_\varepsilon$ as

$$\kappa_\varepsilon = \kappa_1 + \nu\,\tilde{\kappa} + \cdots\,, \qquad \boldsymbol{v}_\varepsilon = \boldsymbol{v}_1 + \nu\,\tilde{\boldsymbol{v}} + \cdots\,. \tag{5.10}$$

Upon substituting (5.10) into (5.9) we equate powers of ν to obtain the leading-order problem

$$(I + \gamma\mathcal{B}^{-1}E)\,\boldsymbol{v}_1 = \kappa_1\,\boldsymbol{v}_1\,, \tag{5.11}$$

and the following problem at $\mathcal{O}(\nu)$:

$$(I + \gamma\mathcal{B}^{-1}E - \kappa_1 I)\,\tilde{\boldsymbol{v}} = \tilde{\kappa}\,\boldsymbol{v}_1 - 2\pi\mathcal{B}^{-1}\mathcal{G}_0\,\boldsymbol{v}_1\,. \tag{5.12}$$

For the leading order problem (5.11), we first observe that $E\,\boldsymbol{q}_j = \boldsymbol{0}$ for $j = 2, \ldots, m$, where $\text{span}\{\boldsymbol{q}_2, \ldots, \boldsymbol{q}_m\}$ is the $m-1$ dimensional subspace orthogonal to $\boldsymbol{e}$. We readily conclude that (5.11) has the eigenpairs

$$\kappa_{1j} = 1 \quad \text{and} \quad \boldsymbol{v}_{1j} = \boldsymbol{q}_j\,, \qquad \text{for} \quad j = 2, \ldots, m\,. \tag{5.13}$$

To determine the $\mathcal{O}(\nu)$ correction to these eigenvalues, we substitute (5.13) into (5.12) to obtain

$$\gamma \mathcal{B}^{-1} E \tilde{\boldsymbol{v}} = \tilde{\kappa} \boldsymbol{q}_j - 2\pi \mathcal{B}^{-1} \mathcal{G}_0 \boldsymbol{q}_j . \tag{5.14}$$

Since $\mathcal{B}\boldsymbol{q}_j$, with $\mathcal{B}^T = \mathcal{B}$, is a left null-vector of $\mathcal{B}^{-1}E$, the solvability condition for (5.14) is $\boldsymbol{q}_j^T \mathcal{B} \left(\tilde{\kappa} \boldsymbol{q}_j - 2\pi \mathcal{B}^{-1} \mathcal{G}_0 \boldsymbol{q}_j \right) = 0$, which determines $\tilde{\kappa}$ for each eigenpair. In this way, we obtain that $m-1$ eigenvalues of (5.9) are

$$\kappa_{j\varepsilon} = 1 + 2\pi\nu \frac{\boldsymbol{q}_j^T \mathcal{G}_0 \boldsymbol{q}_j}{\boldsymbol{q}_j^T \mathcal{B} \boldsymbol{q}_j} + \mathcal{O}(\nu^2) , \qquad \text{where} \quad \boldsymbol{q}_j^T \boldsymbol{e} = 0 , \quad \text{for} \quad j = 2, \ldots, m . \tag{5.15}$$

To find the remaining eigenpair of the leading order problem we write (5.11) as $\boldsymbol{v}_1(1-\kappa_1) = -\frac{\gamma}{m} \left(\boldsymbol{e}^T \boldsymbol{v}_1 \right) (1/b_1, \ldots, 1/b_m)^T$. This has the (unnormalized) nontrivial solution

$$\boldsymbol{v}_1 = (1/b_1, \ldots, 1/b_m)^T , \qquad \text{iff} \qquad \kappa_1 = 1 + \frac{\gamma}{m} \boldsymbol{e}^T \boldsymbol{v}_1 = 1 + \frac{\gamma}{m} \sum_{i=1}^{m} \frac{1}{b_i} . \tag{5.16}$$

To determine the $\mathcal{O}(\nu)$ correction to this eigenvalue we observe, for this eigenpair, that $\boldsymbol{e}$ is a left null-vector of the matrix in (5.12) since, by using (5.16) for κ_1, we calculate

$$\boldsymbol{e}^T \left(I + \gamma \mathcal{B}^{-1} E - \kappa_1 I \right) = \boldsymbol{e}^T \left(1 + \frac{\gamma}{m} \left(\sum_{i=1}^{m} \frac{1}{b_i} \right) - \kappa_1 \right) = \boldsymbol{0} . \tag{5.17}$$

Therefore, upon left-multiplying (5.12) by $\boldsymbol{e}^T$, the solvability condition for (5.12) is $\boldsymbol{e}^T \left(\tilde{\kappa} \boldsymbol{v}_1 - 2\pi \mathcal{B}^{-1} \mathcal{G}_0 \boldsymbol{v}_1 \right) = 0$, which yields $\tilde{\kappa} = 2\pi \boldsymbol{v}_1^T \mathcal{G}_0 \boldsymbol{v}_1 / \left(\boldsymbol{e}^T \boldsymbol{v}_1 \right)$ where we used $\boldsymbol{e}^T \mathcal{B}^{-1} = \boldsymbol{v}_1^T$. We conclude that a two-term expansion $\kappa_{1\varepsilon} = \kappa_1 + \tilde{\kappa}\nu$ for this remaining eigenvalue of (5.9) is as given in (5.7). Finally, by multiplying $\kappa_{1\varepsilon}$ with the other eigenvalues given in (5.15) we obtain $\det \left(I + \gamma \mathcal{B}^{-1} E + 2\pi\nu \mathcal{B}^{-1} \mathcal{G}_0 \right) = \kappa_{1\varepsilon}(1 + \mathcal{O}(\nu))$. In view of (5.8) this completes the derivation of (5.6).

□

The key assumption in Proposition 4 is that $b_j \neq 0$ for any $j = 1, \ldots, m$. By using (5.5) and (5.2a) for b_j and K_j, respectively, we conclude that $b_j = 0$ if and only if λ is a root of the quadratic equation $\mathcal{Q}_j(\lambda) = 0$, where

$$\mathcal{Q}_j(\lambda) \equiv \lambda^2 - \left(\mathrm{tr}(J_j) - \frac{\eta_j}{\tau} \right) \lambda + \det(J_j) \left[1 + \frac{\eta_j}{\tau} \right] , \qquad \text{where} \quad \eta_j \equiv \frac{2\pi d_{2j} D_0}{d_{1j} + D_0} , \tag{5.18}$$

with $\det(J_j)$ and $\mathrm{tr}(J_j)$ as given in (5.2b). With this criterion and together with Proposition 4 we readily formulate a simple scalar root-finding problem to identify values of λ for which the reduced GCEP (5.4) has a nontrivial solution.

Proposition 5. *Suppose that $\lambda = \lambda^\star$ is a root of $\mathcal{Q}_s(\lambda) = 0$, where*

$$\mathcal{Q}_s(\lambda) \equiv 1 + \frac{\gamma}{m} \boldsymbol{e}^T \boldsymbol{v}_1 + 2\pi\nu \left(\frac{\boldsymbol{v}_1^T \mathcal{G}_0 \boldsymbol{v}_1}{\boldsymbol{e}^T \boldsymbol{v}_1} \right) \qquad \text{with} \qquad \boldsymbol{v}_1^T \equiv (1/b_1, \ldots, 1/b_m) . \tag{5.19}$$

Here $\gamma = \gamma(\lambda)$ and $b_j = b_j(\lambda)$ for $j = 1, \ldots, m$ are given in (5.4b) and (5.5), respectively. Suppose that $\lambda^\star$ satisfies

$$\lambda^\star \notin \bigcup_{j=1}^{m} \{\lambda_{j\pm}\} , \qquad \text{where} \quad \mathcal{Q}_j(\lambda_{j\pm}) = 0 , \tag{5.20}$$

and $\mathcal{Q}_j(\lambda)$ is the quadratic defined in (5.18). Then, $\det \mathcal{M}_\infty(\lambda^\star) = 0$ and the corresponding (unnormalized) nontrivial solution $\boldsymbol{c}$ to the reduced GCEP (5.4c) is

$$\boldsymbol{c} = \left(\frac{1}{b_1(\lambda^\star)}, \ldots, \frac{1}{b_m(\lambda^\star)} \right)^T + \mathcal{O}(\nu) \tag{5.21}$$

In this way, we can use Proposition 5 to determine Hopf bifurcation boundaries in the τ versus D_0 parameter plane by simply letting $\lambda = i\lambda_I$, with $\lambda_I > 0$, and setting

$$\mathrm{Re}\left[\mathcal{Q}_s(i\lambda_I) \right] = 0 , \qquad \text{and} \qquad \mathrm{Im}\left[\mathcal{Q}_s(i\lambda_I) \right] = 0 , \tag{5.22}$$

while ensuring that the condition (5.20) holds with $\lambda^\star = i\lambda_I$. A sufficient condition for (5.20) to hold along solutions of (5.22) as parameters are varied is that $\mathrm{tr}(J_j) \neq \eta_j/\tau$ for all $j = 1, \ldots, m$.

A simple analytically tractable special case of Proposition 5 is when the permeabilities are all identical, i.e. $d_{1j} = d_{1c}$, $d_{2j} = d_{2c}$, and when the cell configuration $\{\boldsymbol{x}_1, \ldots, \boldsymbol{x}_m\}$ is such that $\boldsymbol{e}$ is an eigenvector of the reduced-wave Green's matrix

$\mathcal{G}$, and consequently the Neumann Green's matrix $\mathcal{G}_0$. Therefore, $\mathcal{G}_0\boldsymbol{e} = \beta\boldsymbol{e}$ for some eigenvalue β. A ring patterns of cells concentric within the unit disk with common cell permeabilities and Sel'kov parameters is an example of such a cell pattern. For this case, (5.1) admits the solution $\mathcal{A} = A_c\boldsymbol{e}$ and so $J_j = J_c$ for $j = 1, \ldots, m$. Since $b_j = b_c$ for $j = 1, \ldots, m$, we can take $\boldsymbol{v}_1 = b_c^{-1}(1, \ldots, 1)^T$ and readily obtain that the root-finding condition $\mathcal{Q}_s(\lambda) = 0$ in (5.19) reduces to

$$1 + \frac{\gamma}{b_c} + \frac{2\pi\nu}{mb_c}\boldsymbol{e}^T\mathcal{G}_0\boldsymbol{e} = 0\,, \qquad \text{where} \qquad \mathcal{G}_0\boldsymbol{e} = \beta\boldsymbol{e}\,, \tag{5.23}$$

while from (5.18) we have $\mathcal{Q}_j(\lambda) = \mathcal{Q}_c(\lambda)$ for $j = 1, \ldots, m$, where

$$\mathcal{Q}_c(\lambda) \equiv \lambda^2 - \left(\mathrm{tr}(J_c) - \frac{\eta_c}{\tau}\right)\lambda + \det(J_c)\left[1 + \frac{\eta_c}{\tau}\right], \qquad \text{where} \quad \eta_c \equiv \frac{2\pi d_{2c}D_0}{d_{1c} + D_0}\,, \tag{5.24}$$

By using (5.5) and (5.2a), we obtain after a little algebra that (5.23) reduces to

$$\frac{\lambda + \det(J_c)}{\lambda^2 - \lambda\,\mathrm{tr}(J_c) + \det J_c} = -\frac{\tau}{2\pi d_{2c}}\left[1 + \frac{d_{1c}}{D_0}\left(1 + 2\pi\nu\beta\right) + \frac{2\pi m d_{1c}}{|\Omega|(1 + \tau\lambda)}\right], \tag{5.25}$$

which is a cubic equation in λ. For this special cell pattern, we conclude that if $\lambda = \lambda^\star$ is a root of (5.25) for which $Q_c(\lambda^\star) \neq 0$, then $\det \mathcal{M}_\infty(\lambda^\star) = 0$. The corresponding eigenvector of $\mathcal{M}_\infty(\lambda^\star)$ is the in-phase mode $\boldsymbol{c} = \boldsymbol{e}$.

Next, we will show how to determine roots of the reduced GCEP (5.4c) in the case where $\mathcal{B}(\lambda) = \mathrm{diag}\,(b_1(\lambda), \ldots, b_m(\lambda))^T$ in (5.4b) is not invertible. We first observe that a nontrivial $\boldsymbol{c}$ to the leading order problem in (5.4c) (with $\nu = 0$), exists if and only if there is a $\lambda = \lambda^\star$ at which *at least two* b_j cross through zero simultaneously. After relabelling the indices as necessary, this occurs without loss of generality when there is a $\lambda^\star$ and an integer J with $2 \le J \le m$ for which

$$b_1(\lambda^\star) = \ldots = b_J(\lambda^\star) = 0\,, \quad \text{with} \quad b_j(\lambda^\star) \neq 0 \quad \text{for} \quad j = J+1, \ldots, m \quad \text{if} \quad J < m\,. \tag{5.26}$$

Then, for the leading-order problem in (5.4c) at $\lambda = \lambda^\star$ the nontrivial solutions $\boldsymbol{c}_0$ are

$$(\mathcal{B}(\lambda^\star) + \gamma(\lambda^\star)E)\,\boldsymbol{c}_0 = \boldsymbol{0}\,, \quad \Longrightarrow \quad \boldsymbol{c}_0 \in \mathcal{C}^\perp \equiv \left\{\boldsymbol{c}_0 \,\middle|\, \boldsymbol{e}^T\boldsymbol{c}_0 = 0\,,\ \boldsymbol{c}_0 = \begin{pmatrix}\boldsymbol{c}_J\\ \boldsymbol{0}\end{pmatrix},\ \boldsymbol{c}_J \in \mathbb{R}^J\,,\ \boldsymbol{0} \in \mathbb{R}^{m-J}\right\}. \tag{5.27}$$

Next, we introduce an orthonormal basis for the subspace $\mathcal{C}^\perp$ of dimension $J-1$ and we decompose $\boldsymbol{c}_0$ as

$$\boldsymbol{c}_0 = \omega_1\boldsymbol{v}_1 + \ldots + \omega_{J-1}\boldsymbol{v}_{J-1}\,, \qquad \text{where} \qquad \mathcal{C}^\perp \equiv \mathrm{span}\{\boldsymbol{v}_1, \ldots, \boldsymbol{v}_{J-1}\}\,, \qquad \boldsymbol{v}_j^T\boldsymbol{v}_i = \delta_{ij}\,, \tag{5.28}$$

where δ_{ij} is the Kronecker symbol, and ω_j for $j = 1, \ldots, J-1$ are scalar coefficients to be found.

To determine the $\mathcal{O}(\nu)$ correction to the leading-order eigenvalue $\lambda^\star$ of the GCEP and identify the constants ω_j, we look for a nontrivial solution to $\mathcal{M}_\infty(\lambda)\boldsymbol{c} = \boldsymbol{0}$, as defined in (5.4), of the form $\lambda = \lambda^\star + \mathcal{O}(\nu)$. We substitute the expansion

$$\lambda = \lambda^\star + \nu\tilde{\lambda} + \cdots\,, \qquad \boldsymbol{c} = \boldsymbol{c}_0 + \nu\boldsymbol{c}_1 + \cdots\,, \tag{5.29}$$

into (5.4) and then equate $\mathcal{O}(\nu)$ terms to obtain

$$(\mathcal{B}(\lambda^\star) + \gamma(\lambda^\star)E)\,\boldsymbol{c}_1 = -\tilde{\lambda}\gamma'(\lambda^\star)E\boldsymbol{c}_0 - \tilde{\lambda}\mathcal{B}'(\lambda^\star)\boldsymbol{c}_0 - 2\pi\mathcal{G}_0\boldsymbol{c}_0\,, \tag{5.30}$$

where we observe that $E\boldsymbol{c}_0 = \boldsymbol{0}$. The solvability condition for (5.30) is that the right-hand side of (5.30) is orthogonal to each $\boldsymbol{v}_j$ for $j = 1, \ldots, J-1$. In this way, we readily obtain that $\tilde{\lambda}$ and $\boldsymbol{\omega} \equiv (\omega_1, \ldots, \omega_{J-1})^T$ are eigenpairs of the $J-1$ dimensional symmetric generalized matrix eigenvalue problem

$$\mathcal{V}^T\mathcal{G}_0\mathcal{V}\boldsymbol{\omega} = -\frac{\tilde{\lambda}}{2\pi}\mathcal{V}^T\mathcal{B}'(\lambda^\star)\mathcal{V}\boldsymbol{\omega}\,, \qquad \mathcal{V} \equiv \begin{pmatrix}\boldsymbol{v}_1\,, & \ldots & ,\boldsymbol{v}_{J-1}\end{pmatrix}. \tag{5.31}$$

Here $\mathcal{V}$ is the $m \times J-1$ matrix whose columns provide an orthonormal basis for $\mathcal{C}^\perp$. In summary, for any such $\tilde{\lambda}$ satisfying (5.31) a two-term expansion for a root of the reduced GCEP $\det\mathcal{M}_\infty(\lambda) = 0$ is $\lambda = \lambda^\star + \nu\tilde{\lambda}$ where $\lambda^\star$ satisfies (5.26).

We now illustrate this theory for the special case where $J = 2$. This analysis, given below, will be shown in §5.1.1 to be relevant for analyzing anti-phase instabilities associated with the cell configuration of Fig. 23b where a pair of isolated identical cells is spatially segregated from two symmetric ring clusters. Suppose that cells 1 and 2 have common permeabilities $d_{1c} \equiv d_{11} = d_{12}$, $d_{2c} \equiv d_{21} = d_{22}$ and that they have the same intracellular steady-states. Then, from (5.2) we obtain $\mathrm{tr}J_c \equiv \mathrm{tr}J_1 = \mathrm{tr}J_2$, $\det J_c \equiv \det J_1 = \det J_2$, and so (5.5) and (5.2a) yields that $b_c(\lambda) \equiv b_1(\lambda) = b_2(\lambda)$. Then, in (5.31) we can take $\mathcal{V} = \left(1/\sqrt{2}, -1/\sqrt{2}\right)^T$, and readily calculate that $\tilde{\lambda} = -2\pi R_c/b_c'(\lambda^\star)$, where $b_c(\lambda^\star) = 0$. Here $R_c \equiv R_0(\boldsymbol{x}_1) = R_0(\boldsymbol{x}_2)$ is the common value of the regular part of the Neumann Green's function at the centers $\boldsymbol{x}_1$ and $\boldsymbol{x}_2$ of the two cells. For $\nu \ll 1$,

a simple perturbation argument shows that $\lambda \sim \lambda^\star + \nu\tilde{\lambda}$ can be identified as the root to $b_c(\lambda) + 2\pi\nu R_c = 0$. Finally, by using (5.5) for b_c, together with (5.2), we conclude for $\nu \ll 1$ that λ must be a root of the quadratic

$$\lambda^2 - \lambda\left(\mathrm{tr}J_c - \frac{\eta_c}{\tau f}\right) + \left(1 + \frac{\eta_c}{\tau f}\right)\det J_c = 0\,, \qquad \text{where} \qquad \eta_c \equiv \frac{2\pi d_{2c} D_0}{d_{1c} + D_0}\,, \quad f \equiv 1 + \frac{2\pi\nu d_{1c}}{d_{1c} + D_0} R_c\,. \tag{5.32}$$

Since $\det J_c > 0$, an anti-phase instability occurs for cells 1 and 2, with the other cells remaining quiescent, only when

$$\mathrm{tr}(J_c) - \frac{\eta_c}{\tau f} > 0\,. \tag{5.33}$$

Although this criterion gives a region in the (D_0, τ) parameter plane, in §5.1.1 we will only implement it for the cell configuration in Fig. 23b at a fixed value of τ in order to determine a threshold in D_0.

5.1 Example: $m = 10$ cells in the unit disk

We now apply our simplified theory for the regime $D = \mathcal{O}(\nu^{-1})$ to a population of $m = 10$ cells in the unit disk. Different spatial configurations of these cells are considered, and we will focus on three different scenarios: (a) all cells are identical, (b) some groups of cells are identical and, (c) none of the cells are identical. For all the examples considered in this subsection, the cells have a common radius $\varepsilon = 0.05$ and common Sel'kov kinetic parameters as given in (4.22). The heterogeneity in the cells is introduced through the cell locations and their permeability parameters d_{1j}, $j = 1, \ldots, m$, which specifies the rate of feedback of the bulk signal into the cells. The secretion rate is fixed at $d_2 = 0.2$ for all the cells. For each spatial configuration of cells and permeability parameter set $d_{11}, \ldots, d_{1m}$ we will compute the HB bifurcation boundary in the τ versus D_0 plane by solving (5.22) numerically using Newton's method with arclength continuation in D_0.

In Fig. 17 we plot the HB boundaries (left panel) in the τ versus D_0 parameter plane together with the cell pattern (right panel) for a pattern with two clusters of cells (top row) and a pattern with an arbitrary arrangement of cells (bottom row). The precise locations and influx rate d_{1j} for the cells for these two specific configurations are given in Table 4 of Appendix B. By using a numerical winding number computation we have verified that there are exactly two roots of (5.19), corresponding to two unstable eigenvalues of the GCEP matrix, inside the lobes spanned by the HB boundaries.

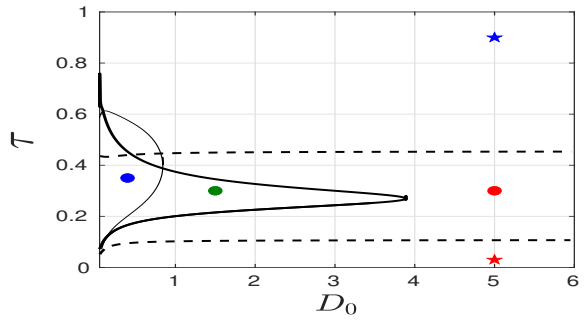

(a) HB boundaries

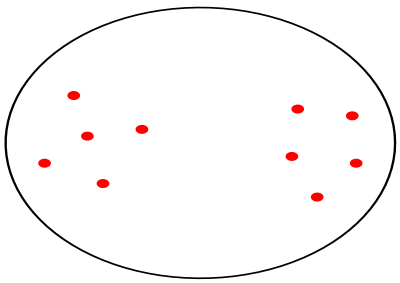

(b) Two spatially segregated clusters of cells

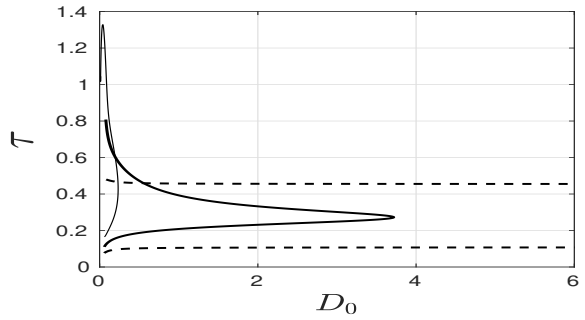

(c) HB boundaries

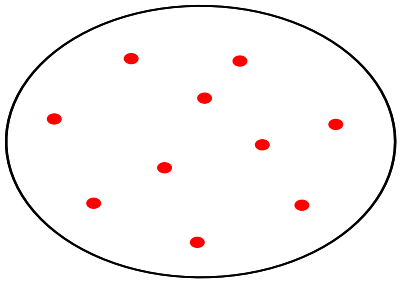

(d) Arbitrary (random) arrangement of cells

Figure 17: HB boundaries in the τ versus D_0 plane for $m = 10$ cells with two groups/clusters of cells (top row) and arbitrarily placed cells (bottom row). The dashed curve corresponds to identical cells where $d_1 = 0.8$ for each cell. The thin solid curve is for when there are two groups of identical cells with $d_1 = 0.8$ for the first group and $d_1 = 0.4$ for the second group (permeability set II). The heavy solid curve is for non-identical cells with d_1 uniformly selected from the interval $0.4 \le d_1 \le 0.8$ (permeability set III). The locations and influx rates d_{1j} for the cells are given in Table 4 of Appendix B. The remaining parameters are as given in (4.22).

By comparing the HB boundaries in Fig. 17a and Fig. 17c we observe from the dashed lines in these figures that when the cells are all identical (with $d_1 = 0.8$ for each cell) the unbounded region of instability in the (D_0, τ) parameter plane is very

similar for the two cell patterns. Therefore, when D_0 is large and when there are a sufficiently large number of identical cells, this observation suggests that the parameter region where intracellular oscillations occur should depend only weakly on the spatial configuration of cells. In addition, by comparing the heavy solid curves in Fig. 17a and Fig. 17c, we conclude that the HB boundaries for cell patterns where d_1 is uniformly selected from the interval $0.4 \le d_1 \le 0.8$ (permeability set III) also depend only weakly on the spatial arrangement of the cells, but that there are no intracellular oscillations when D_0 is large. The influx rates d_{1j} for the cells are given in Table 4 of Appendix B. In this case, the bounded instability region in the (D_0, τ) plane exists only within a rather narrow range of τ, which measures the ratio of the time-scale for the reaction kinetics to the decay rate of the bulk signal. From the thin solid curve in Fig. 17a, corresponding to where we assign the different influx rates $d_1 = 0.8$ and $d_1 = 0.4$ to all the cells in the two different groups (permeability set II in Table 4 of Appendix B), we observe that the parameter region where intracellular oscillations occur is rather small in D_0 but has a larger extent in τ. Even when D_0 is small, identical cells within a cluster are in close proximity and so are able to synchronize their activities and generate oscillations within their respective group. However, as D_0 increases, the bulk signal diffuses rapidly away from each of the two clusters and this signal no longer has a sufficient spatial gradient to coordinate synchronized oscillations between the two spatially segregated groups of cells. For an arbitrary arrangement of cells, we observe from the thin solid curve in Fig. 17c that when cells are assigned either $d_1 = 0.8$ or $d_1 = 0.4$ in such a way that two neighboring cells are not identical, intracellular oscillations only occur when D_0 is significantly smaller than for the case when the cells with the same influx rates are clustered. Qualitatively, this indicates that identical cells within a group of more closely spaced cells can more readily synchronize their activity.

For the case of two clustered groups of cells (see Fig. 17b), we will validate our linear stability predictions with full numerical results computed from the coupled PDE-ODE model (1.2) using FlexPDE [14] at the indicated points in the HB phase diagram in Fig. 17a and for specific permeability sets. In Table 3 we show the real and imaginary parts of the components of the normalized eigenvectors $\boldsymbol{c}$ and $\mathcal{K}\boldsymbol{c}$, together with the unique complex conjugate pair of unstable eigenvalues of the 10×10 GCEP matrix $\mathcal{M}(\lambda)$ in (2.20a), as computed from the root-finding condition $\det \mathcal{M}(\lambda) = 0$, at the red, blue, and green dots shown in the phase diagram in Fig. 17a. In Table 4 of Appendix B we indicate the specific permeability set for the influx rate used at these three pairs of (D_0, τ). From (2.24), the components of $\boldsymbol{c}$ measure the diffusive flux into the cells, while $\tilde{\boldsymbol{c}} \equiv \mathcal{K}\boldsymbol{c}$, with $\mathcal{K}$ given in (5.2), predicts the relative amplitude and phase shifts of the intracellular oscillations.

In the top row of Fig. 18 we show FlexPDE simulation results of (1.2) corresponding to the red dot at $(D_0, \tau) = (5, 0.3)$ in the phase diagram of Fig. 17a for the case where the cells are all identical with $d_{1j} = 0.8$ for $j = 1, \ldots, 10$. The eigenpair $\boldsymbol{c}$ and $\mathcal{K}\boldsymbol{c}$ of the GCEP matrix is given in the top third of Table 3. As predicted by the eigenvector $\mathcal{K}\boldsymbol{c}$ of the linearized theory, the intracellular oscillations observed in the full simulations are nearly synchronized both in amplitude and phase. In the bottom row of Fig. 18 we show, for this parameter set, that results computed from the ODE system (3.16). We observe that the amplitude and period of intracellular oscillations predicted by the ODEs (3.16) compare very favorably with corresponding FlexPDE results computed from (1.2). To explain this very favorable comparison, we observe from the surface plot in Fig. 18a that the bulk signal is roughly spatially uniform when $D_0 = 5$. Recall that the asymptotic analysis for the derivation of the ODE system (3.16) in §3 relies on a nearly spatially uniform bulk signal.

In the top row of Fig. 19 we show full FlexPDE results computed from (1.2) at the blue and red stars in Fig. 17a corresponding to $(D_0, \tau) = (5, 0.9)$ (top left panel) and $(D_0, \tau) = (5, 0.03)$ (top right panel), respectively. In this case, where the cells are all identical with $d_1 = 0.8$, the linear stability analysis predicts that the steady-state is linearly stable and that no sustained intracellular oscillations should occur. This prediction is confirmed from the FlexPDE simulations. In the bottom panels of Fig. 19 we show that the corresponding results predicted by the ODE system (3.16) compare very favorably with the FlexPDE results with regards to the long time limiting behavior. At the red star point in Fig. 17a we calculate from the root-finding condition $\det \mathcal{M}(\lambda) = 0$, where $\mathcal{M}$ is given in (2.20a), that the eigenvalue nearest the origin in $\mathrm{Re}(\lambda) < 0$ is $\lambda \approx -1.01 + 0.000202\, i$. This predicts a monotone, non-oscillatory, decay to the steady-state. This feature is observed in the right panels of Fig. 19. Alternatively, at the blue star point in Fig. 19 we calculate that the nearest eigenvalue in $\mathrm{Re}(\lambda) < 0$ for the GCEP matrix at $(D_0, \tau) = (5.0, 0.9)$ is $\lambda \approx -0.030 + 0.8104\, i$. This eigenvalue predicts an oscillatory decay to the steady-state, and is confirmed by the results in the left panels of Fig. 19. To further explain this transition between monotone and oscillatory decay to the steady-state, in Fig. 20 we plot the real and imaginary parts of the eigenvalue with the largest real part of the GCEP matrix along the vertical slice $D_0 = 5$ for $0.03 \le \tau \le 0.9$ in the phase diagram in Fig. 17a, as obtained by numerically solving $\det \mathcal{M}(\lambda) = 0$. This figure shows that the imaginary part of this eigenvalue becomes small when τ decreases below the lower HB boundary.

In the top and middle rows of Fig. 21 we show FlexPDE simulation results corresponding to the blue dot in Fig. 17a where $(D_0, \tau) = (0.4, 0.35)$. For this case, the influx rate for the cells in the right and left clusters were assigned as $d_1 = 0.8$ and $d_1 = 0.4$, respectively (parameter set II in Table 4 of Appendix B). The corresponding normalized eigenpair $\mathcal{K}\boldsymbol{c}$ obtained from the GCEP matrix, as given in the middle third of Table 3, predicts that the cells will synchronize their oscillations within their respective groups, but that there will be a slight phase difference in the intracellular oscillations between the two groups. The results from the full FlexPDE simulations in the middle row of Fig. 21 confirm these predictions from the linearized theory. However, from comparing the middle and bottom rows of Fig. 21, we observe that results from the ODE system (3.16) do not compare as favorably with FlexPDE simulations as they do in Fig. 18 when $D_0 = 5$. This poorer agreement is likely due to the fact that there is a noticeable spatial gradient in the bulk signal at the lower value $D_0 = 0.4$,

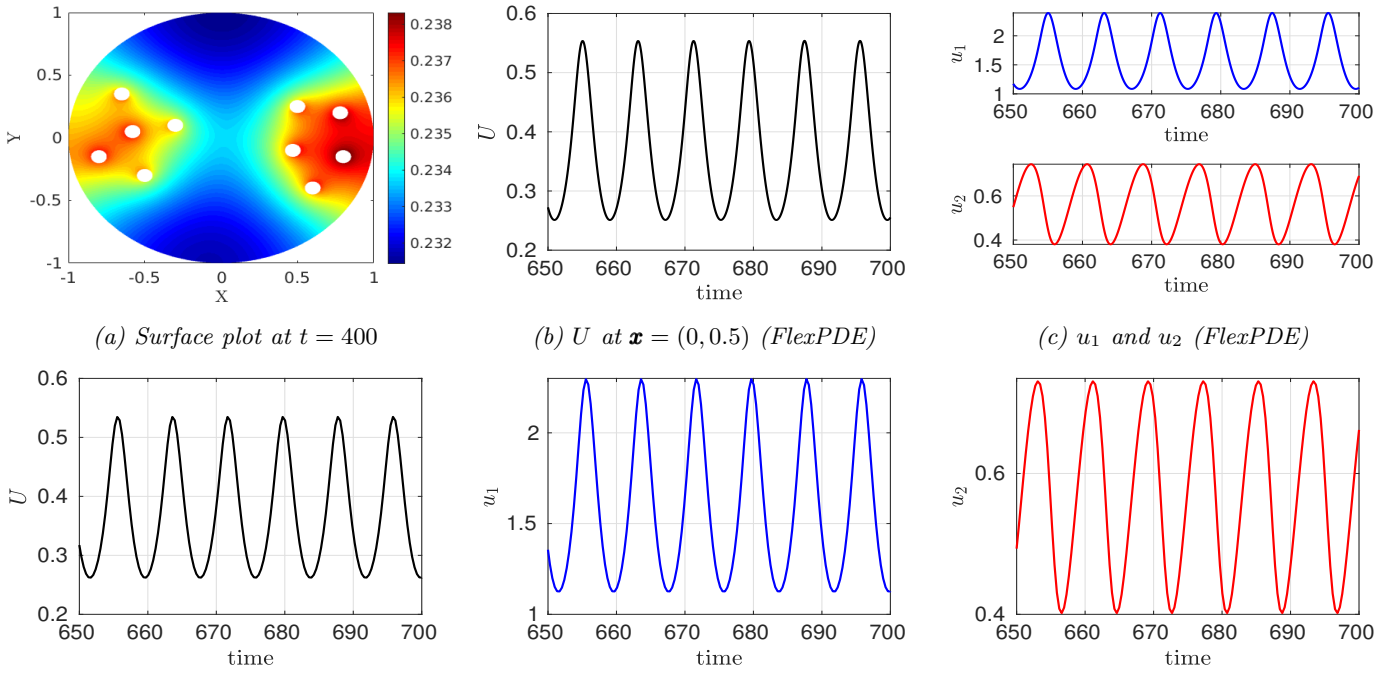

(a) *Surface plot at* $t = 400$ (b) U *at* $\boldsymbol{x} = (0, 0.5)$ *(FlexPDE)* (c) u_1 *and* u_2 *(FlexPDE)*

(d) $\bar{U}$ *(ODEs)* (e) u_1 *(ODEs)* (f) u_2 *(ODEs)*

Figure 18: Top row: FlexPDE numerical results computed from the PDE-ODE model (1.2) for $m = 10$ *identical cells, arranged in two clusters (see Fig. 17b), at the red dot in Fig. 17a where* $(D_0, \tau) = (5.0, 0.3)$*. The cells have identical influx rates* $d_{1j} = 0.8$ *for* $j = 1, \ldots, m$ *(set I) and almost identical intracellular dynamics. The cell locations are in Table 4 of Appendix B. Lower row: corresponding results for* $\bar{U}$*,* u_1*, and* u_2*, as computed from the ODE system (3.16). The eigenvector and eigenvalue for the GCEP matrix for the linearization are in the top third of Table 3. The results from the ODEs compare well with the FlexPDE simulations.*

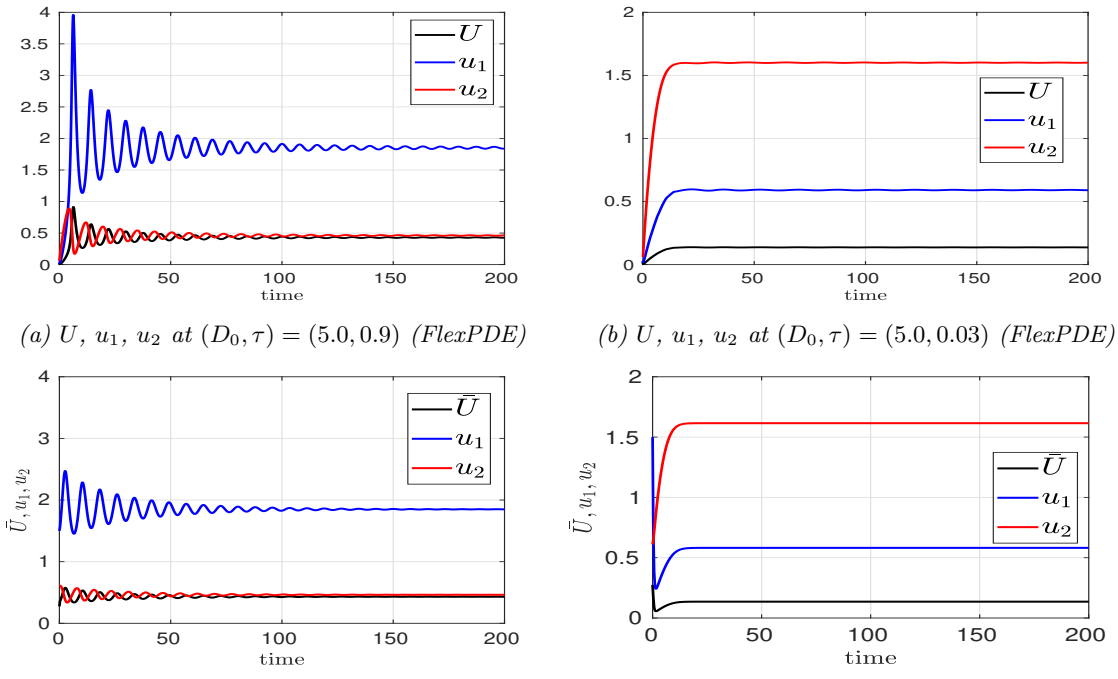

(a) U, u_1, u_2 *at* $(D_0, \tau) = (5.0, 0.9)$ *(FlexPDE)* (b) U, u_1, u_2 *at* $(D_0, \tau) = (5.0, 0.03)$ *(FlexPDE)*

(c) $\bar{U}$, u_1, u_2 *at* $(D_0, \tau) = (5.0, 0.9)$ *(ODEs)* (d) $\bar{U}$, u_1, u_2 *at* $(D_0, \tau) = (5.0, 0.03)$ *(ODEs)*

Figure 19: Top row: FlexPDE numerical results computed from the PDE-ODE model (1.2) for $m = 10$ *identical cells, arranged in two clusters (see Fig. 17b) at the blue star in Fig. 17a where* $(D_0, \tau) = (5.0, 0.9)$ *(left panel) and at the red star in Fig. 17a where* $(D_0, \tau) = (5.0, 0.03)$ *(right panel). The cells have identical influx rates* $d_{1j} = 0.8$ *for* $j = 1, \ldots, 10$ *(set I) and almost identical intracellular dynamics. The cell locations are in Table 4 of Appendix B. Lower row: corresponding results for* $\bar{U}$*,* u_1*, and* u_2*, as computed from the ODE system (3.16). As expected, there are no sustained oscillations and the steady-state is stable.*

Permeability set	$(D_0,\tau)\,;\ D=D_0/\nu$	$(\mathrm{Re}\lambda,\mathrm{Im}\lambda)$	Cell j	$\Big(\mathrm{Re}(c_j),\mathrm{Im}(c_j)\Big)$	θ_j (rad)	$\Big(\mathrm{Re}(\tilde{c}_j),\mathrm{Im}(\tilde{c}_j)\Big)$
Identical cells (Set I)	$(5,0.3)$ $D\approx 14.98$ Red dot	$(0.0198,0.7802)$	1	$(0.316,0.0000)$	0.0000	$(-0.309,0.0670)$
			2	$(0.312,0.00137)$	0.0044	$(-0.310,0.0669)$
			3	$(0.309,0.00236)$	0.0076	$(-0.310,0.0668)$
			4	$(0.319,-0.00103)$	6.284	$(-0.308,0.0670)$
			5	$(0.317,-0.000415)$	6.28	$(-0.309,0.0670)$
			6	$(0.315,0.000335)$	0.0011	$(-0.309,0.0670)$
			7	$(0.320,-0.00146)$	6.28	$(-0.309,0.0671)$
			8	$(0.314,0.00512)$	0.0016	$(-0.309,0.0670)$
			9	$(0.321,-0.00201)$	6.28	$(-0.308,0.0671)$
			10	$(0.321,-0.00183)$	6.28	$(-0.308,0.0671)$
Two groups (Set II)	$(0.4,0.35)$ $D\approx 1.198$ Blue dot	$(0.00772,0.766)$	1	$(0.0718,0.0000)$	0.0000	$(-0.135,0.290)$
			2	$(0.0751,-0.00850)$	6.17	$(-0.135,0.273)$
			3	$(0.0693,0.000272)$	0.0039	$(-0.136,0.270)$
			4	$(0.0802,-0.0145)$	6.10	$(-0.133,0.289)$
			5	$(0.0817,-0.0185)$	6.06	$(-0.133,0.283)$
			6	$(0.208,-0.369)$	5.23	$(-0.123,0.307)$
			7	$(0.204,-0.397)$	5.19	$(-0.116,0.299)$
			8	$(0.210,-0.365)$	5.23	$(-0.125,0.311)$
			9	$(0.197,-0.4127)$	5.16	$(-0.109,0.283)$
			10	$(0.201,-0.406)$	5.17	$(-0.112,0.292)$
Random (Set III)	$(1.5,0.3)$ $D\approx 4.494$ Green dot	$(0.00230,0.765)$	1	$(0.450,0.000)$	0.0000	$(-0.246,0.00135)$
			2	$(0.359,0.0635)$	0.175	$(-0.302,-0.00586)$
			3	$(0.430,0.0277)$	0.0643	$(-0.269,-0.00193)$
			4	$(0.242,0.0834)$	0.331	$(-0.331,-0.00735)$
			5	$(0.0215,0.0775)$	1.30	$(-0.368,-0.00610)$
			6	$(0.260,0.0823)$	0.307	$(-0.324,-0.00917)$
			7	$(0.117,0.0854)$	0.630	$(-0.352,-0.00935)$
			8	$(0.436,0.0192)$	0.0439	$(-0.259,-0.00170)$
			9	$(0.331,0.0697)$	0.208	$(-0.307,-0.00665)$
			10	$(-0.0421,0.0687)$	2.12	$(-0.376,-0.00609)$

Table 3: Real and imaginary parts of the normalized eigenvector $\boldsymbol{c}$ of the GCEP matrix (2.20a), together with $\tilde{\boldsymbol{c}}\equiv\mathcal{K}\boldsymbol{c}$, computed at the red, blue, and green dot shown in the phase diagram in Fig. 17a for a two-cluster arrangement of cells shown in Fig. 17b. The cell locations and permeability sets for the influx rate are given in Table 4 of Appendix B. The other parameters are as given in (4.22). The third column gives the unique unstable eigenvalue in $Re(\lambda)>0$ of the GCEP matrix at these three pairs of (D_0,τ).

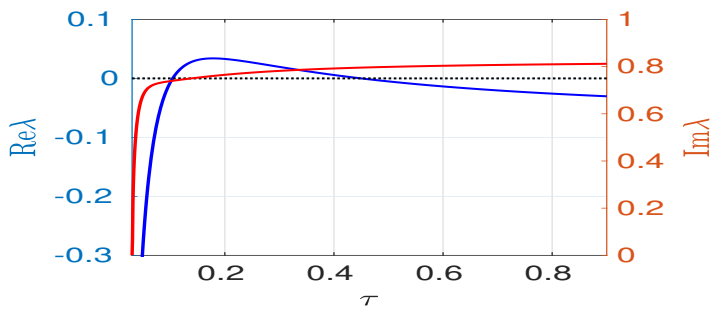

Figure 20: Real (blue curve; left y axis) and imaginary (red curve; right y axis) parts of the eigenvalue of the GCEP matrix with the largest real part versus τ along the vertical slice $D_0=5$ for $0.03\le\tau\le 0.9$ in the phase diagram in Fig. 17a. The eigenvalue is computed using root-finding on $\det\mathcal{M}(\lambda)=0$, where $\mathcal{M}(\lambda)$ is given in (2.20a). Observe the two HB values in τ where $Re(\lambda)=0$ (dotted black line). When $\tau=0.9$, we have $Im(\lambda)\approx 0.81$. However, as τ decreases below the lower HB point, $Im(\lambda)$ decreases to zero.

as observed from the surface plot of Fig. 21a. Moreover, Fig. 21a shows that the bulk signal can concentrate, as expected, in the left cluster owing to the lower rate of chemical influx into the cells in this cluster.

Next, we give FlexPDE results computed from (1.2) corresponding to the green dot in Fig. 17a where $(D_0,\tau)=(1.5,0.3)$, corresponding to the two cluster cell pattern of Fig. 17b). For this case, the influx rates are selected randomly from the interval $0.4\le d_1\le 0.8$ and are given in Table 4 under permeability set III. In the top and middle row of Fig. 22 we show the FlexPDE results for the bulk solution at the point $(0,0.5)$ as well as the intracellular dynamics in cells 1, 2, 6 and 7.

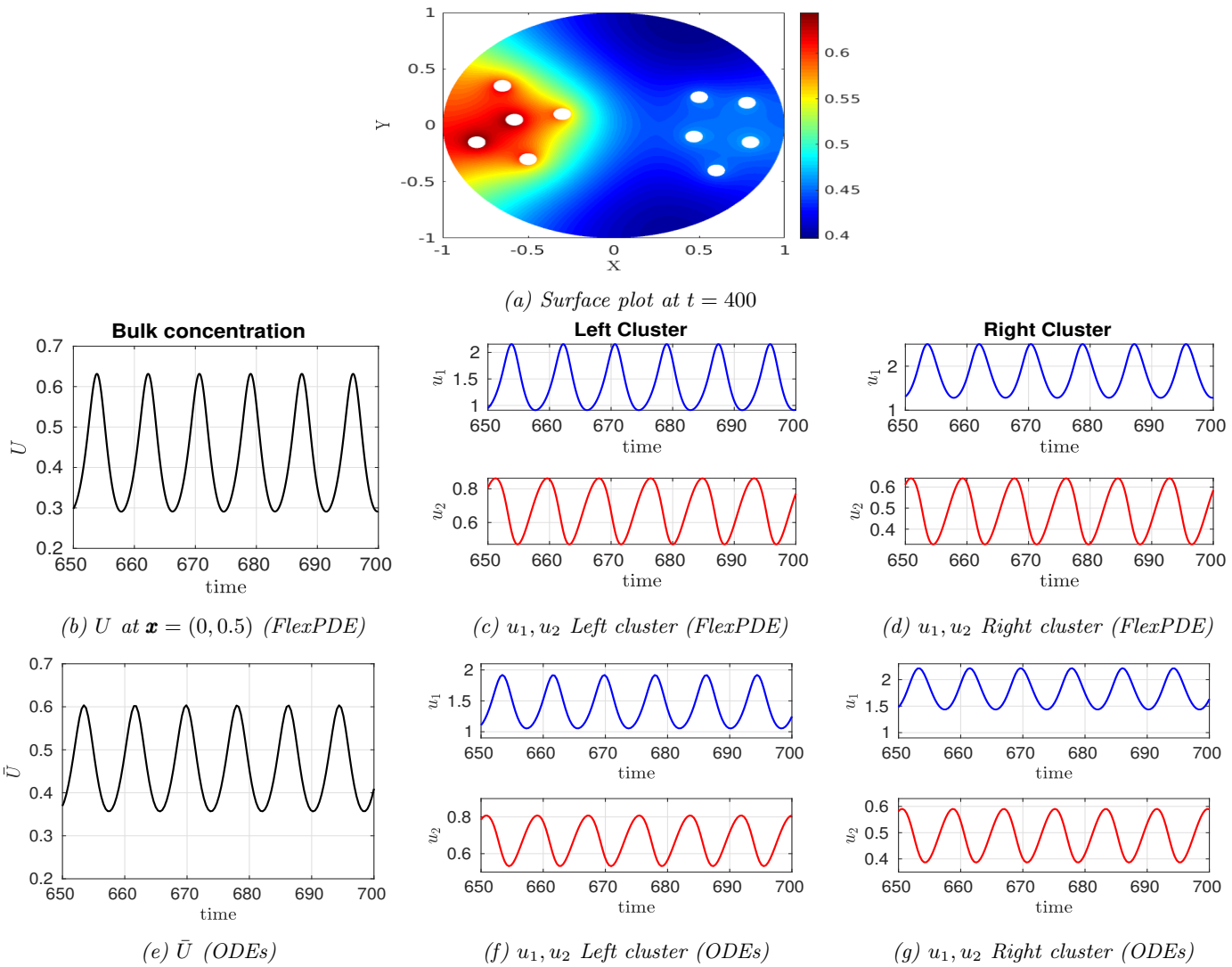

(a) Surface plot at $t = 400$

(b) U at $\boldsymbol{x} = (0, 0.5)$ (FlexPDE)

(c) u_1, u_2 Left cluster (FlexPDE)

(d) u_1, u_2 Right cluster (FlexPDE)

(e) $\bar{U}$ (ODEs)

(f) u_1, u_2 Left cluster (ODEs)

(g) u_1, u_2 Right cluster (ODEs)

Figure 21: Top and middle row: FlexPDE numerical results computed from the PDE-ODE model (1.2) for $m = 10$ cells, arranged in two clusters (see Fig. 17b) at the blue dot in Fig. 17a where $(D_0, \tau) = (0.4, 0.35)$. The cells in the left cluster have identical influx rates $d_1 = 0.4$ while the cells in the right cluster have $d_1 = 0.8$. The cell locations are in Table 4 of Appendix B. Within each cluster there is very similar intracellular dynamics. Lower row: corresponding results for $\bar{U}$, u_1, and u_2, as computed from the ODE system (3.16). The eigenvector and eigenvalue for the GCEP matrix for the linearization are in the middle third of Table 3.

From Table 4, cells 1 and 2 are from the left cluster, while 6 and 7 belong to the right cluster. The corresponding normalized eigenpair $\mathcal{K}\boldsymbol{c}$ of the GCEP matrix, as given in the bottom third of Table 3, predicts that the amplitudes of the intracellular dynamics will differ from cell to cell due to the different cell influx rates, but that there will only be a small phase shift in the intracellular oscillations. Since $|(\mathcal{K}\boldsymbol{c})_1| < |(\mathcal{K}\boldsymbol{c})_7|$ (see Table 3), the linearized theory predicts larger amplitude oscillations for u_1 in cell 7 than in cell 1, which is expected since cell 7 has a larger influx rate than does cell 1 (see Table 4). This is confirmed in the FlexPDE simulations in Fig. 22. In the bottom row of Fig. 22 we observe that the corresponding results from the ODE system (3.16) compare moderately well with the FlexPDE results regarding the amplitude and period of oscillations in the bulk medium and within the cells. We remark that if, instead, we used the simpler ODE system (3.19), corresponding to the well-mixed limit $D \to \infty$, the ODE results would be in very poor agreement with the full PDE simulations.

5.1.1 Isolated cells in a pattern can be quiescent: Diffusion-mediated behavior

In this subsection, we analyze in detail the role of the spatial configuration of the cells on the triggering of intracellular oscillations. Specifically, we consider the cell configuration shown in Fig. 23b, with cell centers given in Table 5 of Appendix B. This pattern consists of two spatially segregated rings of cells together with two cells that are spatially isolated from the rings. For this symmetric pattern we will consider five permeability parameter sets for the cell influx rate, as given in Table 5, which lead to solution behavior that can be interpreted both qualitatively and from our linear stability analysis.

In Fig. 23a we plot the HB boundaries in the τ versus D_0 parameter plane for permeability sets $II - V$ of Table 5, as obtained by solving for the roots of (5.22) numerically. There is no HB boundary in this parameter plane from (5.22) for

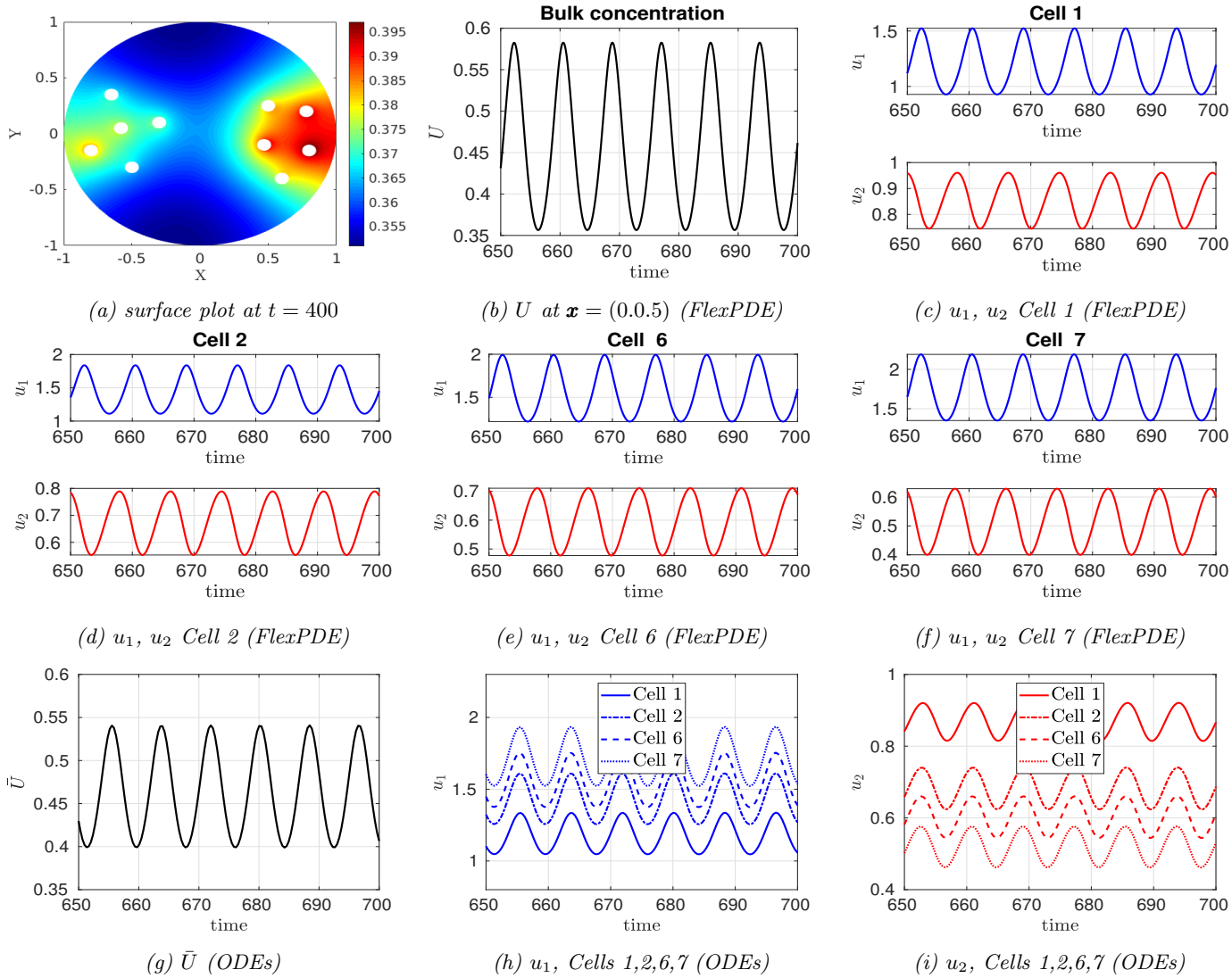

(a) surface plot at $t = 400$ *(b) U at $\boldsymbol{x} = (0.0.5)$ (FlexPDE)* *(c) u_1, u_2 Cell 1 (FlexPDE)*

(d) u_1, u_2 Cell 2 (FlexPDE) *(e) u_1, u_2 Cell 6 (FlexPDE)* *(f) u_1, u_2 Cell 7 (FlexPDE)*

(g) $\bar{U}$ (ODEs) *(h) u_1, Cells 1,2,6,7 (ODEs)* *(i) u_2, Cells 1,2,6,7 (ODEs)*

Figure 22: Top and middle row: FlexPDE numerical results computed from the PDE-ODE model (1.2) for $m = 10$ cells, arranged in two clusters (see Fig. 17b) at the green dot in Fig. 17a where $(D_0, \tau) = (1.5, 0.3)$. The influx rates are selected uniformly from the interval $0.4 \le d_1 \le 0.8$ (see Table 4 for set III). The cell locations are in Table 4 of Appendix B, with Cell 1 at $(0.47, -0.1)$, Cell 2 at $(0.78, 0.2)$, Cell 6 at $(-0.58, 0.05)$, and Cell 7 at $(-0.65, 0.35)$. Each cell has different intracellular dynamics owing to the different influx rates. Lower row: corresponding results for $\bar{U}$, u_1, and u_2, as computed from the ODE system (3.16). The eigenvector and eigenvalue for the GCEP matrix for the linearization are in the lower third of Table 3.

permeability set I, where $d_1 = 0.8$ for the ring cells and $d_1 = 0.3$ for the isolated cells. As verified from a numerical winding number computation, only within the lobes spanned by the HB boundaries is the steady-state unstable to an oscillatory instability. From the dotted and dashed-dotted curves in Fig. 23a corresponding to where all the cells have the common influx rates $d_1 = 0.3$ or $d_1 = 0.8$, respectively, we observe that the instability lobe is unbounded in D_0. Therefore, when the cells are all identical, intracellular oscillations occur within some finite band of the reaction-time parameter τ for all bulk diffusivities. For identical cells with $d_1 = 0.8$, the HB boundaries in Fig. 23a are very similar to that shown in Fig. 17 for the arbitrary cell pattern and the two-cluster pattern. For identical cells with the larger cell influx rate $d_1 = 0.8$ we observe from Fig. 23a that the lower threshold in τ where oscillatory instabilities first occur is smaller than when the common influx rate is $d_1 = 0.3$. To explain this qualitatively, we observe that τ decreases as the bulk decay rate k_B increases (see (1.3)). With a larger bulk decay rate, the bulk signal becomes less diffuse and has larger spatial gradients, which leads to a buildup of the bulk signal, near the cells. As a result, when there is a larger cell influx rate, the bulk signal can more readily enter the cell to trigger intracellular oscillations.

Since from Fig. 23 the steady-state is always linearly stable for permeability set I when $D = D_0/\nu$, this motivates studying the full GCEP matrix $\mathcal{M}(\lambda)$ in (2.20) that is valid for $D = \mathcal{O}(1)$. In the left and right panels of Fig. 24 we plot spectral information versus D, for fixed $\tau = 0.35$, obtained from the roots of $\det\mathcal{M}(\lambda) = 0$ for the two-ring and isolated cell pattern for permeability sets I (left panel) and II (right panel). In the left y-axes of Fig. 24 we plot the real parts of the three eigenvalues of the GCEP matrix that have the largest real parts. These three eigenvalue branches are associated with different spatial modes for the cells as indicated in the figure legends and discussed below. In the right y-axes of Fig. 24 we plot the sum

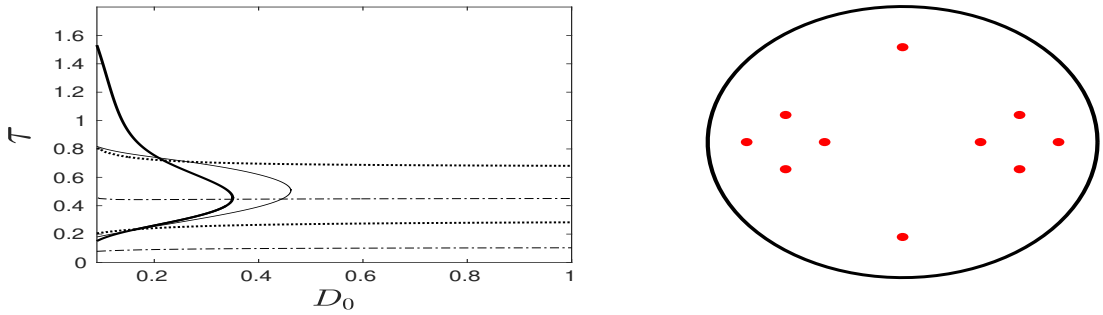

(a) HB boundaries *(b) Two rings of cells with two isolated cells*

Figure 23: HB boundaries (left panel) for $m = 10$ cells for a pattern with two rings of cells and two isolated cells (right panel). The cell locations and permeability parameter sets for the influx rates d_{1j} are given in Table 5 of Appendix B. Four out of five of the permeability sets in Table 5 give HB boundaries in the (D_0, τ) plane. The thin solid curve (set II) has $d_1 = 0.3$ for the ring cells and $d_1 = 0.8$ for the isolated cells. The heavy solid curve has $d_1 = 0.3$ for the isolated cells, $d_1 = 0.8$ for one group of ring cells, and $d_1 = 0.4$ for the cells on the other ring (set III). The dash-dotted curve has $d_1 = 0.8$ for all cells (set IV), while the dotted curve has $d_1 = 0.3$ for all cells (set V). There is no HB boundary for set I where $d_1 = 0.3$ and $d_1 = 0.8$ for the isolated and ring cells, respectively. The remaining parameters are given in (4.22).

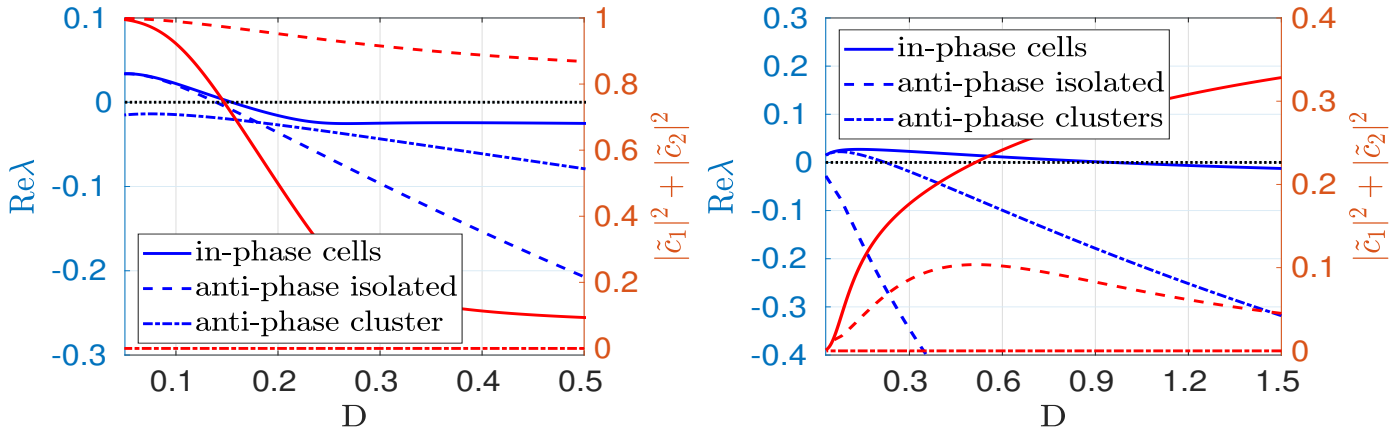

(a) set I: $d_1 = 0.8$ (rings), $d_1 = 0.3$ (isolated) *(b) set II: $d_1 = 0.8$ (isolated), $d_1 = 0.3$ (rings)*

Figure 24: Spectral information from the eigenvalues λ and normalized eigenvectors $\tilde{\boldsymbol{c}} = \mathcal{K}\boldsymbol{c}$, with $\sum_i |(\mathcal{K}\boldsymbol{c})_i|^2 = 1$, obtained from the GCEP matrix (2.20a) and (5.2a) for $\mathcal{K}$, as computed using root-finding on $\det \mathcal{M}(\lambda) = 0$. The cell configuration is the two-ring and two-isolated cell pattern of Fig. 23b for permeability set I (left panel) and permeability set II (right panel) for the fixed value $\tau = 0.35$. Left y-axis: Real parts (blue curves) of the three eigenvalues of the GCEP matrix with the largest real parts versus D. Right y-axis: The sum $|\tilde{c}_1|^2 + |\tilde{c}_2|^2$ (red curves) of the first two components of the normalized eigenvector $\mathcal{K}\boldsymbol{c}$, which measures the relative amplitude of oscillations in the two isolated cells in comparison to the cells on the ring. The linetype (solid, dashed, dot-dashed) of the blue and red curves correspond to the same eigenpair of the GCEP matrix.

$|\tilde{c}_1|^2 + |\tilde{c}_2|^2$ (red curves) of the first two components of the normalized eigenvector $\tilde{\boldsymbol{c}} \equiv \mathcal{K}\boldsymbol{c}$, which measures the relative amplitude of oscillations in the two isolated cells in comparison to the cells on the ring (see (2.24)). The linetype (solid, dashed, dot-dashed) of the blue and red curves in Fig. 24 correspond to the same eigenpair of the GCEP matrix.

For permeability set I, where the influx rate $d_1 = 0.3$ on the isolated cells is lower than that on the ring cells ($d_1 = 0.8$), we observe from the solid and dashed lines in Fig. 24a that there can be two unstable modes when D is small enough. On the range $D < 0.138$, there is an unstable mode given by the blue dashed curve where anti-phase oscillations occur for the two isolated cells (cells 1 and 2), which has a much higher amplitude than for the ring cells. On the two rings, cells 4 and 6 as well as cells 8 and 10 oscillate out of phase. The other ring cells (cells 3, 5, 7, and 9) are essentially quiescent for this mode. Due to the low influx rate into the isolated cells, the isolated cells communicate imperfectly with their images across the domain boundary when D is small, which leads to the anti-phase instability. Observe that as D increases above $D \approx 0.138$ this mode becomes stable and the amplitude in the isolated cells decreases (decreasing dashed red curve) since the bulk signal near the isolated cells is washed away. The other possible unstable mode, given by the blue solid curve in Fig. 24a, is one for which the two isolated cells are in-phase. The ring cells, which have smaller amplitude oscillations than do the isolated cells, are all roughly in phase and have only a slight phase difference with the isolated cells. This in-phase mode is unstable only for $D < 0.155$. We remark that this low stability threshold value of D is consistent with the observations in Fig. 23a that the steady-state is always linearly stable for $D = \mathcal{O}(\nu^{-1}) \gg 1$. Finally, the dashed-dotted blue curve in

Fig. 24a corresponds to a linearly stable mode where the isolated cells are quiescent, with each ring having cell oscillations that are (roughly) synchronized in amplitude and phase. However, for this mode there is a large phase shift between the oscillations in the two rings clusters. With the larger influx rate for the ring cells, there is effective communication between the two spatially segregated rings as D increases, which precludes any anti-phase instability between the two ring clusters.

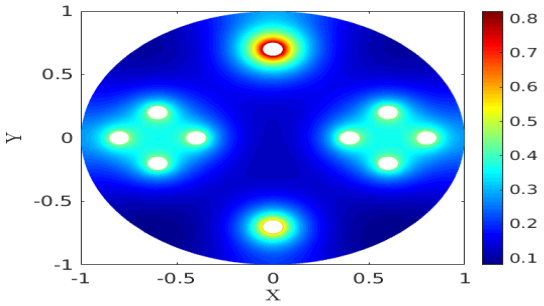

(a) Surface plot at $t = 400$

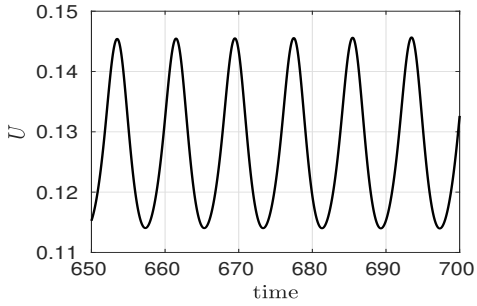

(b) U at $\boldsymbol{x} = (0, 0)$ (FlexPDE)

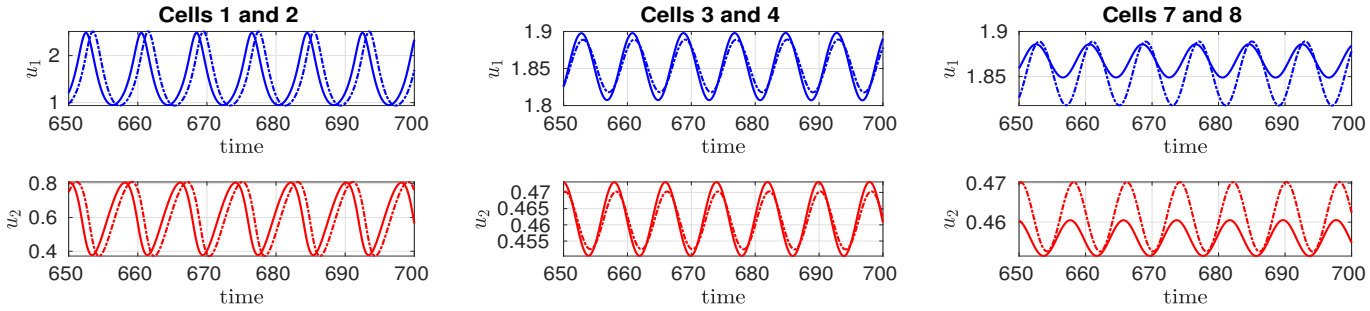

(c) u_1, u_2 isolated cells 1 and 2 (FlexPDE) *(d) u_1, u_2 cells 3 and 4 (left ring)* *(e) u_1, u_2 cells 7 and 8 (right ring)*

Figure 25: FlexPDE numerical results computed from the PDE-ODE model (1.2) for $m = 10$ cells, arranged in two rings with two isolated cells (see Fig. 23b) when $D = 0.05$ and $\tau = 0.35$ for the permeability set I and cell locations given in Table 5. Other parameters are given in (4.22). The linear stability predictions are given in Fig. 24a.

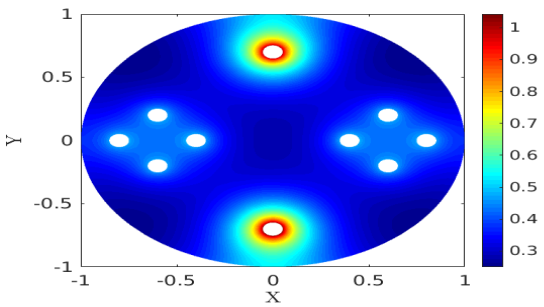

(a) Surface plot at $t = 400$

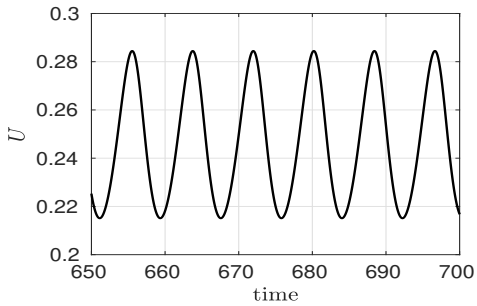

(b) U at $\boldsymbol{x} = (0, 0)$ (FlexPDE)

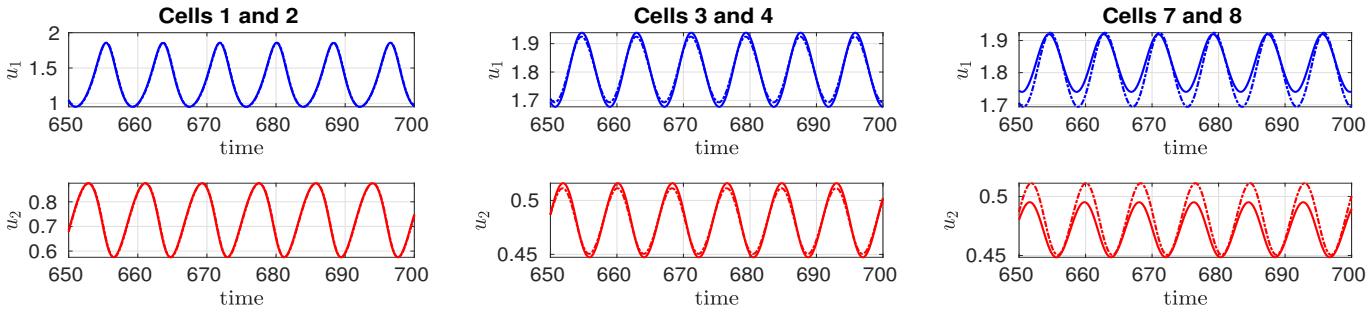

(c) u_1, u_2 isolated cells 1 and 2 (FlexPDE) *(d) u_1, u_2 cells 3 and 4 (left ring)* *(e) u_1, u_2 cells 7 and 8 (right ring)*

Figure 26: Same caption as in Fig. 25 except that now D is increased to $D = 0.13$. Observe that there is large in-phase signaling gradient near the isolated cells in the surface plot (a), and that the isolated cells have now synchronized their dynamics. The oscillations in the ring cells are more synchronized than when $D = 0.05$, but still have smaller amplitude for u_1 than do the isolated cells.

As a test of the predictions of the linear stability theory, as summarized by Fig. 24a, in Fig. 25 and Fig. 26 we show

FlexPDE results for (1.2) for permeability set I when $D = 0.05$ and $D = 0.13$, respectively. For $D = 0.05$ where both the in-phase and anti-phase modes (solid and dashed curves in Fig. 24a) are unstable with comparable growth rates, we observe from Figs. 25c–25e that, as predicted, the intracellular dynamics in cells 1 and 2 are not in-phase and that the amplitude of oscillations in the ring cells is much smaller than in the isolated cells. The strong anti-phase bulk signaling gradient at the isolated cells, as shown in Fig. 25a, is also consistent with the linear stability theory. In contrast, when $D = 0.13$, the in-phase mode is the dominant instability as seen from Fig. 24a. For this larger value of D, we observe from Fig. 26a and Fig. 26c that the bulk signaling gradient and the intracellular oscillations are now in-phase at the two isolated cells. Moreover, by comparing Figs. 25 and 26, we observe that the oscillations within the ring cells are more synchronized and have a larger amplitude, while the isolated cells have a smaller amplitude, when $D = 0.13$ as compared to when $D = 0.05$. These observations are all consistent with the linear stability predictions shown in Fig. 24a.

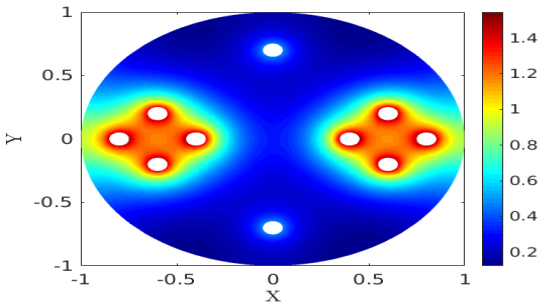

(a) Surface plot at $t = 400$

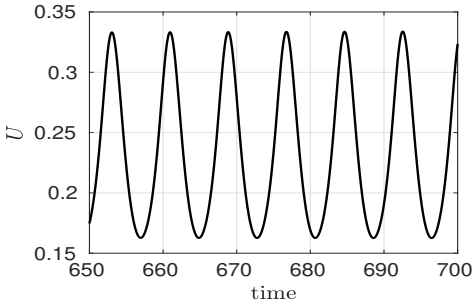

(b) U at $\boldsymbol{x} = (0, 0)$ (FlexPDE)

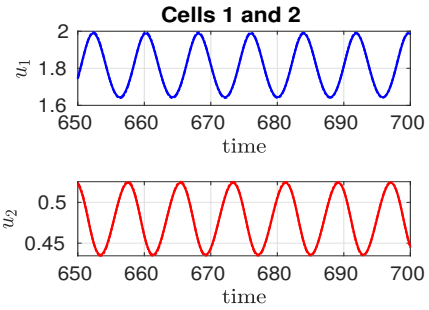

(c) u_1, u_2 isolated cells 1 and 2 (FlexPDE)

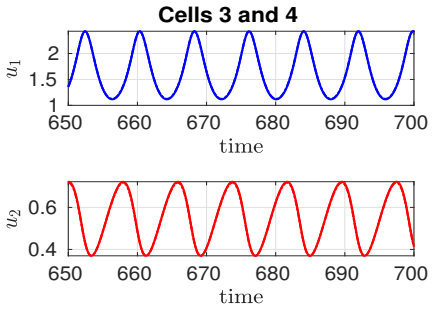

(d) u_1, u_2 cells 3 and 4 (left ring)

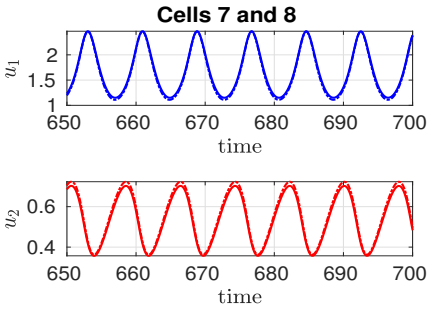

(e) u_1, u_2 cells 7 and 8 (right ring)

Figure 27: FlexPDE numerical results computed from the PDE-ODE model (1.2) for $m = 10$ cells, arranged in two rings with two isolated cells (see Fig. 23b) when $D = 0.05$ and $\tau = 0.35$ for the permeability set II and cell locations given in Table 5. Other parameters are given in (4.22). The linear stability predictions are given in Fig. 24b.

In Fig. 24b we show the corresponding spectral plot, as computed from the GCEP (2.20), for permeability set II where the isolated cells have a higher influx rate $d_1 = 0.8$ than do the ring cells $d_1 = 0.3$. In contrast to the case for permeability set I, we now observe that in addition to the usual in-phase mode that is unstable for $D < 0.95$, the only other possible unstable mode corresponds to an anti-phase instability between the two ring clusters. Since the influx rate into the ring cells has been decreased, this unstable mode is due to a relatively poorer communication between the two rings when the bulk diffusivity is small. This anti-phase cluster mode is unstable for $D < 0.22$. In contrast, the anti-phase mode for the isolated cells, which was unstable for permeability set I when D is small, is now always linearly stable for set II. Another key feature from Fig. 24b is that, for the in-phase mode, the intracellular oscillations in the isolated cells are much smaller when D is small than that in Fig. 24b. However, we observe from the increasing solid red curve in Fig. 24b that the amplitude of the oscillations in the isolated cells grows as D increases. The interpretation of this observation is that the secretion from the ring cells can more easily diffuse across the domain to the isolated cells, where it is readily absorbed, as D is increased. In Fig. 27 we show results from FlexPDE simulations of (1.2) for permeability set II when $D = 0.05$. The strong signalling gradient near the ring cells where the influx rate is small, the smaller amplitude oscillations in the isolated cells than in the rings, and the slight phase shift between the oscillations in the two ring clusters (cells 3 and 4 versus cells 7 and 8) are all consistent with the predictions in Fig. 24b of the linear stability theory.

Finally, to obtain some analytical insight into the possibility of an unstable mode consisting of anti-phase oscillations in the isolated cells together with quiescent ring cells, we implement the degenerate perturbation theory on the reduced GCEP matrix (5.4) from the $D = D_0/\nu$ regime. By using the simple criterion in (5.33), based on the quadratic equation (5.32), we calculate for permeability set I that this anti-phase mode for the isolated cells is unstable when $\tau = 0.35$ only when $D_0 < 0.0817$. This corresponds to $D < 0.245$ using $D = D_0/\nu$ with $\nu = -1/\log\varepsilon$ and $\varepsilon = 0.05$. Although this simple criterion (5.33) predicts the existence of an unstable anti-phase mode for the isolated cells, the threshold value is not so accurate (see Fig. 24a) owing to the fact that D is not asymptotically large. In contrast, for permeability set II, we calculate from the criterion (5.33) that the anti-phase mode for the isolated cells is always stable, as is consistent with Fig. 24b.

6 Discussion and Outlook

We have analyzed diffusion-mediated behavior for the coupled cell-bulk PDE-ODE system (1.2) that was used to model the switch-like onset of intracellular oscillations for a collection of heterogeneous cells, as mediated through a passive bulk diffusion field with finite bulk diffusivity D. For the case of Sel'kov reaction kinetics, we have studied how the onset of intracellular oscillations depends on the spatial configuration of cells, on the membrane permeability parameters, and on the triggering effect of a single "defective" cell with a different kinetic parameter. In contrast, in [26] QS behavior resulting from increase in cell density were studied using only the ODE system (3.19) with global coupling, which pertains to the well-mixed regime of infinite bulk diffusivity.

There are several open theoretical and computational challenges that should be explored for (1.2). One key numerical issue concerns developing efficient and well-conditioned numerical techniques to implement the full linear stability theory based on the root-finding condition $\det(\mathcal{M}(\lambda)) = 0$ for the GCEP given in (2.20) for a large number, i.e. $m \geq 100$, of randomly located cells with arbitrary permeabilities. The solution strategies for such nonlinear matrix eigenvalue problems are typically restricted to matrices wih special structure, such as Hermitian matrices, matrices with low-rank dependence on λ, or matrices that are quadratic or rational in the eigenvalue parameter λ (cf. [23] and [4]). In contrast, the GCEP matrix in (2.20) is not Hermitian when λ is complex-valued, and is not of low-rank owing to its dependence on the full eigenvalue-dependent Green's matrix $\mathcal{G}_\lambda$.

From a mathematical viewpoint, a second open direction would be to develop a weakly nonlinear theory for the Hopf bifurcations of steady-state solutions of (1.2). The numerical results shown in §4 and 5 have suggested that the intracellular oscillations are supercritical for the Sel'kov kinetics, and that their relative amplitude and phases within the cells are well-predicted by the eigenvector of the GCEP matrix $\mathcal{M}(\lambda)$ in (2.20). Also of interest would be to explore whether ODE phase-reduction techniques, such as surveyed in [41] and [36], can be extended to the PDE-ODE setting of (1.2).

From a modeling perspective, the PDE-ODE system (1.1) is well-suited for investigating triggered intracellular oscillations and collective dynamics associated with specific microbial systems for which detailed models of the signaling pathways are available, the autoinducer is known, and where membrane permeabilities can be estimated from biological data. Such calibrated biological models are readily incorporated into the theoretical framework (1.1). In particular, it would be worthwhile to analyze (1.1) with the detailed model of [57] and [25] for the glycolytic pathway in yeast cells and the model of [33] for bacterial communication of *Escherichia coli* cells. For non-oscillatory QS systems, it would be interesting to use the intracellular Lux-signaling pathways of [32] into our PDE-ODE model (1.1) to analyze sudden jumps between small and large amplitude steady-states for bistable QS systems as the cell density increases past a saddle-node bifurcation value. Moreover, (1.1) can be used to study the effect of spatial diffusion on the parallel QS signaling pathways associated with the marine bacterium *V. harveyi*, which were recently modeled in [5] through an ODE well-mixed limit. Our analysis in §3 has shown that the dimensionless PDE-ODE system (1.2) can be reduced to a limiting ODE system only when the bulk diffusivity satisfies $D = \mathcal{O}(-\log\varepsilon)$, where ε is the dimensionless ratio of the cell radius to the length scale of the domain. The classic ODE system for the well-mixed limit corresponds to the regime $D \gg \mathcal{O}(-\log\varepsilon)$.

From a different perspective, it would be interesting to examine quantitatively the relationship between the concept of *diffusion-sensing*, as pioneered in [43], and our analysis of *diffusion-mediated* communication. In our study, we have analyzed how spatial information such as, spatial gradients in the bulk signal, the permeability parameters and the bulk diffusivity, and the specific spatial configuration of cells, all play a key role in the triggering of collective dynamics. With regards to diffusion-sensing, in [43] it was postulated that each cell measures the rate of diffusion of the autoinducer in the local environment as a means to determine when it is beneficial to increase production of a signal.

Finally, it would be worthwhile to extend the 2-D model (1.1) to allow for two passive bulk diffusion fields, and to consider 3-D domains, where the cell-cell interaction is weaker than in 2-D owing to the rapid decay of the 3-D free-space Green's function. Although a similar analysis of a 3-D extension of the PDE-ODE model would be desirable, our analysis of the 2-D problem is relevant for modeling diffusion-mediated communication between cells in thin petri dishes. By including two bulk species, and with a re-formulation of the class of lattice-based models introduced in [42] into the framework of (1.1), it should be possible to show analytically that changes in the permeability parameters of a collection of cells can induce a Turing or transcritical bifurcation to a patterned steady-state for an activator-inhibitor system even when the two bulk diffusing species have very similar diffusivities. In a spatially homogeneous medium without cells, Turing bifurcations only occur for activator inhibitor systems when there is a sufficiently large diffusivity ratio, which is not typical for most biological systems. The PDE-ODE framework of (1.1), where the small signaling compartments are modeled explicitly, also provides an alternative approach for studying large-scale self-organized structures that have previously been modeled through PDE-ODE lattice dynamics in which the dynamically active "cells" are treated as point sources restricted to lattice sites and where a discrete Laplacian averaging over nearby lattice points replaces the Laplace operator (cf. [6], [44], [29]). Such lattice PDE-ODE systems have been used to model traveling waves of yeast activation due to substrate addition of glucose at a localized source (cf. [44]), and the emergence of spiral waves resulting from the coupling of Fitzhugh-Nagumo or Rossler cell kinetics to discrete lattice-based diffusion (cf. [29], [6]).

Acknowledgements

Michael Ward gratefully acknowledges the financial support from the NSERC Discovery grant program. We are grateful to Justin Tzou (Macquarie U.) for his initial help with the FlexPDE simulations.

Appendices

A The reduced-wave Green's function for the unit disk

In this appendix we provide explicit expressions for the matrix spectrum of (4.9) corresponding to the matrix block of the eigenvalue-dependent reduced-wave Green's matrix in (4.8) representing the interactions of $m-1 \geq 2$ cells on a ring of radius r_0, with $0 < r_0 < 1$, concentric within the unit disk. For notational convenience we define N by $N = m-1$. The N cells on the ring of radius r_0 are centered at $\boldsymbol{x}_k = r_0\,(\cos\psi_k, \sin\psi_k)^T$, where $\psi_k \equiv 2\pi(k-1)/N$ for $k = 1, \ldots, N$. In the unit disk, the reduced-wave Green's function $G_\lambda(\boldsymbol{x};\boldsymbol{\xi})$ and its regular part, satisfying (2.15), can be calculated using separation of variables as (see equations (6.10) and (6.11) of [20])

$$G_\lambda(\boldsymbol{x};\boldsymbol{\xi}) = \frac{1}{2\pi} K_0\left(\varphi_\lambda|\boldsymbol{x}-\boldsymbol{\xi}|\right) - \frac{1}{2\pi}\sum_{n=0}^{\infty} \beta_n \cos\left(n(\psi-\psi_0)\right) \frac{K_n'(\varphi_\lambda)}{I_n'(\varphi_\lambda)} I_n\left(\varphi_\lambda r\right) I_n\left(\varphi_\lambda \rho\right)\,, \tag{A.1a}$$

$$R_\lambda(\boldsymbol{\xi}) = \frac{1}{2\pi}\left[\log\left(2\sqrt{D}\right) - \gamma_e - \frac{1}{2}\log\left(1+\tau\lambda\right)\right] - \frac{1}{2\pi}\sum_{n=0}^{\infty} \beta_n \frac{K_n'(\varphi_\lambda)}{I_n'(\varphi_\lambda)}\left[I_n\left(\varphi_\lambda\rho\right)\right]^2\,, \tag{A.1b}$$

where $\varphi_\lambda \equiv \sqrt{(1+\tau\lambda)/D}$ is the principal branch of φ_λ, $\gamma_e = 0.5772$ is Euler's constant, and $I_n(z)$ and $K_n(z)$ are the modified Bessel functions of the first and second kind of order n, respectively. In (A.1), $\beta_0 \equiv 1$, $\beta_n \equiv 2$ for $n \geq 1$, while $\boldsymbol{x} \equiv r(\cos\psi, \sin\psi)^T$, and $\boldsymbol{\xi} \equiv \rho(\cos\psi_0, \sin\psi_0)^T$.

For a ring pattern, the $N \times N$ symmetric Green's matrix $\mathcal{G}_{\lambda N}$ is also cyclic and can be generated by a cyclic permutation of its first row $\boldsymbol{a}_\lambda \equiv (a_{\lambda,1}, \ldots, a_{\lambda,N})^T$, which is defined term-wise by

$$a_{\lambda,1} \equiv R_\lambda(\boldsymbol{x}_1)\,; \qquad a_{\lambda,k} = G_\lambda(\boldsymbol{x}_k;\boldsymbol{x}_1)\,, \qquad k = 2, \ldots, N\,. \tag{A.2}$$

The matrix spectrum $\mathcal{G}_{\lambda N}\boldsymbol{v}_j = \omega_{\lambda j}\boldsymbol{v}_j$ in (4.9) with $N = m-1$ is calculated as in §6 of [20]. The in-phase eigenpair is

$$\omega_{\lambda N} = \sum_{k=1}^{N} a_{\lambda,k}\,, \qquad \boldsymbol{v}_N = (1, \ldots, 1)^T\,, \tag{A.3a}$$

while the other eigenvalues, corresponding to the anti-phase modes for which $\boldsymbol{v}_j^T\boldsymbol{v}_N = 0$ for $j = 1, \ldots, N-1$, are

$$\omega_{\lambda j} = \sum_{k=0}^{N-1} \cos\left(\frac{2\pi jk}{N}\right) a_{\lambda,k+1}\,, \qquad j = 1, \ldots, N-1\,. \tag{A.3b}$$

Since $\omega_{\lambda j} = \omega_{\lambda,N-j}$ for $j = 1, \ldots, \lceil N/2\rceil - 1$, there are $\lceil N/2\rceil - 1$ pairs of degenerate eigenvalues for $\mathcal{G}_{\lambda N}$. Here the ceiling function $\lceil x\rceil$ is defined as the smallest integer not less than x. When N is even, there is an eigenvalue of multiplicity one given by $\omega_{\lambda,\frac{N}{2}} = \sum_{k=0}^{N-1}(-1)^k a_{\lambda,k+1}$. The other eigenvectors for $j = 1, \ldots, \lceil N/2 - 1\rceil$ are

$$\boldsymbol{v}_j = \left(1, \cos\left(\frac{2\pi j}{N}\right), \ldots, \cos\left(\frac{2\pi j(N-1)}{N}\right)\right)^T\,, \qquad \boldsymbol{v}_{N-j} = \left(0, \sin\left(\frac{2\pi j}{N}\right), \ldots, \sin\left(\frac{2\pi j(N-1)}{N}\right)\right)^T\,. \tag{A.3c}$$

Finally, when N is even, there is an additional eigenvector $\boldsymbol{v}_{\frac{N}{2}} = (1, -1, \ldots, -1)^T$. By using the explicit formulae for G_λ and its regular part from (A.1), the eigenvalues $\omega_{\lambda j}$ of the Green's matrix $\mathcal{G}_{\lambda N}$ are then easily computed from (A.3).

Remark 1. *The symmetric and cyclic matrix $\mathcal{G}_{\lambda N}$ has $N/2$ distinct anti-phase modes if N is even and $(N-1)/2$ distinct anti-phase modes if N is odd.*

Finally, in order to calculate the quantities in (4.2) and (4.3), which are needed in (4.4) for determining the steady-state solution, we need only set $\lambda = 0$ in (A.1) and (A.3a).

B Cell locations and permeability parameters

The cell locations and permeability parameter sets for the influx rate d_{1j}, for $j = 1, \ldots, m$, are given in the next two tables for the cell patterns studied in §5.

Cell i	Two clusters of cells				Arbitrary cell locations			
	x_i	y_i	d_{1i}(II)	d_{1i}(III)	x_i	y_i	d_{1i}(II)	d_{1i}(III)
1	0.4700	−0.1000	0.8	0.4000	0.5205	−0.4687	0.4	0.4000
2	0.7800	0.2000	0.8	0.5168	−0.1856	−0.1927	0.8	0.5168
3	0.8000	−0.1500	0.8	0.4378	0.3170	−0.0236	0.8	0.4378
4	0.5000	0.2500	0.8	0.6120	−0.3571	0.6112	0.4	0.6120
5	0.6000	−0.4000	0.8	0.7421	0.2019	0.5935	0.4	0.7421
6	−0.5800	0.0500	0.4	0.6069	−0.7526	0.1667	0.8	0.6069
7	−0.6500	0.3500	0.4	0.7062	−0.5500	−0.4543	0.4	0.7062
8	−0.8000	−0.1500	0.4	0.4365	0.0203	0.3201	0.4	0.4365
9	−0.3000	0.1000	0.4	0.5629	0.6947	0.1265	0.8	0.5629
10	−0.5000	−0.3000	0.4	0.8000	−0.0172	−0.7422	0.8	0.8000

Table 4: Locations of the cell centers and influx permeability rates for parameter sets II and III corresponding to the two cluster arrangement of cells in Fig. 17b (columns 2–5) and the arbitrary arrangement of cells in Fig. 17d (columns 6–9). The permeability parameter set I (not shown) is for identical cells where $d_{1j} = 0.8$ for $j = 1, \ldots, m$.

Cell i	Two rings with two isolated cells						
	x_i	y_i	d_{1i}(I)	d_{1i}(II)	d_{1i}(III)	d_{1i}(IV)	d_{1i}(V)
1	0.0000	−0.7000	0.3	0.8	0.3	0.8	0.3
2	0.0000	0.7000	0.3	0.8	0.3	0.8	0.3
3	−0.4000	0.0000	0.8	0.3	0.8	0.8	0.3
4	−0.6000	0.2000	0.8	0.3	0.8	0.8	0.3
5	−0.8000	0.0000	0.8	0.3	0.8	0.8	0.3
6	−0.6000	−0.2000	0.8	0.3	0.8	0.8	0.3
7	0.8000	0.0000	0.8	0.3	0.4	0.8	0.3
8	0.6000	0.2000	0.8	0.3	0.4	0.8	0.3
9	0.4000	0.0000	0.8	0.3	0.4	0.8	0.3
10	0.6000	−0.2000	0.8	0.3	0.4	0.8	0.3

Table 5: Locations of the cell centers and influx permeability rates for parameter sets I–V corresponding to the pattern of two rings of cells together with two isolated cells, as shown in Fig. 23.

References

[1] Continuation Test: a MATLAB library which defines test functions for continuation codes. http://people.math.sc.edu/Burkardt/m_src/test_con/test_con.html. Accessed: 2020-02-26.

[2] D. Alciatore and R. Miranda. A winding number and point-in-polygon algorithm. *Glaxo Virtual Anatomy Project Research Report, Department of Mechanical Engineering, Colorado State University*, 1995.

[3] T. Betcke, N. G. Highan, V. Mehrmann, G. M. N. Porzio, C. Schröder, and Tisseur F. NLEVP: A collection of nonlinear eigenvalue problems. users' guide. *MIMS EPring 2011.117, Manchester Institue for Mathematical Sciences, The University of Manchester, UK*, page 10 pages, updated 2019.

[4] T. Betcke, N. G. Highan, V. Mehrmann, C. Schröder, and Tisseur F. NLEVP: A collection of nonlinear eigenvalue problems. *ACM Trans. Math. Software*, 39(2):7.1–7.28, 2013.

[5] P. Bressloff. Ultrasensitivity and noise amplification in a model of v. harveyi quorum sensing. *Phys. Rev. E*, 93:062418, 2016.

[6] X. Z. Cao, H. Yuan, and B. W. Li. Selection of spatiotemporal patterns in arrays of spatially distributed oscillators indirectly coupled via a diffusive environment. *Chaos*, 29:043104, 2019.

[7] M. A. J. Chaplain, M. Ptashnyk, and M. Sturrock. Hopf bifurcation in a gene regulatory network model: Molecular movement causes oscillations. *Math. Mod. Meth. Appl. Sci.*, 25(6):1179–1215, 2015.

[8] S. Danø, M. F. Madsen, and P. G. Sørensen. Quantitative characterization of cell synchronization in yeast. *Proceedings of the National Academy of Sciences*, 104(31):12732–12736, 2007.

[9] S. Danø, P. G. Sørensen, and F. Hynne. Sustained oscillations in living cells. *Nature*, 402(6759):320–322, 1999.

[10] S. De Monte, F. d'Ovidio, S. Danø, and P. G. Sørensen. Dynamical quorum sensing: Population density encoded in cellular dynamics. *Proceedings of the National Academy of Sciences*, 104(47):18377–18381, 2007.

[11] G. E. Dilanji, J. B. Langebrake, P. De Leenheer, and S. J. Hagen. Quorum activation at a distance: Spatiotemporal patterns of gene regulation from diffusion of an autoinducer signal. *J. Am. Chem. Soc.*, 6:34695, 2016.

[12] J. D. Dockery and J. P. Keener. A mathematical model for quorum sensing in *pseudomonas aeruginosa*. *Bull Math Biol.*, 63(1):95–116, 2001.

[13] G. M. Dunny and B. Leonard. Cell-cell communication in gram-positive bacteria. *Annual review of microbiology*, 51(1):527–564, 1997.

[14] PDE FlexPDE. Solutions inc. *URL http://www. pdesolutions. com*, 2015.

[15] M. Gao, H. Zheng, Y. Ren, R. Lou, F. Wu, W. Yu, X. Liu, and X. Ma. A crucial role for spatial distribution in bacterial quorum sensing. *Scientific Reports*, 6(34695), 2016.

[16] A. Goldbeter. *Biochemical oscillations and cellular rhythms: the molecular bases of periodic and chaotic behaviour*. Cambridge university press, 1997.

[17] A. Gomez-Marin, J. Garcia-Ojalvo, and J. M. Sancho. Self-sustained spatiotemporal oscillations induced by membrane-bulk coupling. *Phys. Rev. Lett.*, 98:168303, Apr 2007.

[18] J. Gou, W.-Y. Chiang, P.-Y. Lai, M. J. Ward, and Y.-X. Li. A theory of synchrony by coupling through a diffusive chemical signal. *Physica D*, 339:1–17, 2017.

[19] J. Gou, Y. X. Li, W. Nagata, and M. J. Ward. Synchronized oscillatory dynamics for a 1-D model of membrane kinetics coupled by linear bulk diffusion. *SIAM J. Appl. Dyn. Sys.*, 14(4):2096–2137, 2015.

[20] J. Gou and M. J. Ward. An asymptotic analysis of a 2-d model of dynamically active compartments coupled by bulk diffusion. *Journal of Nonlinear Science*, 26(4):979–1029, 2016.

[21] J. Gou and M. J. Ward. Oscillatory dynamics for a coupled membrane-bulk diffusion model with Fitzhugh-Nagumo kinetics. *SIAM J. Appl. Math.*, 76(2):776–804, 2016.

[22] T. Gregor, K. Fujimoto, N. Masaki, and S. Sawai. The onset of collective behavior in social amoebae. *Science*, 328(5981):1021–1025, 2010.

[23] S. Güttel and F. Tisseur. The nonlinear eigenvalue problem. *Acta Numerica*, 26(1):1–94, 2017.

[24] B. A. Hense, C. Kuttler, J. Müller, M. Rothballer, A. Hartmann, and J. U. Kreft. Does efficiency sensing unify diffusion and quorum sensing? *Nature Reviews. Microbiology*, 5:230–239, 2007.

[25] M. A. Henson, Müller D., and M. Reuss. Cell population modelling of yeast glycolytic oscillations. *Biochem J.*, 368:433–446, 2002.

[26] S. Iyaniwura and M. J. Ward. Localized signaling compartments in 2-d coupled by a bulk diffusion field: Quorum sensing and synchronous oscillations in the well-mixed limit. *to appear, Europ. J. Appl. Math.*, 2020.

[27] K. Kamino, K. Fujimoto, and Sawai S. Collective oscillations in developing cells: Insights from simple systems. *Develop. Growth Differ.*, 53:503–517, 2011.

[28] T. Kolokolnikov, M. S Titcombe, and M. J. Ward. Optimizing the fundamental Neumann eigenvalue for the Laplacian in a domain with small traps. *Europ. J. Appl. Math.*, 16(2):161–200, 2005.

[29] B. W. Li, X. Z. Cao, and C. Fu. Quorum sensing in populations of spatially extended chaotic oscillators coupled indirectly via a heterogeneous environment. *Journal of NonLinear Science*, 27(6):1667–1686, 2017.

[30] B. W. Li, C. Fu, H. Zhang, and X. Wang. Synchronization and quorum sensing in an ensemble of indirectly coupled chaotic oscillators. *Physical Review E*, 86(4):046207, 2012.

[31] C. K. Macnamara and M. A. J. Chaplain. Spatio-temporal models of synthetic genetic oscillations. *Math. Biosc. Eng.*, 14:249–262, 2017.

[32] P. Melke, P. Sahlin, A. Levchenko, and H. Jonsson. A cell-based model for quorum sensing in heterogeneous bacterial colonies. *PLoS Computational Biology*, 6(6):e1000819, 2010.

[33] P. Mina, M. di Benardo, N. J. Savery, and K. Tsaneva-Atanasova. Modeling emergence of oscillations in communicating bacteria: a structured approach from one to many cells. *J. Royal Society Interface*, 10:20120612, 2012.

[34] J. Müller, C. Kuttler, B. A. Hense, M. Rothballer, and A. Hartmann. Cell–cell communication by quorum sensing and dimension-reduction. *Journal of mathematical biology*, 53(4):672–702, 2006.

[35] J. Müller and H. Uecker. Approximating the dynamics of communicating cells in a diffusive medium by odes—homogenization with localization. *Journal of mathematical biology*, 67(5):1023–1065, 2013.

[36] H. Nakao. Phase reduction approach to synchronisation of nonlinear oscillators. *Contemporary Physics*, 57(2):188–214, 2015.

[37] V. Nanjundiah. Cyclic AMP oscillations in Dictyostelium Discoideum: Models and observations. *Biophysical chemistry*, 72(1-2):1–8, 1998.

[38] F. Naqib, T. Quail, L. Musa, H. Vulpe, J. Nadeau, J. Lei, and L. Glass. Tunable oscillations and chaotic dynamics in systems with localized synthesis. *Phys. Rev. E*, 85:046210, Apr 2012.

[39] J. Noorbakhsh, D. J. Schwab, A. E. Sgro, T. Gregor, and P. Mehta. Modeling oscillations and spiral waves in *dictyostelium* populations. *Phys Rev. E.*, 91(6):062711, 2015.

[40] F. Paquin-Lefebvre, W. Nagata, and M. J Ward. Pattern formation and oscillatory dynamics in a two-dimensional coupled bulk-surface reaction-diffusion system. *SIAM J. Appl. Math.*, 80(3):1520–1545, 2020.

[41] B. Pietras and A. Daffertshofer. Network dynamics of coupled oscillators and phase reduction techniques. *Physics Reports*, 819:1–105, 2019.

[42] E. M. Rauch and M. Millonas. The role of trans-membrane signal transduction in turing-type cellular pattern formation. *J. Theor. Biol.*, 226:401–407, 2004.

[43] R. Redfied. Is quorum-sensing a side effect of diffusion sensing? *Trends Microbiology*, 10:365–370, 2002.

[44] J. Schütze and J. Wolf. Spatio-temporal dynamics of glycolysis in cell layers: A mathematical model. *Biosystems*, 99(2):104–108, 2010.

[45] E. E. Sel'kov. Self-oscillations in glycolysis 1. a simple kinetic model. *European Journal of Biochemistry*, 4(1):79–86, 1968.

[46] M. E. Taga and B. L. Bassler. Chemical communication among bacteria. *Proceedings of the National Academy of Sciences*, 100(suppl 2):14549–14554, 2003.

[47] A. F. Taylor, M. Tinsley, and K. Showalter. Insights into collective cell behavior from populations of coupled chemical oscillators. *Phys. Chemistry Chem Phys.*, 17(31):20047–20055, 2015.

[48] A. F. Taylor, M. Tinsley, F. Wang, Z. Huang, and K. Showalter. Dynamical quorum sensing and synchronization in large populations of chemical oscillators. *Science*, 323(5914):614–6017, 2009.

[49] M. R. Tinsley, A. F. Taylor, Z. Huang, and K. Showalter. Emergence of collective behavior in groups of excitable catalyst-loaded particles: Spatiotemporal dynamical quorum sensing. *Phys. Rev. Lett.*, 102:158301, 2009.

[50] M. R. Tinsley, A. F. Taylor, Z. Huang, F. Wang, and K. Showalter. Dynamical quorum sensing and synchronization in collections of excitable and oscillatory catalytic particles. *Physica D*, 239(11):785–790, 2010.

[51] A. Trovato, F. Seno, M. Zanardo, S. Alberghini, A. Tondello, and A. Squartini. Quorum vs. diffusion sensing: A quantitative analysis of the relevance of absorbing or reflecting boundaries. *FEMS Microbiology Letters*, 352:198–203, 2014.

[52] H. Uecker, J. Müller, and B. A. Hense. Individual-based model for quorum sensing with background flow. *Bulletin of mathematical biology*, 76(7):1727–1746, 2014.

[53] J. P. Ward, J. R. King, A. J. Koerber, P. Williams, J. M. Croft, and R. E. Sockett. Mathematical modelling of quorum sensing in bacteria. *Mathematical Medicine and Biology*, 18(3):263–292, 2001.

[54] M. J Ward. Spots, traps, and patches: Asymptotic analysis of localized solutions to some linear and nonlinear diffusive systems. *Nonlinearity*, 31(8):R189, 2018.

[55] M. J. Ward, W. D. Henshaw, and J. B. Keller. Summing logarithmic expansions for singularly perturbed eigenvalue problems. *SIAM J. Appl. Math.*, 53(3):799–828, 1993.

[56] M. Whiteley, S. P. Diggle, and E. P. Greenberg. Bacterial quorum sensing: the progress and promise of an emerging reserch areas. *Nature*, 551:7680, November 15 2017.

[57] J. Wolf and R. Heinrich. Effect of cellular interaction on glycolytic oscillations in yeast: a theoretical investigation. *Biochem J.*, 345:321–334, 2000.

[58] B. Xu and P. Bressloff. A PDE-DDE model for cell polarization in fission yeast. *SIAM J. Appl. Math.*, 76(3):1844–1870, 2016.